Multi-level Control in Large-anharmonicity High-coherence Capacitively Shunted Flux Quantum Circuits

by

Muhammet Ali Yurtalan

A thesis
presented to the University of Waterloo
in fulfillment of the
thesis requirements for the degree of
Doctor of Philosophy
in
Electrical and Computer Engineering (Quantum Information)

Waterloo, Ontario, Canada, 2019

Examining Committee Membership

The following served on the Examining Committee for this thesis. The decision of the Examining Committee is by majority vote.

External Examiner	Max Hofheinz Associate Professor
Supervisor	Adrian Lupascu Associate Professor
Supervisor	Zbigniew Wasilewski Professor
Internal Member	Bo Cui Associate Professor
Internal Member	Guoxing Miao Associate Professor
Internal-External Member	Jonathan Baugh Associate Professor

This thesis consists of material all of which I authored or co-authored: see Statement of Contributions included in the thesis. This is a true copy of the thesis, including any required final revisions, as accepted by my examiners.

I understand that my thesis may be made electronically available to the public.

Statement of Contributions

Most of the material in Chapter 5 consists of co-authored content. Muhammet Ali Yurtalan and Adrian Lupascu worked on the design and modeling of the device. Muhammet Ali Yurtalan conducted the experiments and performed device simulations. Muhammet Ali Yurtalan and Jiahao Shi fabricated the sample and performed data analysis. Muhammet Ali Yurtalan and Graydon Flatt performed numerical simulations of randomized benchmarking protocol. Adrian Lupascu supervised the experimental work.

Most of the material in Chapter 6 consists of co-authored content. Muhammet Ali Yurtalan conducted the experiments and performed numerical simulations. Muhammet Ali Yurtalan and Jiahao Shi fabricated the sample. Sahel Ashhab and Adrian Lupascu worked on theoretical implementation and analysis of the experiments. Adrian Lupascu supervised the experimental work.

Abstract

Superconducting devices as quantum bits (qubits) are one of the most promising candidates for implementing a practical quantum computer. Over the last decade, quantum coherence times of superconducting qubits have been continuously improved. Operating qubits in noise insensitive points, eliminating the participation of the lossy materials, and better isolation from environment increased the decoherence times from nanoseconds to tens of microseconds. One recent approach on the qubit design is to shunt the Josephson junctions with large capacitors to reduce the sensitivity to noise and to redistribute the stored electromagnetic energy in a well-engineered area. This approach was first applied on charge qubits and later adopted to other types of superconducting qubits.

In this thesis, we present the design and the characterization of a three-Josephson junction superconducting circuit with three large shunt capacitors. We present experiments on decoherence in the circuit used as a qubit. The qubit relaxation time T_1 is reaching as high as $47\mu s$ and the spin-echo dephasing time $T_{2E} = 9.4\mu s$. In addition, we present spectroscopy experiments and decoherence characterization in the qutrit subspace formed by the lowest three energy levels. The spectroscopy data is in excellent agreement with the complete circuit model based on the system capacitance matrix. At the flux symmetry point, the circuit has a large anharmonicity, defined as the difference between the 1-2 and 0-1 transition frequencies, approaching $2\pi \times 3.7$ GHz, which is enabling fast single qubit operations. We performed randomized benchmarking with the qubit gates with a duration of 1.62 ns and an average gate fidelity of 99.9%.

Moreover, we present experiments with multi-level control in qutrit subspace, formed by the lowest three energy levels. We demonstrate a single step experimental implementation of a generalized Walsh-Hadamard gate. We use a decomposition of the quantum gate into two unitary operations, one implemented by an off-diagonal Hamiltonian and the other implemented by a diagonal Hamiltonian. The off-diagonal Hamiltonian is obtained by the simultaneous driving of the transitions between levels 0-1, 1-2, and 0-2, with the latter being a two-photon process. The diagonal Hamiltonian is effectively implemented

by appropriately shifting the phases of adjacent pulses. The gate is characterized using tomography process and the average fidelity exceeds 90%, in good agreement with numerical simulations that take into account the multi-level structure of the system.

Acknowledgments

I would like to thank my supervisor Prof. Adrian Lupascu for encouraging me to pursue a research in quantum computing with superconductors and for his exemplary stance in methodology, discipline and dedication. I am grateful for the skills and knowledge I obtained during my studies, and thankful for the opportunities I was provided.

I would also like to thank Prof. Zbigniew Wasilewski for his co-supervision and Prof. Sahel Ashhab for the most appreciated discussions and help on the experiments. I am thankful to the members of my thesis advisory committee, Prof. Jonathan Baugh, Prof. Bo Cui, Prof. Guoxing Miao and Prof. Max Hofheinz.

I would like to extend my thanks to all present and past SQD group members. I am grateful to Mustafa Bal, Florian Ong, Pol Forn-Diaz, Jean-Luc Orgiazzi, Marty Otto and Chunqing Deng for the useful discussions, help and support. I would also like to thank Jiahao Shi for his dedication, eagerness and his most appreciated help on the experiments.

I am thankful to Quantum NanoFab team, IQC IT team and Roberto Romero for their amazing assistance and support.

Lastly, I would like to thank my family and my friends for their never-ending support and encouragements throughout my studies.

Table of Contents

List of Tables

List of Figures

Chapter 1

Introduction

Quantum computers, as an emerging technology, promise breakthroughs in many aspects of our daily lives such as computation, communication, and security. Compared to the classical computers they harness the quantum nature of physical systems and offer speed up in certain algorithms, secure communication, better encryption protocols , and simulations of natural quantum system [1].

The basic unit of a quantum computer is a quantum bit (qubit) which is essentially a two level system. Similar to classical bits, qubits can be in state 0 or 1. On the contrary to their classical counterpart, qubits can be in a superposition of these two states. When a measurement is performed, the qubit superposed state collapses to either state 0 or 1. However, certain algorithms and quantum gates can act on the superposed state acting on all superposed states simultaneously, offering a speed up on computation tasks. In 1994 Peter Shor demonstrated that the factorization of large numbers into prime factors could be exponentially faster then the best known classical algorithms [2].

There are several types of physical implementations of qubits. The most evident quantum systems are the microscopic natural systems such as single atoms [3, 4], ions [5, 6, 7] or spins [8, 9, 10]. Such qubits are well established and studied in literature [11]. In addition to the microscopic systems, a quantum system can be engineered in macroscopic scales

using superconducting circuits [12, 13, 14, 15, 16]. The main component of the superconducting qubits is the Josephson junction. Superconducting qubits are often called as artificial atom since they mimic microscopic quantum objects in macroscopic scales. Due to the relatively large sizes, on-chip superconducting qubits fully utilizes the advancements in micro- and nano-fabrication methods leading to more reproducible devices and scalable architectures.

One of the major challenges in superconducting devices is to increase the quantum information storage life times. One disadvantage with on-chip superconductors is that they can couple to their environment strongly due to their macroscopic size. Therefore, the noise channels can induce significant decoherence on the stored information. Reducing the sensitivity of the qubit to noise channels is a key aspect to implement a practical fault tolerant quantum computer.

There are two characteristic energy scales defining superconducting qubit states, namely the charging energy E_{C} and the Josephson energy E_{J} of the junctions. In the charge regime ($E_{\mathrm{J}} < E_{\mathrm{C}}$), the quantum states are defined by the well defined charges whereas in the flux regime ($E_{\mathrm{J}} > E_{\mathrm{C}}$) the states are defined by the well defined phase or the flux. The charge qubit is operated in charge regime, however the qubit is sensitive to charge fluctuations. The coherence time of the charge qubit can be improved by reducing the sensitivity to charge noise. One of the recent achievements in design of a charge qubit is the capacitive shunting of qubit Josephson junctions. This approach reduces the sensitivity to charge fluctuations. In addition, capacitive shunting allows for storing the electromagnetic energy in an engineered area, effectively removing the participation of lossy environment around qubit and suppressing the dielectric loss. This modification of the charge qubit increased the coherence times significantly [17].

The superconducting flux qubit is formed by interrupting a superconducting loop with typically one [18] or three [19] Josephson junctions. The two quantum basis states are persistent supercurrents in the loop circulating in clockwise and anticlockwise directions. The flux qubit is insensitive to charge fluctuations as it is operated in the large $E_{\mathrm{J}}/E_{\mathrm{C}}$

regime. On the other hand, the fluctuations in flux can induce significant decoherence especially away from the flux symmetry point. Over the years flux qubits demonstrated relatively high coherence with flexibility in terms of quantum control and integration in other circuits. However, until recently the coherence were improved marginally. Capacitive shunting of the flux qubit is proposed to reduce the charge noise [20] and recently a systematic study of flux qubit with single shunt pads demonstrated high coherence with moderate anharmonicity of 0.8 GHz in optimized samples [21].

1.1 Objective of the thesis

The objective of this thesis is to present a design for a three junction flux qubit by introducing shunt capacitors to all three qubit junctions to uniformly redistribute the electric fields in an engineered area. The aim is to reduce the participation of the lossy materials in the vicinity of the qubit affecting qubit coherence. In addition, this work proposes a model for the design to investigate the design space and to determine the circuit characteristics with fabrication parameters. This works also proposes to investigate the device characteristic in multi-level structure and explore single-qubit and qutrit gates.

1.2 Outline of this thesis

In this thesis, we present the design and a model for the capacitively shunted flux device coupled to a superconducting coplanar waveguide (CPW) resonator. The device is formed of three Josephson junctions shunted by three large capacitor pads, creating a loop circuit. We perform spectroscopy experiments and demonstrate multi-level structure of the device. In addition, we characterize coherence in qubit and qutrit space and investigate the possible sources of decoherence. We show fast and high-fidelity single qubit gates and benchmark the gate fidelities with a randomized benchmarking protocol. We also demonstrate multi-level control of the device in qutrit subspace and utilize state tomography process for

fidelity analyses of qutrit gates.

In Chapter 2, first, the basic building blocks of superconducting devices including coplanar waveguide resonators, Josephson junctions, and qubits are introduced. Next, qubit control and qubit resonator interactions in circuit quantum electrodynamics picture are discussed. Last, the decoherence with master equation formalism and dephasing with low frequency flux noise are discussed.

In Chapter 3, the design and the model for capacitively shunted flux qubits are given. The design consist of a coplanar waveguide resonator and flux qubits with all three junctions shunted by large capacitor pads. The model is based on the complete capacitive structure of the design. The electromagnetic (EM) response of the coupled resonator-qubit system and the capacitance matrix of the system is simulated with EM simulation tools. The qubit characteristics are then calculated with the circuit model using EM simulation results and fabrication parameters as input parameters. Lastly, device fabrication methods and procedures are discussed.

In Chapter 4, the experimental characterization of the shunted flux qubit is given. First, transmission spectrum of the coupled qubit resonator system is presented and the readout characteristics are discussed. Next, the energy level spectrum of the qubit is determined by spectroscopy experiments and the transition frequencies are shown for a range of magnetic flux. Next, driven Rabi oscillations on the states identified by spectroscopy are demonstrated at various flux bias points. Last, a method for determining the state populations is discussed.

In Chapter 5, coherence characterization for the qubit system including energy relaxation and dephasing analysis with Ramsey, spin-echo, and dynamical decoupling methods are presented at various flux bias points. In addition, decoherence rates are determined for the multi-level system formed by the lowest three energy levels. Next, fast and high fidelity single qubit gates are demonstrated and the fidelity of the gates are studied with randomized benchmarking protocol.

In Chapter 6, quantum state tomography and multi-level control are presented. Multi-

level control utilizes resonant transitions and two photon transition from ground state to second excited state. Therefore, Rabi oscillations between states 0 and 2 with two-photon process are presented in this chapter. In addition, the experimental implementation of a generalized Walsh-Hadamard gate is demonstrated. The gate Hamiltonian is decomposed into two unitary operators. The unitary operators are implemented by simultaneous driving of the qutrit transitions and adjusting the drive phases. Last, numerical simulations of the gate is compared to the experimental results and potential limitations are discussed.

In Chapter 7, the concluding remarks of the thesis and the future work are discussed.

Chapter 2

Theoretical background

In this chapter, the general theoretical background for the experiments with capacitively shunted flux qubits is given. In the first section, a brief introduction to superconducting microwave resonators is presented. In the second section, Josephson junctions,the building blocks of superconducting qubits, are discussed. In the third section, superconducting qubit types are introduced with a focus on flux qubits. In the fourth section, a general introduction to qubit control is given. In the fifth section, the coupled resonator and qubit system is studied with circuit quantum electrodynamics approach. In the last section, the decoherence of superconducting qubits are discussed.

2.1 Superconducting microwave resonators

Superconducting resonators play a significant role in quantum computation and information and they are used in many applications such as radiation detection [22, 23] and parametric amplification [24]. In quantum computation, superconducting resonators are mainly used for qubit state readout [25], qubit control [26], and qubit-qubit coupling mechanisms [27]. In this section, we first introduce lumped element resonators. Next, the basics

of the transmission lines and distributed resonators are given. Finally, coplanar microwave resonators are discussed.

2.1.1 Lumped element resonators

A simple resonator can be built by lumped circuit elements, consisting of resistors, inductors, and capacitors, placed in series or in parallel. Figure 2.1 depicts the series and parallel RLC circuits. The complex impedance of the serial circuit is expressed as

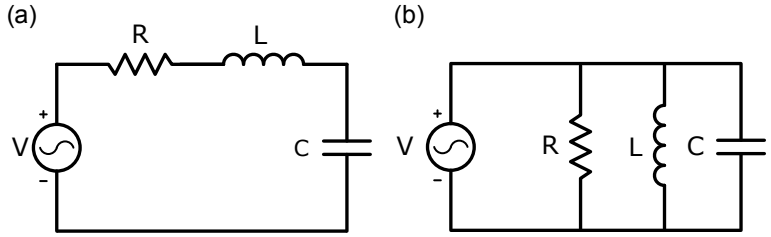

Figure 2.1: Circuit representations of lumped element resonators. a) Series RLC circuit. b) Parallel RLC circuit

$$Z(i\omega) = R + i\omega L + \frac{1}{i\omega C}, \tag{2.1}$$

where R, L, and C are resistor, inductor and capacitor respectively and ω is the angular frequency of the input signal. The impedance expression for parallel circuit is similarly expressed as

$$Z(i\omega) = \left(\frac{1}{R} + \frac{1}{i\omega L} + i\omega C\right)^{-1}. \tag{2.2}$$

The resonance occurs when the time average energies of the stored electric and magnetic field are equal to each other. This condition is satisfied when $\omega = \omega_0 = 1/\sqrt{LC}$, leading to complex impedance Z to be real. The average stored energies when on resonance are

$$\begin{aligned} W_C &= W_L, \\ \frac{1}{4}CV_C^2 &= \frac{1}{4}LI_L^2. \end{aligned} \tag{2.3}$$

In a resonator, the loss is associated with the resistive element R and the corresponding energy is given as

$$W_R = \frac{1}{2} R I_R^2. \tag{2.4}$$

One important measure of a resonator is called quality factor Q. Basically, the quality factor describes the life time of the stored energy in the resonator. The simple form of the Q is given as [28],

$$Q = \omega \frac{\text{Average energy stored in the resonator}}{\text{Energy loss per cycle}}. \tag{2.5}$$

For the series RLC circuit, the Q is found as

$$Q = \frac{\omega_0 L}{R}. \tag{2.6}$$

Similarly for the parallel RLC circuits,

$$Q = \omega_0 R C. \tag{2.7}$$

Quantization of LC resonator

In this section the quantum LC resonator is discussed. The classical Hamiltonian of the lumped element LC resonator can be expressed as

$$H = \frac{1}{2} C V^2 + \frac{1}{2} L I^2, \tag{2.8}$$

where V is the voltage on the capacitor C and I is the current on the inductor. Using generalized coordinates and replacing the terms in the Hamiltonian as charge on the capacitor $q = CV$ and the flux on the inductor $\phi = LI$, the Hamiltonian can be written as

$$H = \frac{q^2}{2C} + \frac{\phi^2}{2L}. \tag{2.9}$$

In quantum picture, the classical quantities of charge and flux are replaced by their corresponding quantum operators $q \to \hat{q}$ and $\phi \to \hat{\phi}$. The quantum Hamiltonian is then expressed as

$$\hat{H} = \frac{\hat{q}^2}{2C} + \frac{\hat{\phi}^2}{2L}. \tag{2.10}$$

The operators $\hat{q}$ and $\hat{\phi}$ have a commutation relation $[\hat{q}, \hat{\phi}] = i2e\hbar$ and are canonically conjugated. We introduce the dimensionless annihilation and creation operators as,

$$\hat{a} = \frac{1}{\sqrt{2\hbar\omega_0 C}}(\hat{q} + iC\omega_0\hat{\phi}) \tag{2.11}$$

$$\hat{a}^\dagger = \frac{1}{\sqrt{2\hbar\omega_0 C}}(\hat{q} - iC\omega_0\hat{\phi}). \tag{2.12}$$

The annihilation and creation operator have the commutation relation $[\hat{a}, \hat{a^\dagger}] = 1$. We can rewrite the Hamiltonian as

$$\hat{H} = \hbar\omega_0(\hat{a}^\dagger\hat{a} + \frac{1}{2}). \tag{2.13}$$

This is the Hamiltonian of a harmonic oscillator. The non-Hermitian annihilation and creation operators do not correspond to measurable quantities however they are useful in operations on photon number states $|n\rangle$, where $n = \hat{n}|n\rangle$ represents the number of photons stored in the resonator with the number operator $\hat{n} = \hat{a}^\dagger\hat{a}$. The action of the annihilation and creation operators on number states are

$$\begin{aligned} \hat{a}|n\rangle &= \sqrt{n}|n-1\rangle, \\ \hat{a}^\dagger|n\rangle &= \sqrt{n+1}|n+1\rangle. \end{aligned} \tag{2.14}$$

2.1.2 Transmission lines

Microwave resonators are quite useful tools to probe any circuitry they are coupled to. Typically, a resonator can be implemented by using either lumped circuit elements or

distributed elements in the form of transmission lines. Unlike the circuit theory, the transmission line theory deals with devices having dimensions comparable to the wavelength of the frequency of interest. In this case, voltage and current can vary significantly over the device dimensions. Therefore, transmission lines are modeled as systems consisting of distributed elements of capacitors, inductors, resistors, and conductors. For infinitely small lengths, transmission lines can be treated as circuits with lumped unit elements. Figure 2.2 shows a section of a typical transmission line having two conductors with length Δz.

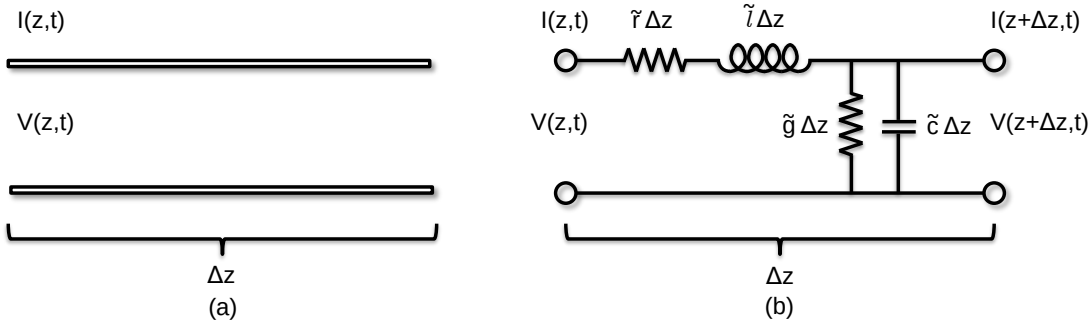

Figure 2.2: a) Infinitely small part of a two conductor transmission line. b) Lumped element model of the transmission line shown in (a).

Here, $\tilde{r}$ is the series resistance per unit length. Similarly $\tilde{l}$, $\tilde{g}$, and $\tilde{c}$ are series inductance, shunt conductance and shunt capacitance per unit length respectively. When Kirchhoff's voltage and current laws are applied to circuit shown in Fig. 2.2(b), corresponding wave equations for the voltage and the current can be found as [28]

$$V(z) = V_0^+ e^{-\gamma_p z} + V_0^- e^{\gamma_p z} \tag{2.15}$$

$$I(z) = I_0^+ e^{-\gamma_p z} + I_0^- e^{\gamma_p z}, \tag{2.16}$$

where $\gamma_p = \alpha + i\beta = \sqrt{(\tilde{r} + i\omega\tilde{l})(\tilde{g} + i\omega\tilde{c})}$ is the propagation constant and ω is the angular frequency. The real part of the propagation constant governs the dissipative loss of the resistive and conductive elements where the imaginary part associates with electromagnetic radiation. If the loss on the line is neglected, propagation constant becomes $\gamma_p = i\beta$, $\beta =$

$\omega\sqrt{\tilde{l}\tilde{c}}$. Introducing $Z_0 = \frac{V_0^+}{I_0^+} = \frac{V_0^-}{I_0^-}$ as characteristic impedance and reflection coefficient $\Gamma(l) = \Gamma e^{(-2\gamma_p l)}$, the wave equations are then expressed as [28]

$$V(z) = V_0^+(e^{-\gamma_p z} + \Gamma e^{\gamma_p z}) \tag{2.17}$$

$$I(z) = \frac{V_0^+}{Z_0}(e^{-\gamma_p z} - \Gamma e^{\gamma_p z}). \tag{2.18}$$

The input impedance at distance l away from the load is given as [28]

$$Z_{in} = Z_0 \frac{Z_L + Z_0 \tanh \gamma l}{Z_0 + Z_L \tanh \gamma l}, \tag{2.19}$$

where Z_L is the load terminates the transmission line.

We are interested in a special case of transmission lines. In this case both ends of the finite transmission line of length l is open ended. The boundary conditions are $I(0) = I(l) = 0$ and the load impedance $Z_L \to \infty$. In this case we have reflection coefficient $\Gamma = 1$. Using Eq. 2.18 and the boundary conditions,

$$\sin(\beta l) = 0 \tag{2.20}$$

$$\beta = \frac{m\pi}{l}, \quad m \in \mathbb{N}. \tag{2.21}$$

The phase velocity $\nu_p = 1/\sqrt{\tilde{l}\tilde{c}}$ and with $\omega = 2\pi\lambda^{-1}\nu_p$ we find that

$$\lambda_m = \frac{2l}{m}. \tag{2.22}$$

Equation 2.22 indicates that the wavelength of the standing wave in the resonator is related to the length of this finite transmission line. For $m = 1$, we have the fundamental resonance mode, with frequency ω_0. Around its resonance frequency $\omega = \omega_0 + \Delta\omega$, βl can be written as $\beta l = \pi(1 + \frac{\Delta\omega}{\omega_0})$. Assuming the losses are negligible, the input impedance for the open

ended transmission line can we written as

$$Z_{\text{in}} \approx \frac{Z_0}{\alpha l + i\frac{\pi\Delta\omega}{\omega_0}}. \tag{2.23}$$

This equation is analogous to a lumped element parallel RLC oscillator. Therefore, around the resonance frequency, open ended transmission line can be approximated by a parallel RLC resonator.

2.1.3 Coplanar waveguide resonators

A typical coplanar waveguide resonator(CPW) section is shown in Fig. 2.3. It consists of a center signal conductor line and two ground conductor planes sitting on top of a substrate. Since all the conductors are in the same plane, it makes it easier to fabricate coplanar structures of desired parameters.

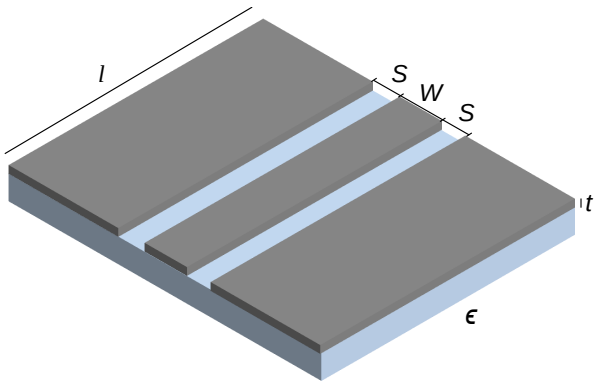

Figure 2.3: A sketch of a coplanar waveguide structure. Capacitances are formed between the central signal line and the ground planes. The geometric inductance is dependent on the geometry of the CPW structure.

Electrical dynamics of CPW resonators with transverse electric and magnetic mode are explained well by transmission line theory. In order to find the circuit elements such as capacitance per unit length and inductance per unit length, conformal mapping techniques

can be applied and they are given as [29]

$$\tilde{l} = \frac{\mu_0}{4}\frac{K(k_0')}{K(k_0)} \tag{2.24}$$

$$\tilde{c} = 4\epsilon_0\epsilon_{eff}\frac{K(k_0)}{K(k_0')}, \tag{2.25}$$

where $\epsilon_{eff} = ((\epsilon + 1)/2)$ is the effective dielectric constant. The arguments for complete elliptic integral of first kind K are given as

$$k_0 = \frac{w}{w + 2s} \tag{2.26}$$

$$k_0' = \sqrt{1 - k_0^2}, \tag{2.27}$$

where w and s are the CPW resonator center line width and the gap between center line and ground planes, shown in Fig. 2.3.

In order to realize the half-wavelength resonators described in the previous section, coupling capacitors are placed at each end of the transmission line. These capacitors, leaving the transmission line open ended, can couple the resonator to other circuits such as measurement tools. For the case of the quarter wavelength resonators, the center conductor line is shorted to ground planes at one end of the line whereas the other end is terminated by a capacitor. Figure 2.4 depicts these two basic CPW resonators. The resonance frequencies for mode m of half-wavelength resonator is given by $f_m = \frac{m}{2\pi 2l\sqrt{LC}}$ and for quarter wavelength resonators, $f_m = \frac{m}{2\pi 4l\sqrt{LC}}$.

For the case of superconducting electrodes, it is expected to have high quality factor resonators because the loss associated with the resistive elements are negligible. Superconductor CPW resonators are reported to have quality factors around 10^6 [30, 31, 32]. When dealing with superconductor CPW resonators, the total inductance should also accommodate for the inertia of the moving Cooper pairs since they have large relaxation times. This kinetic inductance of Cooper pairs is temperature dependent contributes to the total inductance of the superconducting CPW resonator.

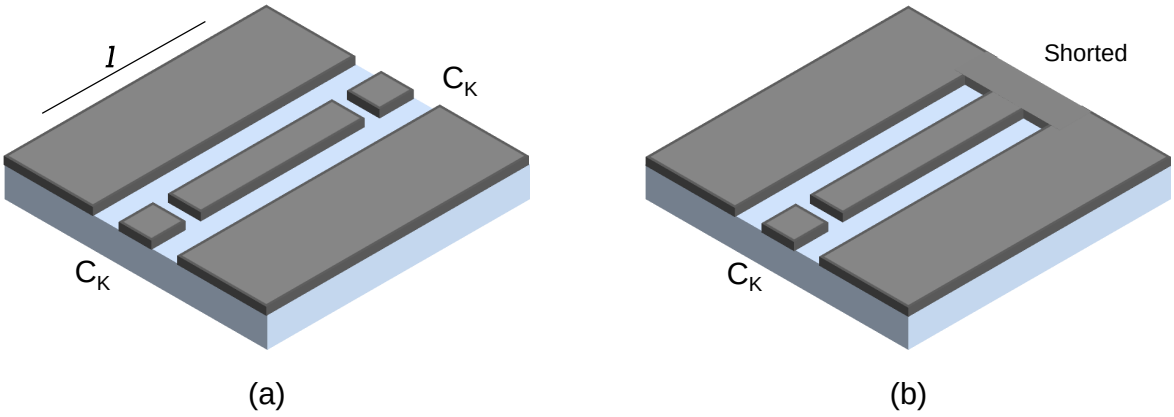

Figure 2.4: Sketch of terminated transmission lines. a) Coupling capacitors C_K at both ends defines a half-wavelength resonator for the fundamental mode. b) Shorting one end and placing a capacitor on the other end defines a quarter-wavelength resonator. Dimensions are not to scale.

Quantization of CPW resonator

A half-wavelength CPW resonator is treated as a transmission line with open-circuit boundary conditions at both ends of the line. The transmission line can be considered as a chain of lumped element LC resonators [28] (Fig. 2.5). The Lagrangian of the system can be written as

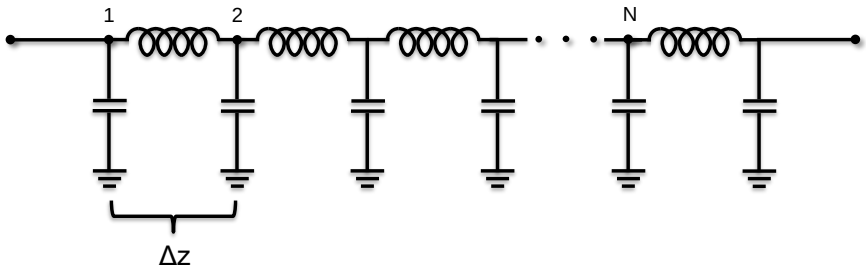

Figure 2.5: Schematic diagram of a transmission line modeled as chain of LC resonators.

$$\mathcal{L} = \sum_{i=1}^{N} \frac{1}{2}\tilde{c}\Delta z\dot{\phi}_i^2 - \sum_{i=1}^{N-1} \frac{1}{2}\frac{(\phi_{i+1}-\phi_i)^2}{2\tilde{l}\Delta z}, \tag{2.28}$$

where $\tilde{c}$ and $\tilde{l}$ are the capacitance and inductance per unit length. For $N \to \infty$ Eq.2.28 becomes

$$\mathcal{L} = \int_0^l \left[\frac{\tilde{c}\dot{\phi}(z,t)^2}{2} - \frac{1}{2\tilde{l}} \left(\frac{\partial \phi(z,t)}{\partial z} \right)^2 \right] dz. \tag{2.29}$$

For this case the Euler-Lagrange equation is

$$\nu_p^2 \frac{\partial^2 \phi(z,t)}{\partial t^2} = \frac{\partial^2 \phi(z,t)}{\partial z^2}. \tag{2.30}$$

Where $\nu_p = 1/\sqrt{\tilde{l}\tilde{c}}$. The general solution for the wave equation is

$$\phi(z,t) = \sum_{m=1}^{\infty} A_m \cos(k_m z + \alpha_m) \cos(k_m \nu_p t + \beta_m). \tag{2.31}$$

Remembering the boundary conditions $I(0,t) = I(l,t) = 0$, substituting the solution into Eq.2.29 and carrying out the integrations, the Lagrangian is found as

$$\mathcal{L} = \sum_{m=1} \frac{\tilde{c}l\dot{\phi}(t)_m^2}{4} - \frac{m^2\pi^2\phi(t)_m^2}{4\tilde{l}} \tag{2.32}$$

where $\phi(t)_m = A_m \cos(\frac{m\pi t}{l} + \beta_m)$. The Lagrangian takes a familiar form of a system of LC resonators with $C_m = Cl/2$ and $L_m = 2lL/m^2\pi^2$ as

$$\mathcal{L} = \sum_{m=1} \frac{C_m\dot{\phi}(t)_m^2}{2} - \frac{\phi(t)_m^2}{2L_m}. \tag{2.33}$$

Carrying out the Legendre transformation, the Hamiltonian of the CPW structure is obtained as [33]

$$H = \sum_{m=1} \hbar\omega_m (a_m^\dagger a_m + \frac{1}{2}), \tag{2.34}$$

where $\omega_m = m\nu_p\pi/l$ is the mode resonance frequencies. For fundamental mode ($m = 0$), the Hamiltonian simplifies to Eq. 2.13 in quantum picture.

Transmission measurement of CPW resonators

When a half-wavelength resonator is biased by an external microwave source, the signal transmitted through the resonator depends on the frequency of the bias. The transmitted signal is maximum when the drive frequency is equal to the resonance frequency, and it is diminished away from the resonance. The behavior of the transmitted signal has a Lorentzian shape and can be fitted by [34]

$$F(f) = A_0 \frac{\delta f}{(f - f_0)^2 + (\delta f/2)^2}, \tag{2.35}$$

where f is the frequency of the signal with $2\pi f = \omega$, δf is the full width half-maximum, and A_0 is the transmission amplitude. The corresponding quality factor of the resonator is $Q_L = f_0/\delta f$.

The transmission and reflection characterization of the CPW resonators can be analyzed with the scattering matrix of the circuit. It describes the relations of the incident and outgoing signals on the ports of the circuit. For a two port circuit, the scattering matrix is expressed as

$$\begin{bmatrix} V_1^- \\ V_2^- \end{bmatrix} = \begin{bmatrix} S_{11} & S_{12} \\ S_{21} & S_{22} \end{bmatrix} \begin{bmatrix} V_1^+ \\ V_2^+ \end{bmatrix}. \tag{2.36}$$

In this expression, the incident wave on a port is indicated with a (+) sign whereas wave leaving the port is indicated by a (-) sign. The S matrix elements are found by biasing one of the ports and measuring the signal on the port of interest while no bias is applied on the other ports. For example, the S_{12} element of the scattering matrix relates how much of the input signal on port $1(V_1^-)$ ends up on the port 2 (V_2^+). From circuit and transmission line theory, the impedance matrix of a two-port network matrix can be constructed and the scattering matrix of the network related to the impedance matrix can be calculated [28].

2.2 The Josephson junction

Josephson junctions play a significant role in superconducting quantum devices. A Josephson junction is formed by interrupting two superconductors by a thin tunnel barrier. The barrier material is typically an insulator however normal metals and constrictions on geometry can be used as a barrier.

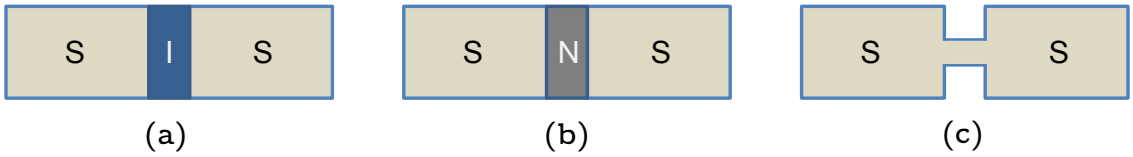

Figure 2.6: Implementations of Josephson junctions. Illustrations of a) superconductor-insulator-superconductor, b) superconductor-metal-superconductor, and c) superconductor-bridge-superconductor junctions.

In 1962, Brian Josephson predicted that a dissipationless current can flow between superconducting electrodes separated by a barrier in the form of Cooper pair tunneling [35]. The superconducting island can be described by a macroscopic wave function $\Psi = \Psi_0 e^{i\varphi}$, where φ is the superconducting phase and ψ_0 is the amplitude associated with the Cooper pair density. This tunneling current is given by

$$I_s = I_c \sin\gamma, \tag{2.37}$$

where I_c is the junction critical current above which the supercurrent vanishes, and γ is the gauge invariant phase difference between the wave functions of the two superconducting electrodes ($\gamma = \varphi_1 - \varphi_2$). This equation is known as the first Josephson relation. Josephson also predicted that the phase evolves in time with a voltage bias across the junction as

$$V = \frac{\hbar}{2e}\frac{d(\gamma)}{dt}. \tag{2.38}$$

When the time derivative of the Eq. 2.37 is considered and with the help of second Josephson relation

$$\frac{dI_s}{dt} = I_c \cos(\gamma) \frac{2e}{\hbar} V \tag{2.39}$$

is obtained. This equation relates the time derivative of the current to voltage indicating an inductive element behaviour. With $V = L\frac{dI}{dt}$, the Josephson inductance can be expressed as

$$L_J = \frac{\varphi_0}{I_c \cos\gamma}. \tag{2.40}$$

where φ_0 is the reduced magnetic flux quantum $\varphi_0 = \Phi_0/2\pi = \hbar/2e$. Equation 2.40 suggest that the inductance value is non-linear due to the cosine term and it depends on the phase difference γ. This non-linear inductance plays a significant role in practical applications of superconductors.

The RCSJ model

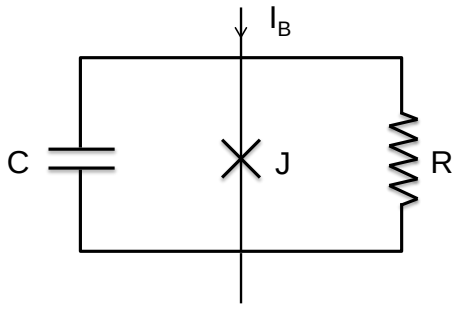

Figure 2.7: Schematic diagram of the RCSJ model of a Josephson junction. The junction is represented by a cross and it is shunted by a resistor R and a capacitor C. The bias current is denoted with I_B.

A Josephson junction can be modeled as a resistively capacitively shunted junction (Fig 2.7) [36]. In practice, apart from Cooper pair tunneling there are other contributions to the current due to resistive and capacitive channels. Since the junction itself forms a capacitance, a displacement current can contribute to the current. The resistive channel

represents the tunneling of excited quasiparticles in superconductor. The shunting of the junction can be explicit as well by adding external circuit elements. The total current can be written as

$$I_B = I_c \sin\gamma + C\frac{dV}{dt} + \frac{V}{R}, \tag{2.41}$$

where I_B is the bias current. With the help of Josephson relations, the above equation can be rewritten as

$$I_B = I_c \sin\gamma + \frac{\Phi_0 C}{2\pi}\frac{d^2\gamma}{dt^2} + \frac{\Phi_0}{2\pi R}\frac{d\gamma}{dt}. \tag{2.42}$$

The Lagrangian of a system is quite useful to find the equations of motion describing the circuit. The Lagrange equation with the gauge invariant phase difference γ as a generalized coordinate is

$$\frac{d}{dt}\left(\frac{\partial\mathcal{L}}{\partial\dot{\gamma}}\right) - \frac{\partial\mathcal{L}}{\partial\gamma} = 0. \tag{2.43}$$

Ignoring the resistive channel, the Lagrangian $\mathcal{L}$, can be guessed as

$$\mathcal{L} = \frac{1}{2}C\left(\frac{\Phi_0}{2\pi}\right)^2\dot{\gamma}^2 + \frac{\Phi_0}{2\pi}(I_c\cos\gamma + I_B\gamma). \tag{2.44}$$

The corresponding conjugate momentum is found as

$$p_\gamma = \frac{\partial\mathcal{L}}{\partial\dot{\gamma}} = C(\frac{\Phi_0}{2\pi})^2\dot{\gamma}. \tag{2.45}$$

The Hamiltonian of the driven Josephson junction can be found by applying the Legendre transformation

$$H(p_\gamma,\gamma) = p_\gamma\dot{\gamma} - \mathcal{L}(\gamma,\dot{\gamma}). \tag{2.46}$$

After the transformation the Hamiltonian is found as

$$H(p_\gamma,\gamma) = \frac{1}{2C}\big(\frac{2\pi}{\Phi_0}\big)^2 p_\gamma^2 - \frac{\Phi_0}{2\pi}(I_c\cos\gamma + I_B\gamma). \tag{2.47}$$

Quantum Hamiltonian of a Josephson junction

To treat the system quantum mechanically, conjugate variables γ and p_γ in Hamiltonian 2.46 are replaced with operators $\hat{\gamma}$ and $\hat{p_\gamma}$ respectively. It can be shown that $\hat{\gamma}$ and $\hat{p_\gamma}$ have the commutation relation $[\hat{\gamma}, \hat{p_\gamma}] = i\hbar$. Introducing the charging energy of the junction as $E_C = \frac{(2e)^2}{2C}$ and Josephson energy as $E_J = \frac{\Phi_0}{2\pi} I_c$ and assuming the bias current $I_B = 0$, the Josephson junction Hamiltonian in phase basis is expressed as

$$\hat{H} = \frac{E_C}{\hbar^2} \hat{p_\gamma}^2 - E_J \cos\hat{\gamma}. \tag{2.48}$$

It is often useful to the express the Hamiltonian in the charge basis. The momentum operator in Eq. 2.48 can be expressed in terms of the charge operator $\hat{q}$. The charge is associated with the number of Cooper pairs on the capacitor, $\hat{q} = 2e\hat{n}$ where $\hat{n}$ is the number operator. Therefore,

$$\hat{p_\gamma} = \frac{\Phi_0}{2\pi}\hat{q} = \frac{\hbar}{2e} 2e\hat{n} = \hbar\hat{n}. \tag{2.49}$$

It is also useful to express the potential term in exponential form

$$E_J \cos\hat{\gamma} = E_J \frac{e^{i\hat{\gamma}} + e^{-i\hat{\gamma}}}{2}. \tag{2.50}$$

In the charge representation $e^{\pm i\hat{\gamma}}$ is expressed as

$$e^{\pm i\hat{\gamma}} = \sum_n e^{\pm i\hat{\gamma}} |n\rangle\langle n| = \sum_n |n \mp 1\rangle\langle n|. \tag{2.51}$$

As a result, the Hamiltonian in the charge representation is

$$\hat{H} = E_C \hat{n}^2 + \frac{E_J}{2} \sum_n |n-1\rangle\langle n| + |n+1\rangle\langle n|. \tag{2.52}$$

It can be shown that $\hat{\gamma}$ and $\hat{n}$ do not commute as $[\hat{\gamma}, \hat{n}] = i$. They obey the uncertainty

relation and they can not be known exactly simultaneously. If the ratio of $\frac{E_J}{E_C} \gg 1$ than the fluctuations in charge are big and phase variance is small. The phase value is well defined. On the other hand, if $\frac{E_J}{E_C} \ll 1$ then the phase variation is large and charge is well defined. Both E_C and E_J are tunable parameters and can be adjusted during fabrication.

The potential energy of the Josephson junction is due to nonlinear inductive element. However, for small γ values in the cosine term, the expression is approximated as $\cos\gamma \approx 1 - \frac{\gamma^2}{2}$. For this case the potential is parabolic and the Hamiltonian of the Josephson junction is analogous to LC harmonic oscillator. For a harmonic oscillator, subsequent energy level differences are equal to each other. The Josephson junction potential energy consists of nonlinear element and the energy levels in this potential are anharmonic. This anharmonic energy level property plays an important role in superconducting quantum devices.

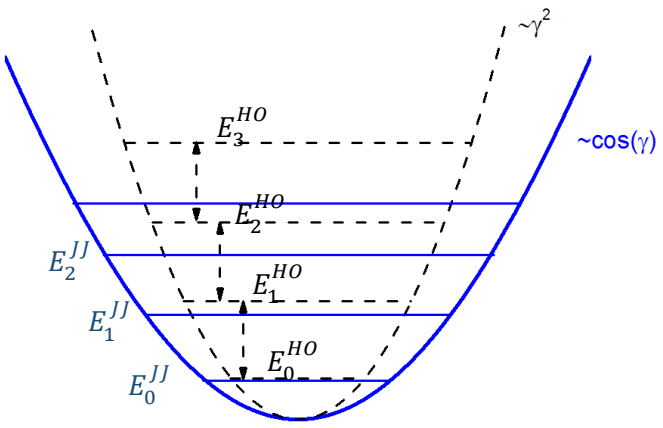

Figure 2.8: Energy level representation of a LC harmonic oscillator (dashed lines) and a Josephson junction (solid lines).

Ambegaokar-Baratoff relation

The Ambegaokar-Baratoff formula relates the critical current of a Josephson junction to the BCS energy gap Δ_{BCS} [37] and the normal state conduction of the Josephson junction. This is a very useful relation because, for known superconductor gap Δ_{BCS}, one can find the E_J of the Josephson junction just by measuring the resistance of the junction R_n at room temperature. Assuming the junction consisting of only one type of superconductor, For any temperature T, the Ambegaokar-Baratoff relation is given as [38]

$$I_c R_n = (\frac{\pi \Delta_{\mathrm{BCS}}}{2e}) \tanh(\frac{\Delta_{\mathrm{BCS}}}{2kT}). \tag{2.53}$$

This relation is useful to determine the relation between the critical current and resistance, with the latter easily characterized during the fabrication process.

2.3 Superconducting qubits

In order for a system to be considered as a practical qubit, it is expected to satisfy certain conditions. According to DiVincenzo [39], first, the qubit has to have the ability to be initialized to a known state. Second, there must exist single qubit operators to manipulate the state of the qubit. Third, to realize universal set of quantum gates, the qubit has to be applicable for two qubit operations. Fourth, the system should exhibit long coherence times in which the quantum algorithm or protocol finishes successfully. Lastly, the system should allow for a qubit-specific measurement.

Superconducting qubits are based on Josephson junctions and have an important share in quantum computation. They are macroscopic objects demonstrating quantum effects on large scales. As investigated in the previous sections, Josephson junctions have anharmonic energy states. For instance, the two lowest states can be candidates for a qubit implementation. Being macroscopic objects, it is easy to utilize the fabrication methods in micro- and nano-technology to realize the Josephson junctions of desired parameters and it

is also quite flexible to couple to the external circuits for state manipulation and readout.

In the next subsections, specific types of Josephson junctions, namely the phase qubit, the charge qubit, and the flux qubit are discussed, respectively.

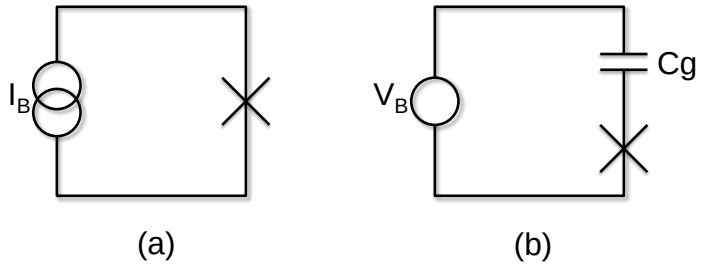

Figure 2.9: The phase and the charge qubit. a) Circuit representation of a the phase qubit. The Josephson junction (illustrated as cross) is biased with a DC current source. b) Circuit representation of a the charge qubit. The Josephson junction is isolated by a gate capacitor C_g and biased by a gate voltage V_B.

2.3.1 The phase qubit

The phase qubit is basically a Josephson junction biased with a current $I_B < I_c$ as shown on Fig. 2.9(a). The Hamiltonian of a driven junction is derived in Eq. 2.46. The potential term in the Hamiltonian is nonlinear and it resembles a particle moving in the tilted washboard potential. The tilting of the potential is controlled by the bias current and the number of energy levels in the local potential depends on the value of the I_B.

Phase qubits are typically biased very close to the critical current of the junction ($I_B \approx 99\% I_c$) which leads to few energy levels in the potential well. Bias current modifies the potential well structure and affects the anharmonicity of the energy levels. As the potential gets tilted the anharmonicity increases. Considering two energy levels in the well, after some waiting time quantum tunneling occurs if the qubit is in the excited state and no tunneling observed for the ground state. This is because the excited state sees a smaller

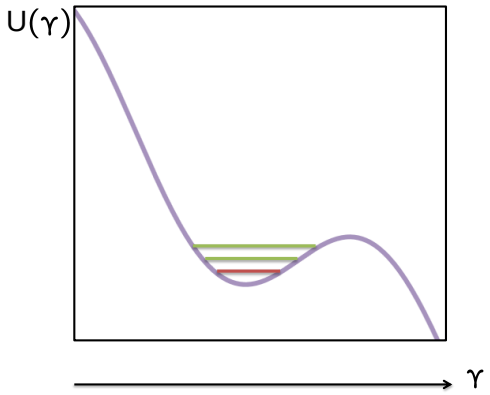

Figure 2.10: Potential energy of the phase qubit. The first few energy states are localized in the potential well. The energy level splitting and the barrier height is determined by the biased current I_B. The tunneling probability is higher for the higher energy levels.

potential barrier than the ground state. This builds the basic idea of the state read-out of the phase qubit.

2.3.2 The charge qubit

The charge qubit circuit is shown in Fig. 2.9(b). It consists of a superconducting island isolated from a voltage source by a gate capacitor and from a gate electrode through a junction. The Hamiltonian of the charge qubit is similar to Hamiltonian of a Josephson junction expressed in Eq. 2.52. However, one needs to include the charges on the gate capacitor. Introducing $n_g = \frac{-C_g V_B}{2|e|}$ as gate charge and $C_\Sigma = C_g + C$, the Hamiltonian of a charge qubit in charge basis is expressed as

$$H = E_C(n - n_g)^2 - \frac{Ej}{2}\sum_n |n-1\rangle\langle n| + |n+1\rangle\langle n|, \tag{2.54}$$

where $E_C = \frac{(2e)^2}{2C_\Sigma}$. The energy levels of the charge qubit can be calculated for two cases. For the first case, where $E_C \gg E_J$, the Hamiltonian is dominated by the first term and the

Josephson energy can be considered as small perturbation. As seen form Fig. 2.11(a), the energy levels are strongly dependent on gate charge. Fluctuations in the charge are very important in this regime. For the reverse case, where $E_J \gg E_C$, the energy levels of the charge qubit become less dependent on the gate charge. On the contrary, the anharmonicity is reduced. Overall the change in the anharmonicity is lower than the change in the charge dependency of the qubit [17]. A simple way to change the ratio of E_J/E_C is to add a shunting capacitor to the junction which modifies charging energy E_C.

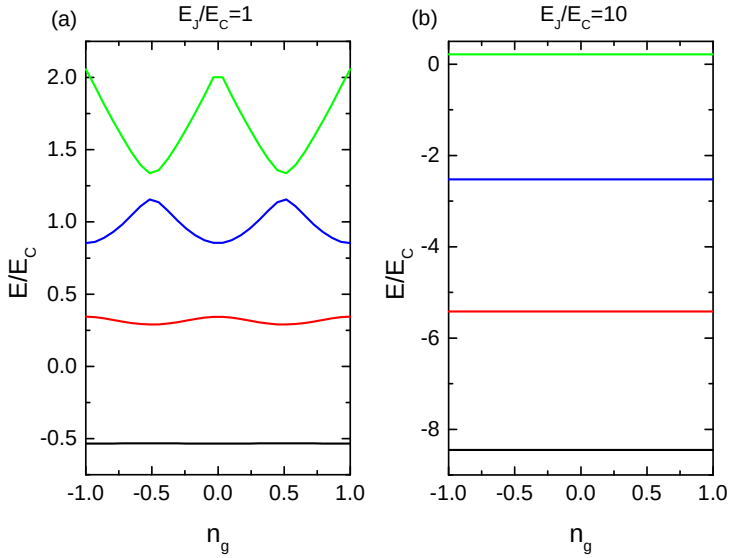

Figure 2.11: Charge qubit energy level structure. The first four energy levels with varying E_J/E_C ratios for a) $E_J/E_C = 1$, and b) $E_J/E_C = 50$. In the regime $E_J/E_C = 1$, the energy levels are strongly dependent on the gate charge compared to the case where $E_J/E_C = 50$. The anharmonicity is decreasing with the increasing E_J/E_C.

2.3.3 The flux qubit

The flux qubit contains a superconducting loop interrupted by at least one Josephson junction [18]. The qubit is operated close to an applied magnetic flux of half a flux quantum, and at this point, the potential energy has two wells separated by a tunneling

barrier. In the quantum picture, the tunneling can occur between the wells and this lifts the degeneracy between two lowest state of each potential wells. This design is prone to the dephasing due to the flux fluctuations since the loop inductance is high and it strongly couples the qubit to the environment. This problem is solved by using Josephson junctions to replace loop inductance to realize flux qubits with smaller loops. Therefore, flux qubit with three junction design [40] is quite common.

The circuit analysis of a persistent current qubit

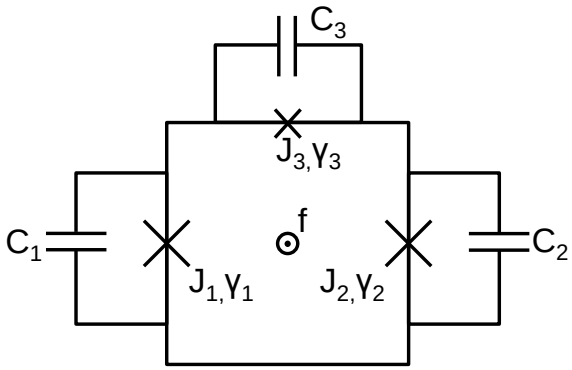

Figure 2.12: A schematic circuit representation of the persistent current qubit. The superconducting loop is interrupted by three Josephson junctions. One of the junctions, J_3 is called the α junction and it has $E_{C3} = \alpha^{-1} E_{C1}$ and $E_{J3} = \alpha E_{J1}$ where typically $0.5 < \alpha < 1$.

The persistent current qubit circuit is shown in Fig. 2.12. The small inductance loop is interrupted by three Josephson junctions. The Hamiltonian of the system has three phase degree of freedoms. However, since the macroscopic wave function must be single valued, the phase along the loop must be an integer multiple of 2π. This imposes a flux quantization condition

$$\sum_i \gamma_i + 2\pi f = 2\pi n, n \in \mathbb{N} \tag{2.55}$$

where γ_i is the phase difference across junction J_i and $f = \frac{\Phi_{ext}}{\Phi_0}$ is the external magnetic frustration. The junction sizes are selected such that the small junction is α times smaller

than the two identical junctions. The characteristic energies of the smaller junction is rescaled by α since the junction critical current scales with the area. The potential energy is then expressed as

$$U_J = -E_J(\cos\gamma_1 + \cos\gamma_2 + \alpha\cos\gamma_3). \tag{2.56}$$

By applying the flux quantization condition, the number of degrees of freedom reduced to two and the potential energy can be expressed as

$$U_J = -E_J(\cos\gamma_1 + \cos\gamma_2 + \alpha\cos(2\pi f + \gamma_1 + \gamma_2)). \tag{2.57}$$

The applied external flux modifies the shape of the potential well. Figure 2.13 depicts the potential energy of a PCQ under three external flux values of $f = 0.485$, $f = 0.5$, and $f = 0.515$. The two potential minima (darkest regions) along $\gamma_1 = \gamma_2$, and the induced asymmetry by the applied flux can be clearly seen.

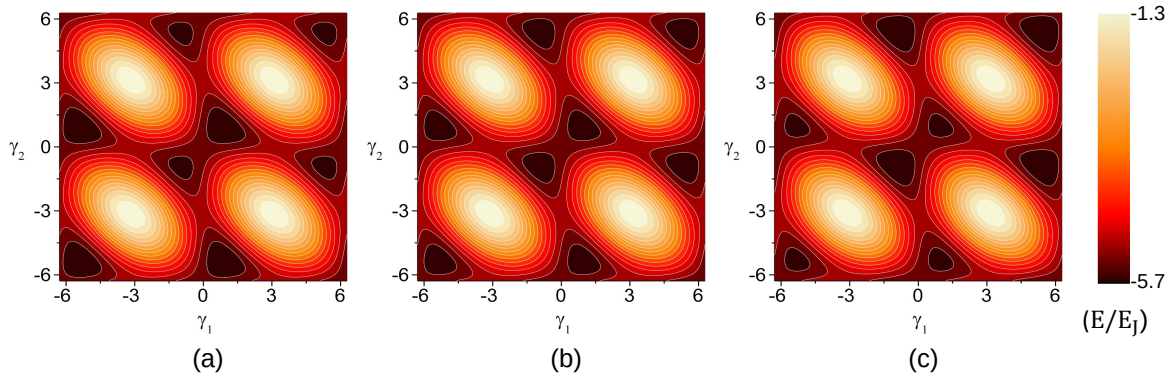

Figure 2.13: Potential energy of the flux qubit. The energy is plotted with phase differences γ_1 and γ_2 for a) $f = 0.485$ b) $f = 0.5$ and c) $f = 0.515$. Darker regions corresponds potential minima.

The flux qubit is operated near half a flux quantum. Classically, the lowest energy states of the persistent current qubit are located at the minima of these potential wells and they are degenerate at the symmetry point, $f = 0.5$. If the potential energy equation is further inspected, it can be found that the potential barrier between two well along the

line $\gamma_1 = \gamma_2$ depends on the α junction, which can be defined by the geometry during fabrication. The modulation of the barrier can be seen on Fig. 2.14.

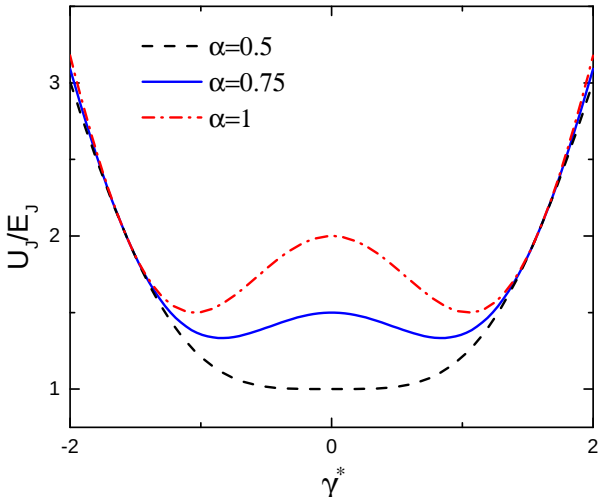

Figure 2.14: Modulation of the potential barrier of the flux qubit between two potential wells along the line $\gamma^* = \gamma_1 = \gamma_2$ for $\alpha = 0.5, 0.75$, and 1.

Away from the symmetry point, the double potential well is tilted. In this case, the energy associated with the persistent current is given as

$$\epsilon = 2I_c(\Phi_{ext} - \frac{\Phi_0}{2}). \tag{2.58}$$

To describe the dynamics of the persistent current qubit, the kinetic energy of the system should be considered. It is due to the electrostatic energy stored in the capacitive elements of the circuit. The kinetic energy for the three-junction flux qubit can be found as

$$T = \frac{1}{2}\sum_i C_i V_i^2. \tag{2.59}$$

Using the second Josephson relation, the kinetic energy can be expressed as [40]

$$T = \frac{1}{2}\frac{\Phi_0}{2\pi}^2 \begin{pmatrix} \dot{\gamma}_1 & \dot{\gamma}_2 \end{pmatrix} \mathbf{C} \begin{pmatrix} \dot{\gamma}_1 \\ \dot{\gamma}_2 \end{pmatrix} \tag{2.60}$$

The classical Hamiltonian of the three-junction flux qubit can be found by applying the Legendre transformation to the Lagrangian of the system. The Hamiltonian of the system can be quantized similarly to the Josephson junction Hamiltonian quantization described in the previous sections. The conjugate coordinates are replaced by the quantum operators. The finite barrier between the wells allows a quantum tunneling process which lifts the degeneracy in potential well states. This hybridization process creates the energy levels for the persistent current qubit. The first few numerically calculated energy levels are shown in Fig 2.15 for a typical flux qubit.

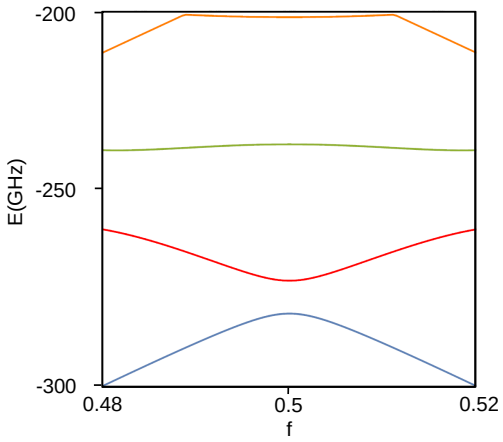

Figure 2.15: The first four energy levels of a typical persistent current qubit with external flux f and $E_J/E_C = 42$.

Two-level model

In Fig. 2.15, it can be seen that the anharmonicity is large around $f = 0.5$. Therefore, the first two levels of the quantum system can be used to approximate the system dynamics as a qubit. The Hamiltonian of the two-level flux qubit can be expressed using the minimum energy separation between the ground and excited state Δ, the asymmetry parameter ϵ, and Pauli matrices as

$$H_{2S} = -\frac{1}{2}\Delta\sigma_x - \frac{1}{2}\epsilon\sigma_z. \tag{2.61}$$

The Hamiltonian H_{2S} can be diagonalized by a unitary rotation with an angle $\tan\Theta = \Delta/\epsilon$.

$$U = e^{-i\Theta\sigma_y} = \begin{pmatrix} \cos\frac{\Theta}{2} & -\sin\frac{\Theta}{2} \\ \sin\frac{\Theta}{2} & \cos\frac{\Theta}{2} \end{pmatrix} \tag{2.62}$$

and it can be expressed as

$$H_{qb} = -\frac{\sqrt{\epsilon^2+\Delta^2}}{2}\sigma_z = -\frac{\hbar\omega_{qb}}{2}\sigma_z. \tag{2.63}$$

The qubit ground and excites states ($|g\rangle$ and $|e\rangle$) are then expressed as

$$|g\rangle = \cos\frac{\Theta}{2}|l\rangle + \sin\frac{\Theta}{2}|r\rangle \tag{2.64}$$

$$|e\rangle = \cos\frac{\Theta}{2}|l\rangle - \sin\frac{\Theta}{2}|r\rangle. \tag{2.65}$$

in relation to persistent current states ($|l\rangle$ and $|r\rangle$). At the symmetry point, $\Theta = \pi/2$ and both qubit states are superpositions of clockwise and counterclockwise persistent current states $|l\rangle$ and $|e\rangle$ with equal probability amplitudes. The net average current flowing in the ring for this case is zero.

2.4 Qubit state control

The state of any two-level system can be expressed as a vector in a unit sphere known as the Bloch sphere. With the help of Fig. 2.16, an arbitrary qubit state $|\psi\rangle = \alpha|0\rangle + \beta|1\rangle$ is expressed as

$$|\psi\rangle = \big(\cos\frac{\theta}{2}|0\rangle + e^{i\varphi}\sin\frac{\theta}{2}|1\rangle\big). \tag{2.66}$$

The control of the qubit can be understood by rotations on the Bloch sphere. A way to control the phase ϕ of the qubit is to wait for its free precession of the state at a rate of $\sqrt{\Delta^2+\epsilon^2}/\hbar$.

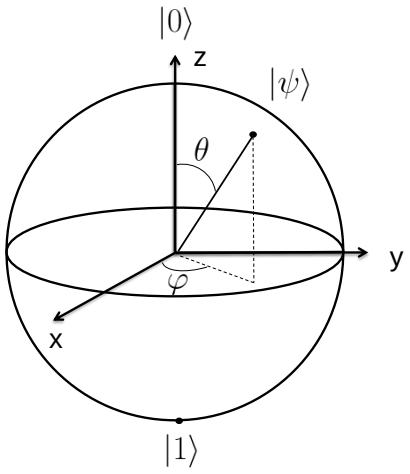

Figure 2.16: The Bloch sphere. An arbitrary qubit state $|\psi\rangle = \cos(\theta)|0\rangle + e^{i\varphi}\sin(\theta)|1\rangle$ is represented on the Bloch sphere.

An external microwave signal is used to implement a rotation which includes control of the angle θ. The signal imposes oscillating magnetic field to the loop and perturbs the asymmetry of the double well potential. Therefore, it can be regarded as an operator proportional to σ_z operator. An external drive Hamiltonian is typically in the form of

$$H_d = A\cos(\omega_d t + \phi)\sigma_z, \tag{2.67}$$

where A is the driving amplitude and ϕ is the drive phase. The driving Hamiltonian can be rotated into the qubit eigenbasis using Eq. 2.62.

$$H'_d = A\cos(\omega_d t + \phi)\Big(\frac{\Delta}{\hbar\omega_{qb}}\sigma_x - \frac{\epsilon}{\hbar\omega_{qb}}\sigma_z\Big). \tag{2.68}$$

The total Hamiltonian ($H = H_{qb} + H_d\prime$) of the system can be simplified by a unitary transformation $U = \exp(i\omega_d t\sigma_z/2)$ which transforms into a frame rotating with the drive.

The total Hamiltonian in the rotating frame is

$$\begin{aligned} H_{RF} &= -\frac{1}{2}(\omega_{qb}-\omega_d)\sigma_z + A\frac{\epsilon}{\omega_{qb}}\cos(\omega_d t+\phi)\sigma_z \\ &+\frac{A}{2}\frac{\Delta}{\omega_{qb}}\big(\cos(2\omega_d t+\phi)\sigma_x - \sin(2\omega_d t+\phi)\sigma_y\big) \\ &+\frac{A}{2}\frac{\Delta}{\omega_{qb}}\big(\cos(\phi)\sigma_x + \sin(\phi)\sigma_y\big) \end{aligned} \tag{2.69}$$

When the driving amplitude is weak compared to the drive frequency, the fast oscillating terms with ω_d and $2\omega_d$ average out during slow time scales of the qubit dynamics. This assumption is called rotating wave approximation (RWA) and this simplifies the Eq. 2.70 into

$$H^{\text{RWA}} = -\frac{1}{2}(\omega_{qb}-\omega_d)\sigma_z + \frac{A}{2}\frac{\Delta}{\omega_{qb}}[\cos(\phi)\sigma_x + \sin(\phi)\sigma_y]. \tag{2.70}$$

When $\omega_d = \omega_{qb}$, the Hamiltonian corresponds to an operator which rotates the qubit around x or y axis depending on the ϕ with a Rabi frequency $\Omega_R = A\Delta/(2\omega_{qb})$. When drive is off-resonant ($\omega_d \neq \omega_{qb}$), the rotation frequency is $\Omega = \sqrt{\Omega_R^2 + (\omega_{qb}-\omega_d)^2}$.

2.5 Circuit quantum electrodynamics

Cavity quantum electrodynamics (QED) investigates the interaction of matter with light confined in a cavity. The cavity imposes discrete modes for the light which can interact with a trapped atom. The properties of the coupled system can be studied by the Hamiltonian known as Jaynes-Cummings Hamiltonian [41]. The Jaynes-Cummings Hamiltonian depicts the atom (qubit) as a two-level system and the cavity as a mode of the electric field. Circuit QED (cQED) is analogous to cavity-QED. In cQED, a microwave resonator replaces the cavity and hosts qubits acting as artificial atoms. cQED is quite useful to describe the superconducting flux qubit coupled to a CPW resonator. Equation 2.71 describes the JC

Hamiltonian of a qubit in a resonator

$$H_{\mathrm{JC}} = H_{\mathrm{r}} + H_{\mathrm{qb}} + H_{\mathrm{int}}, \tag{2.71}$$

where H_r is the Hamiltonian describing the CPW resonator, H_{qb} is the qubit Hamiltonian and H_{int} is Hamiltonian describing the interaction representing a dipole coupling between the qubit and the electromagnetic field in its vicinity. The individual Hamiltonians are

$$H_{\mathrm{r}} = \hbar\omega_r(a^\dagger a + \frac{1}{2}) \tag{2.72}$$

$$H_{\mathrm{qb}} = \frac{1}{2}\hbar\omega_{qb}\sigma_z \tag{2.73}$$

$$H_{\mathrm{int}} = \hbar g(a\sigma_+ - a\sigma_- - a^\dagger\sigma_+ + a^\dagger\sigma_-), \tag{2.74}$$

where σ_+ and σ_- are qubit raising and lowering operators given by $\frac{1}{2}(\sigma_x \pm i\sigma_y)$ and g is the coupling strength between the qubit and resonator. The interaction part contains terms which do not conserve energy since it both adds or removes energy to the resonator and the qubit at the same time. Invoking the rotating wave approximation and ignoring the energy non-conserving terms ($a^\dagger\sigma_+$, $a\sigma_-$), the Hamiltonian can be written as

$$H_{\mathrm{JC}} = \frac{1}{2}\hbar\omega_{qb}\sigma_z + \hbar\omega_r(a^\dagger a + \frac{1}{2}) + \hbar g(a\sigma_+ + a^\dagger\sigma_-). \tag{2.75}$$

The interaction term now only allows for a quanta of energy exchange between the resonator states and the qubit states. Figure 2.17 depicts the energy spectrum of the coupled system with changing qubit frequency ω_{qb}. On resonance ($\omega_{qb} = \omega_r$), the degeneracy is lifted by the coupling term g and the energies differ by $2g$. In this case eigenstates are the superpositions of qubit and resonator states. The energy is swapped back and forth between the resonator and the qubit at a rate $2g$. This phenomenon is known as vacuum Rabi oscillations. When far detuned ($|\omega_{qb} - \omega_r| \gg g$), the eigenstates of the JC Hamiltonian approximates to the case where qubit and resonator are decoupled.

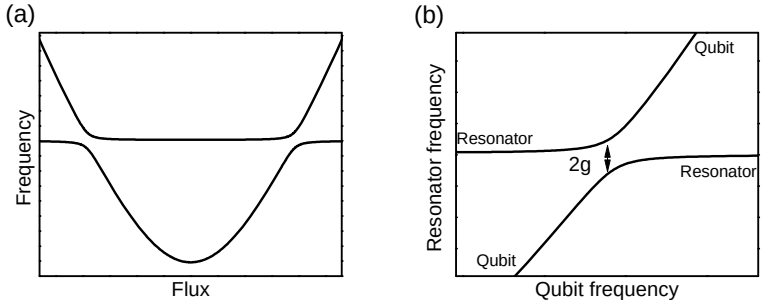

Figure 2.17: Energy level structure of the coupled resonator qubit system. a) The lowest two eigenstates of the Jaynes-Cummings Hamiltonian for a typical qubit and resonator parameters. b) The interaction term creating a splitting(2g) in the energy levels when the qubit and the resonator are in resonance. Away from this point, the eigenstates are well approximated by uncoupled qubit and resonator system.

2.5.1 Dispersive regime

The dispersive regime describes far detuning of the qubit and resonator ($\Delta\omega = |\omega_{qb} - \omega_r| \gg g$). The interaction in this regime is negligible and no energy exchange between the qubit and the cavity occurs. In the interaction picture, since the qubit Hamiltonian and interaction Hamiltonian commute with σ_z, the Hamiltonian can be expressed as

$$H_D = \frac{1}{2}\hbar(\omega_{qb} + \frac{g^2}{\Delta\omega})\sigma_z + \hbar\big(\omega_r + \frac{g^2}{\Delta\omega}\sigma_z\big)(a^\dagger a + \frac{1}{2}). \tag{2.76}$$

Here it can be concluded that the interaction does not alter the qubit Hamiltonian but imposes a shift on the resonance frequency of the CPW resonator. Thus by measuring the transmission spectrum of the resonator, the qubit state can be determined. The difference in the resonance frequency corresponding to qubit states $|0\rangle$ and $|1\rangle$ is 2χ with $\chi = \frac{g^2}{\Delta\omega}$.

2.6 Decoherence

The coherence time of a quantum system is an important metric in quantum computation. It describes the characteristic life-time of a stored information on the quantum system. The

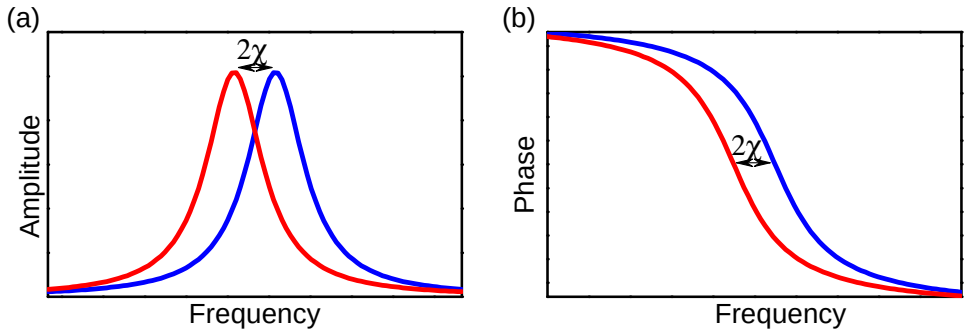

Figure 2.18: Resonator transmission spectrum with qubit states. The shift on the resonance frequency of the resonator due to the qubit state can be observed on the a) amplitude and b) on the phase of resonance. The red and blue lines correspond to the transmission due to the qubit states $|0\rangle$ and $|1\rangle$.

number of operations on the system depends on the gate duration and coherence time. In the quantum picture, a qubit system tend to lose its coherence due to environment its coupled to. In order to realize a useful quantum system, the qubit coherence times need to be long enough for successful quantum operations. Therefore, the characteristics life times of a quantum system is a crucial metric.

There are two different processes which leads to loss of coherence. First, the quantum system can emit its energy to the surrounding resonant systems and undergo a relaxation process into another state. If the system is in contact with an environment at finite temperature, the thermal energy can induce excitations in the system. These processes cause the system to lose its coherence due to the energy exchange. The characteristic decay time for this decoherence process is known as T_1. Second, due to the fluctuations in the environmental parameters effecting the system Hamiltonian, the system frequencies fluctuate leading to random evolution of the phase.

In the following subsection, the decoherence is analyzed in more details with master equation formalism. The expressions for the energy relaxation and dephasing processes are derived.

2.6.1 Master equation

Any qubit state can be represented by a vector on a Bloch sphere. A useful description of a quantum system is the density matrix formalism. It can be constructed by

$$\rho = \sum_n p_n |\psi_n\rangle\langle\psi_n|. \tag{2.77}$$

The evolution of the system in Schrödinger picture is expressed as,

$$i\hbar\dot{\rho} = [H, \rho] \tag{2.78}$$

Schrödinger's equations describes well the evolution of a closed quantum systems. Decoherence process can be analyzed by assuming the qubit is interacting with an environment and undergoing relaxation and dephasing processes. The environment can be treated as a quantum system and the whole system of qubit, environment, and the interaction forms a closed system and can be treated with Schrödinger equation for its evolution. The Hamiltonian of this joined system is given by

$$\begin{aligned} H &= H_{\mathrm{S}} + H_{\mathrm{SB}} + H_{\mathrm{B}}, & (2.79)\\ H_{\mathrm{S}} &= \hbar \sum_i \omega_i |i\rangle\langle i|, & (2.80)\\ H_{\mathrm{SB}} &= Af, & (2.81) \end{aligned}$$

where H_{S}, H_{B}, and H_{SB} are the system, environment, and the interaction Hamiltonians respectively. The interaction Hamiltonian is built by the qubit operator A and the environment operator f. In the interaction picture with respect to system and environment Hamiltonian(H_{S}+H_{B}), the Schrödinger equation becomes $i\hbar\dot{\tilde{\rho}} = [\tilde{H}, \tilde{\rho}]$. The evolution of the $\tilde{\rho}$ is given as [42],

$$\dot{\tilde{\rho}}(t) = -\frac{i}{\hbar}[\tilde{H}(t), \tilde{\rho}(t)] - \frac{1}{\hbar^2}\int_0^t [\tilde{H}(t), [\tilde{H}(t'), \tilde{\rho}(t')]]dt'. \tag{2.82}$$

Here two approximations can be applied to further simplify the Eq.2.82. First, we assume that the interaction between the environment and the system is weak compared to the system and the environment. This approximation is known as Born approximation. Additionally, the environment is assumed to be a large system in which the interaction does not affect the environment. This allows to express the density matrix as $\tilde{\rho}(t) = \tilde{\rho}_S \otimes \tilde{\rho}_B$. Second, it is assumed that the system density matrix operator $\tilde{\rho}(t)$ is independent of $\tilde{\rho}(t')$. This approximation is known as Markov approximation. With these approximations the Born-Markov master equation is given by [42]

$$\dot{\rho}(t) = \frac{1}{2\hbar^2} \sum_{j,k} |A_{jk}|^2 S(\omega_{jk})[2|k\rangle\langle j|\rho(t)|j\rangle\langle k| - \rho(t)|j\rangle\langle j|) - |j\rangle\langle j|\rho(t)] \tag{2.83}$$

where $\omega_{jk} = \omega_j - \omega_k$, and $S(\omega) = \int_{-\infty}^{\infty} e^{i\omega\tau}\langle \tilde{f}(\tau)\tilde{f}(0)\rangle$ is the power spectral density of the environment operator. Here, j, k represent the states of the system H_S.

Relaxation and dephasing

In the relaxation process, the quantum system moves from one state to another. For the two-level qubit case, where $j, k = 0, 1$, Eq.2.83 becomes

$$\begin{aligned}\dot{\rho}(t) = \Gamma_{10}[\hat{\sigma}_-\rho(t)\hat{\sigma}_+ - \frac{1}{2}\hat{\sigma}_+\hat{\sigma}_-\rho(t) - \frac{1}{2}\rho(t)\hat{\sigma}_+\hat{\sigma}_-] \\ +\Gamma_{01}[\hat{\sigma}_+\rho(t)\hat{\sigma}_- - \frac{1}{2}\hat{\sigma}_-\hat{\sigma}_+\rho(t) - \frac{1}{2}\rho(t)\hat{\sigma}_-\hat{\sigma}_+]\end{aligned} \tag{2.84}$$

while $j \neq k$. Equation 2.84 can be expressed by superoperators with $\mathcal{L}[\hat{\sigma}]\rho(t) = \hat{\sigma}\rho(t)\hat{\sigma}^\dagger - \frac{1}{2}\hat{\sigma}^\dagger\hat{\sigma}\rho(t) - \frac{1}{2}\rho(t)\sigma^\dagger\sigma$ as:

$$\dot{\rho(t)} = \Gamma_{10}\mathcal{L}[\hat{\sigma}_-]\rho(t) + \Gamma_{01}\mathcal{L}[\hat{\sigma}_+]\rho(t). \tag{2.85}$$

The transition rates Γ_{01} and Γ_{10} (transition from $|0\rangle$ to $|1\rangle$ and $|1\rangle$ to $|0\rangle$, respectively) are given as:

$$\Gamma_{10} = \frac{1}{\hbar^2}|A_{10}|^2 S(\omega_{10}) \tag{2.86}$$

$$\Gamma_{01} = \frac{1}{\hbar^2}|A_{10}|^2 S(\omega_{01}). \tag{2.87}$$

$$\tag{2.88}$$

For the case of $j = k$, we find the Eq.2.83 for the dephasing process. Again for the qubit case, the evolution of the density matrix operator is given as

$$\dot{\rho}(t) = \Gamma_{\varphi}\mathcal{L}[\hat{\sigma}_z]\rho(t), \tag{2.89}$$

and the qubit dephases with a rate

$$\Gamma_{\varphi} = \frac{1}{2\hbar^2}(|A_{11}|^2 - |A_{00}|^2)S(0) \tag{2.90}$$

2.6.2 Dephasing with $1/|\omega|$ flux noise

Low frequency noise is the most common noise observed superconducting flux qubits. The power spectral density of the low frequency noise is in the form of

$$S_{\xi}(w) = \frac{A}{|\omega|^{\alpha}} \tag{2.91}$$

where α is a positive number and A is a constant. Assuming a classical noise, the qubit Hamiltonian with the noise is given by

$$H_{qb} = -\hbar\frac{\omega_{\mathrm{qb}} + \xi(t)}{2}\sigma_z, \tag{2.92}$$

where $\xi(t)$ is the stochastic process describing the noise. The superposition of states acquires additional phase due to the presence of the random noise term as $\Delta\varphi(\tau) =$

$-\int_0^\tau \xi(t)dt$. For a Gaussian noise with zero average, the average of the term $\exp(i\Delta\varphi(\tau))$, describing the decay of the coherence of the density matrix, is given by

$$\langle e^{-i\int_0^\tau dt\xi(t)}\rangle = e^{-\frac{1}{2}\int_0^\tau dt_1\int_0^\tau dt_2\langle\xi(t_1)\xi(t_2)\rangle}. \tag{2.93}$$

The correlation function $\langle\xi(t_1)\xi(t_2)\rangle$ is expressed in terms of power spectral density $S_\xi(\omega)$ with Fourier transformations as

$$\langle\xi(t_1)\xi(t_2)\rangle = \frac{1}{2\pi}\int_{-\infty}^{\infty} d\omega e^{-i\omega\tau}S_\xi(\omega). \tag{2.94}$$

Equation 2.93 becomes

$$\langle e^{-i\int_0^\tau dt\xi(t)}\rangle = e^{-\frac{\tau^2}{2}\frac{1}{2}\int d\omega S_\xi(\omega)\mathrm{sinc}^2(\frac{\omega\tau}{2})} \tag{2.95}$$

Following Ithier *et al.* [43], with the noise with power spectral density in the form of $1/|\omega|$ with low-frequency ω_{ir} and high-frequency cut-offs for the power spectral density, the decay function is expressed as

$$\langle e^{-i\int_0^\tau dt\xi(t)}\rangle = \exp\big[-t^2A(\ln\frac{1}{\omega_{\mathrm{ir}}t}) + O(1)\big] \tag{2.96}$$

The coherence function has a Gaussian decay characteristics for $1/|\omega|$ noise.

2.6.3 Noise sources in superconducting qubits

Charge noise is the most commonly observed noise in solid state devices. Trapped charges or impurities in the vicinity of the qubit can induce charge fluctuations in the junction islands. Charge noise follows a $1/\omega$ power spectral density [44] and induces significant decoherence for superconducting devices that are in charge regime $E_{\mathrm{J}} < E_{\mathrm{C}}$. The source for the charge noise is typically the two-level systems(TLS), in which the electron hops between available states affecting the electrical environment of the qubit. TLS can also

induce relaxation in qubits and resonators. The electric fields inside the resonator or the qubit can couple to TLS present around. The characteristic energy of the TLS are broad in frequency, therefore a resonant TLS can absorb energy from the qubit, inducing decoherence [45].

Magnetic flux noise can cause significant decoherence for the superconducting qubits having large E_{J}. The study of the source of the flux noise remains highly relevant topic. One source of the flux noise is the trapped fluxoids that can hop between trap sites [46]. In addition, TLS can also generate flux noise with $1/\omega$ power spectral density due to the magnetic moments of the hopping electron. Recently it has been suggested the unpaired surface spins gives $1/\omega$ flux noise [47].

Flux qubits are in the flux regime and the dependency of the transition frequency on charge fluctuations is low. Therefore, dephasing due to the charge noise is relatively negligible. On the other hand, the qubit frequency depends strongly on the flux. Flux fluctuations, especially away from the symmetry point induce decoherence with high rates. To mitigate this problem, flux qubits are operated at the symmetry point. The measured $\sqrt{A}$ for the power spectral density of A/ω^{α} is typically in the order of $1 \times 10^{-6}\Phi_0$ [48].

Chapter 3

Design and modeling of capacitively shunted flux qubits

Superconducting qubits are promising candidates for implementing scalable fault tolerant quantum computers. Over the years, superconducting qubits have showed significant improvements on their performances. Improved fabrication methods and designs lead to long-coherence quantum devices. One particular example is the evolution of the charge qubit. The charge qubit first exhibited coherence times of few nanoseconds [49]. Introducing shunt capacitors to qubit Josephson junctions resulted in several orders of magnitudes increase in the coherence times of the charge qubit; this design is known as transmon qubit [17].

Capacitive shunting of the qubit junction reduces the charging energy since the total capacitance across the junction increases. The $E_{\mathrm{J}}/E_{\mathrm{C}}$ ratio becomes larger and the sensitivity of the charge qubit to charge fluctuations is reduced, as seen in previous chapter. Compared to a typical Josephson junction, relatively large size of the shunting capacitors allows for a more reproducible fabrication as typically they are in several hundreds of micrometers range. This not only enhances the reproducibility but also allows one to control the participation of the materials in the vicinity of the electric fields. The capacitance

across the superconducting islands is dominated by the shunt capacitor. The confined electric field in the Josephson junction is distributed over the junction and the shunt capacitor. The effect of the less controllable lossy oxide barrier of Josephson junction is consequently reduced. This approach raised the coherence times of the charge qubit to the 10-100 μs range [17, 50]. However, the anharmonicity of the charge qubit energy levels is reduced.

The flux qubit distinguishes itself from the other Josephson junction based qubits by having a large anharmonicity in energy levels and flexible coupling mechanisms [51, 52]. The superconducting loop of the flux qubit is utilized to implement direct and tunable qubit-qubit coupling [53, 54, 55]. The flux qubit is also useful to probe the light matter interactions in the ultra-strong coupling regime where the coupling strength is comparable to the artificial atom and cavity frequency [56, 57]. The strong coupling between the qubit and a resonator is achieved by galvanically connecting the qubit to the resonator.

The flux qubit is in the $E_{\mathrm{J}}/E_{\mathrm{C}} \gg 1$ regime. It is insensitive to charge noise, however, the frequency of the qubit is sensitive to flux fluctuations especially when it is away from the flux-symmetry point. If it is in the charge regime, the charge fluctuations becomes important and can contribute significantly to the decoherence process. On the contrary, the sensitivity to flux noise is reduced. The sensitivity of the qubit to the charge noise can be improved by adding shunt capacitors and reducing the charging energy of the junction. The sensitivity to the flux fluctuations can be reduced by reducing the Josephson energy of the qubit by adjusting the junction critical currents.

In this chapter, first, we introduce the design and the model for the capacitively shunted three-junction flux qubit. Next, we discuss the electromagnetic(EM) simulations of the CPW resonators and the total capacitance matrix of the system. The qubit parameters are then simulated based on the introduced model with the results from EM simulations and nominal fabrication parameters. Last, we discuss the fabrication methods.

3.1 The shunted flux qubit

In this section, a modified version of a regular three-junction persistent current qubit [40] is considered. It consist of a superconducting loop containing three Josephson junctions. The modification is done by adding coplanar shunt capacitors across each junction. Figure 3.1 shows a cartoon sketch of the device. The junctions, illustrated as crosses, are placed in between the superconducting capacitor pads (islands) 1, 2, and 3. The superconducting

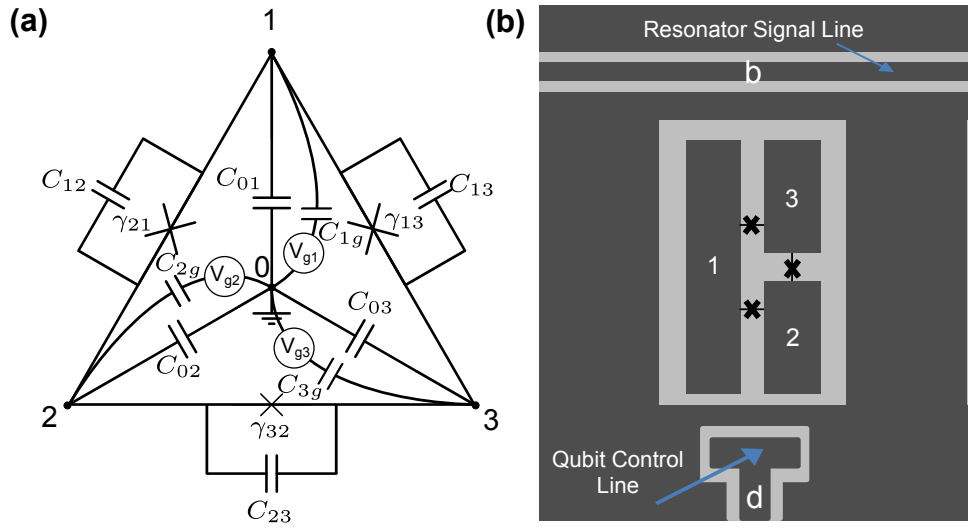

Figure 3.1: Design and circuit model of the capacitively shunted flux qubit.a) Circuit diagram of the design shown in (b). The node 0 corresponds to the CPW ground plane and the nodes 1,2 and 3 correspond to the capacitor pads. b) A sketch of the 3 junction flux qubit with the shunt capacitor pads labeled as 1, 2, and 3. The resonator electrode and the drive pad are labeled as b and d, respectively. Drak gray areas represent the superconductor metal layers where light gray is the substrate.

phase difference across the junctions are γ_{21}, γ_{32}, and γ_{13} respectively and γ_{01} is the associated branch flux between nodes 0 and 1. Applying the flux quantization condition, the phase on junction between node 2 and 3 can be rewritten as $\gamma_{32} = \gamma_{21} + \gamma_{13} + 2\pi f$, with external magnetic frustration f. The capacitors C_{12}, C_{23}, and C_{13} correspond to the total capacitance across the junctions consisting of the junction self capacitances and the shunt capacitor. In the circuit, the ground is represented by the node 0. The islands are coupled

to the CPW resonator ground planes through the capacitors C_{01}, C_{02}, and C_{03}. The gate electrodes can be explicit for biasing the circuit through the capacitors C_{1g}, C_{2g}, and C_{3g} with corresponding voltages V_{g1}, V_{g2}, and V_{g3}. The gate capacitors can also be used to model trapped charges.

The kinetic energy of the circuit consists of the electrostatic energy stored in the capacitors and it is dominated by the shunt capacitances. Following Orlando *et al.* [40] and ignoring the offset energies, the kinetic energy term is expressed as

$$T = \frac{\varphi_0^2}{2}\, \dot{\gamma}^T C' \dot{\gamma} + \varphi_0 \dot{\gamma}^T D Q_g \tag{3.1}$$

where φ_0 is reduced magnetic flux quantum and

$$\dot{\gamma} = \begin{pmatrix} \dot{\gamma}_{21} \\ \dot{\gamma}_{31} \\ \dot{\gamma}_{10} \end{pmatrix} \quad , \quad Q_g = \begin{pmatrix} C_{g1} V_{g1} \\ C_{g2} V_{g2} \\ C_{g3} V_{g3} \end{pmatrix}. \tag{3.2}$$

The capacitance matrix C' is

$$C' = \begin{pmatrix} C_{12} + C_{23} + C_{2g} + C_{02} & -C_{23} & C_{2g} + C_{02} \\ -C_{23} & C_{13} + C_{23} + C_{3g} + C_{03} & C_{3g} + C_{03} \\ C_{2g} + C_{02} & C_{3g} + C_{03} & \begin{matrix} C_{1g}+C_{2g}+C_{3g} \\ +C_{01}+C_{02}+C_{01} \end{matrix} \end{pmatrix}. \tag{3.3}$$

The above capacitance matrix C' is for the floating circuit case where coupling to the drive line and the to the resonator has not been included yet. The matrix D is given as

$$D = \begin{pmatrix} 0 & -1 & 0 \\ 0 & 0 & -1 \\ -1 & -1 & -1 \end{pmatrix}. \tag{3.4}$$

The potential energy of the system is due the Josephson junctions and it is expressed

as

$$U = -\varphi_0[I_{C_{12}}\cos(\gamma_{12}) + I_{C_{13}}\cos(\gamma_{13}) + I_{C_{23}}\cos(\gamma_{21}+\gamma_{13}+2\pi f)], \tag{3.5}$$

where $I_{C_{12}}$, $I_{C_{13}}$, and $I_{C_{23}}$ are the junction critical currents. The design consists of two identical junctions of same area and a third junction having a smaller area, rescaled by the factor α. Since all three junctions are fabricated at the same time, the critical currents $I_{C_{12}} = I_{C_{13}} = I_{C_{23}}/\alpha$.

We select the Lagrangian of the system as $\mathcal{L} = T - U$. The Euler-Lagrange equation is given by

$$\frac{d}{dt}\left(\frac{\partial \mathcal{L}}{\partial \dot{\gamma}}\right) = \frac{\partial \mathcal{L}}{\partial \gamma}. \tag{3.6}$$

For the node 2 and γ_{21}, Eq. 3.6 becomes

$$\begin{aligned}\varphi_0^2\big[C_{12}\ddot{\gamma}_{21} + C_{23}(\ddot{\gamma}_{21} - \ddot{\gamma}_{31}) + C_{2g}(\ddot{\gamma}_{21} - \ddot{\gamma}_{10}) + C_{02}(\ddot{\gamma}_{21} + \ddot{\gamma}_{10})\big] \\ = \varphi_0\big[-I_{C_{12}}\sin(\gamma_{21}) - I_{C_{23}}\sin(\gamma_{21}+\gamma_{13}+2\pi f)\big].\end{aligned} \tag{3.7}$$

The left hand side of the Eq. 3.7 represents the current leaving node 2 through capacitors and the right hand side represents the current entering the node through the Josephson junctions. Similar approach holds for node 3. For node 0 we have $\frac{d}{dt}\left(\frac{\partial \mathcal{L}}{\partial \dot{\gamma}_{10}}\right) = 0$. The equation of motions satisfies the Euler-Lagrange equation in Eq. 3.6. The Hamiltonian of the system is then obtained by the Legendre transformation and expressed as

$$H = \frac{1}{2}\left(\frac{p}{\varphi_0} - DQ_g\right)^T C'^{-1}\left(\frac{p}{\varphi_0} - DQ_g\right) + U(\gamma), \tag{3.8}$$

where the conjugate momentum vector $p = (p_{\gamma_{21}}, p_{\gamma_{31}}, p_{\gamma_{10}})$ is

$$p = \nabla_\gamma T = \varphi_0^2 C'\dot{\gamma} + \varphi_0 DQ_g. \tag{3.9}$$

The momentum vector is related to the total charges on the nodes. $p_{\gamma_{21}}/\varphi_0$ represents the total charges on the plates of the capacitors on the side of node 2 with $p_{\gamma_{21}}/\varphi_0 = 2e \times n_2$

where e is the electronic charge and n_2 is the number of cooper pairs on the island 2. Similarly, $p_{\gamma_{31}}/\varphi_0 = 2e \times n_3$ is the total charge on island 3. We note that $p_{\gamma_{10}}/\varphi_0$ is a constant of motion.

3.1.1 Coupling to a CPW resonator

In the following sections, we consider the cases where the capacitively shunted flux qubit is capacitively coupled to a CPW resonator for dispersive readout and a drive pad for quantum control. Figure 3.1(b) illustrates the qubit-resonator coupled system. The center conductor and the superconducting islands form capacitances denoted as $C_{1\mathrm{b}}$, $C_{2\mathrm{b}}$, and $C_{3\mathrm{b}}$. The total kinetic energy of the circuit needs to include these added capacitances. The CPW signal electrode is considered to be at voltage V_b and the kinetic energy in this case is then given by

$$T = \frac{\varphi_0^2}{2}\, \dot{\gamma}^T C'' \dot{\gamma} + \varphi_0 \dot{\gamma}^T D Q_g + \varphi_0 \dot{\gamma}^T D Q_b, \tag{3.10}$$

where

$$Q_b = C_b V_b = \begin{pmatrix} C_{1\mathrm{b}} \\ C_{2\mathrm{b}} \\ C_{3\mathrm{b}} \end{pmatrix} V_b. \tag{3.11}$$

The addition of this signal electrode modifies the capacitance matrix as $C'' = C' + C_{\mathrm{b}}^{+}$ and C_{b}^{+} is given by

$$C_{\mathrm{b}}^{+} = \begin{pmatrix} C_{2\mathrm{b}} & 0 & C_{2\mathrm{b}} \\ 0 & C_{3\mathrm{b}} & C_{3\mathrm{b}} \\ C_{2\mathrm{b}} & C_{3\mathrm{b}} & C_{1\mathrm{b}} + C_{2\mathrm{b}} + C_{3\mathrm{b}} \end{pmatrix}. \tag{3.12}$$

The kinetic energy term in the Hamiltonian is then expressed as

$$T_H = \frac{1}{2\varphi_0^2} \big(p - \varphi_0 D Q_g - \varphi_0 D Q_b\big)^T C''^{-1} \big(p - \varphi_0 D Q_g - \varphi_0 D Q_b\big). \tag{3.13}$$

In the Jaynes-Cummings treatment, the interaction between the coupled qubit and resonator is governed by the interaction Hamiltonian $H_{int} = g\sigma_x(a + a^\dagger)$. The interaction could be modeled by system Hamiltonian dependency on the control parameter. In this case, the interaction Hamiltonian can be expressed as

$$H_{\text{int}} = \frac{\partial T_H}{\partial V_b} V_b, \tag{3.14}$$

with

$$\begin{aligned} \frac{\partial T_H}{\partial V_b} &= \frac{1}{2\varphi_0^2} 2(-\varphi_0)(DQ_b)^T C''^{-1}(p - \varphi_0 DQ_g) \\ &\quad + \frac{1}{2} 2V_b (DQ_b)^T C''^{-1}(DQ_b) \end{aligned} \tag{3.15}$$

The degrees of freedom in momentum vector can be reduced since $p_{\gamma_{01}}$ is constant of motion and could be considered as an offset charge and simply added to other gate charges. The interaction term can be expressed in charge operators as

$$\frac{\partial T_H}{\partial V_b} = -2e \left(\left[(DC_b)^T C^{-1} \right]_1 (n_2 - n_{2\text{g}}) + \left[(DC_b)^T C^{-1} \right]_2 (n_3 - n_{3\text{g}}) \right), \tag{3.16}$$

where $\left[(DC_b)^T C^{-1} \right]_{1(2)}$ is the first(second) element of the product $(DC_b)^T C^{-1}$ and $n_{2\text{g}}$ and $n_{3\text{g}}$ are the gate charges.

The average energy of the resonator when it is in ground state $\langle E \rangle = \frac{\hbar\omega_r}{4} = \frac{1}{2}\tilde{c}lV_0^2$, where $\tilde{c}$ is the capacitance per unit length of the CPW resonator, l is the length of the resonator, and V_0 is the quantum zero point voltage of the resonator expressed as

$$V_0 = \sqrt{\frac{\hbar\omega_r}{2\tilde{c}l}}. \tag{3.17}$$

Expressing the off-diagonal part of $\partial T_H / \partial V_b$ in the form of $\alpha_b \times \sigma_x$(assuming no σ_y component) with the voltage on the signal electrode $V_b = V_0(a + a^\dagger)$, the coupling strength

between the resonator and the qubit is found as

$$g = \alpha_b \times \sqrt{\frac{\hbar\omega_r}{2\tilde{c}l}}. \tag{3.18}$$

3.1.2 Coupling to the drive line

The device design includes a capacitive drive line for qubit control. Figure 3.1 illustrates the drive line capacitively coupled to the shunted qubit. Similar to resonator signal line, the drive line electrode and the superconducting islands form capacitors denoted by $C_{1\mathrm{d}}$, $C_{2\mathrm{d}}$, and $C_{3\mathrm{d}}$. The total kinetic energy term is given by

$$T = \frac{\varphi_0^2}{2}\ \dot{\gamma}^T C\dot{\gamma} + \varphi_0\dot{\gamma}^T DQ_g + \varphi_0\dot{\gamma}^T DQ_b + \varphi_0\dot{\gamma}^T DQ_d. \tag{3.19}$$

The charges in the capacitors associated with the drive electrode are given by

$$Q_d = C_d V_d = \begin{pmatrix} C_{1d} \\ C_{2d} \\ C_{3d} \end{pmatrix} V_d. \tag{3.20}$$

The addition of the drive line modifies the capacitance matrix by $C = C'' + C_{\mathrm{d}}^+$ and C_{d}^+ is given by

$$C_{\mathrm{d}}^+ = \begin{pmatrix} C_{2d} & 0 & C_{2d} \\ 0 & C_{3d} & C_{3d} \\ C_{2d} & C_{3d} & C_{1d} + C_{2d} + C_{3d} \end{pmatrix}. \tag{3.21}$$

In order to consider the effect of the driving, we assume the time dependent drive to be in the form of $V_d(t) = V_{d0}\cos(\omega_d t + \varphi_d)$ where V_{d0} is the drive amplitude, ω_d is the drive frequency, and φ_d is the phase of the drive signal. The drive Hamiltonian then can be expressed as

$$H_d(t) = \frac{\partial T_H}{\partial V_d} V_{d0}\cos(\omega_d t + \varphi_d). \tag{3.22}$$

The system Hamiltonian sensitivity on the drive voltage is given as

$$\frac{\partial T_H}{\partial V_d} = -2e\,\left(\left[(DC_d)^T C^{-1}\right]_1 (n_2 - n_{2g}) + \left[(DC_d)^T C^{-1}\right]_2 (n_3 - n_{3g})\right). \tag{3.23}$$

For a two level system case, Eq. 3.23 can be represented in the qubit subspace as.

$$\frac{\partial T_H}{\partial V_d} = \begin{pmatrix} \langle 0|\frac{\partial T_H}{\partial V_d}|0\rangle & \langle 0|\frac{\partial T_H}{\partial V_d}|1\rangle \\ \langle 1|\frac{\partial T_H}{\partial V_d}|0\rangle & \langle 1|\frac{\partial T_H}{\partial V_d}|1\rangle \end{pmatrix} \tag{3.24}$$

where $|0\rangle$ and $|1\rangle$ are the ground and excited states of the qubit. The off-diagonal terms in the Eq. 3.24 describe the transition strengths between qubit states. Equation 3.24 can be expressed more generally with Pauli matrices as

$$\begin{aligned} \frac{\partial T_H}{\partial V_d} &= g_{01}\cos(\varphi_{01})\sigma_x + g_{01}\sin(\varphi_{01})\sigma_y \\ &= g_{01}\sigma_{\varphi_{01}}, \end{aligned} \tag{3.25}$$

where g_{01} is the transition strength between states 0 and 1. The drive Hamiltonian in Eq. 3.22 is then expressed as

$$H_d(t) = g_{01}V_{d0}\cos(\omega_d t + \varphi_d)\sigma_{\varphi_{01}}. \tag{3.26}$$

This drive Hamiltonian describes rotations on the Bloch sphere. The rotation axis is determined by the phase of the drive φ_d. The rotations are easier to illustrate in a rotating frame resonant with the drive. The details of the qubit drive is given in the previous chapter. For the drive in Eq. 3.26, the Rabi oscillation frequency is given by

$$\Omega_{R_{01}} = V_{d0}\alpha_{01}. \tag{3.27}$$

3.2 Device simulations

Device simulations play important role in determining the final device design and fabrication procedures. In this section we discuss several numerical simulations performed to confirm device characteristics. First, the electromagnetic response of the CPW resonator is discussed. Second, the qubit circuit capacitors including shunt pads are simulated to construct the system capacitance matrix. Third, qubit characteristics such as energy level structures and transition strengths are simulated based on the capacitance matrix and resonator simulations.

EM simulations

The capacitively shunted flux qubit is coupled to a half-wavelength resonator defined by interrupting a co-planar transmission line by coupling capacitors at both ends. The microwave response of the coupled resonator qubit system is simulated with Sonnet EM Suite and ANSYS HFSS software tools. In the simulations, the transmission spectrum and the current distribution in the resonator are simulated with frequency sweeps. The resonance frequency and the resonance modes are checked against any unwanted resonances and the geometry is adjusted to remove these spurious modes.

The CPW resonator is coupled to external circuitry for qubit state readout and the external coupling strength is found by assuming the internal loss of the resonator to be negligible ($Q_0 \to \infty$) and simulating transmission spectrum. In this case, the loaded quality factor Q_L will be limited by the external coupling as $\frac{1}{Q_L} = \frac{1}{Q_0} + \frac{1}{Q_{\text{ext}}} \approx \frac{1}{Q_{\text{ext}}}$. Alternatively, coupling capacitors of the CPW half-wavelength resonator can be simulated in EM tools and the external quality factor can be calculated numerically.

With EM simulations, the resonance frequency of the CPW is designed to be at 6.7 GHz with $Q_{\text{ext}} = 2 \times 10^5$. The resonator width/gap ratio is 16 μm/ 8.4 μm, leading to a characteristic impedance of $50\,\Omega$. The inductance and capacitance per unit length are 4.232×10^{-8} H/m and 1.708×10^{-10} F/m.

The capacitance simulations

The capacitance structure of the device is shown in Fig. 3.1. The capacitance matrix used in the model (Eq. 3.3) is constructed from the capacitance simulations performed in Sonnet EM Suite, ANSYS Q3D Extractor, and COMSOL Multi-physics softwares to compare simulation accuracy. The extracted capacitance values agree well in all simulations tools. The size of the pads and the gap dimensions between the pads and the ground plane are parametrized for optimizations. A set of parameters that are used in the device fabrication are given in Table 3.1.

Table 3.1: Set of parameters used in the capacitance simulations for the device geometry shown in Fig. 3.1.

Parameter	Value
Size of capacitor pad 1	100 μm × 300 μm
Size of capacitor pad 2	100 μm × 146 μm
Size of capacitor pad 3	100 μm × 146 μm
Gap between capacitor pads	8 μm
Gap between CPW ground plane and capacitor pads	10 μm
Distance between the drive line and capacitor pads	135 μm
Distance between the resonator and the capacitor pads	26.4 μm

In order to eliminate the loss associated with the amorphous junction oxide layers, the electric field across the qubit junctions are dispersed on these large shunt capacitors. The value shunt capacitances are designed to be at least factor of five higher than the junction self capacitances assuming the capacitance density of the Josephson junctions are approximately 80 fF/μm^2. Table 3.2 summarizes the simulated capacitance values with the geometry defined in Table 3.1.

Table 3.2: The simulated capacitances of the geometry defined in Table 3.1.

Capacitor	Value	Capacitor	Value
C_{13}	14.52 fF	C_{21}	14.74 fF
C_{32}	8.51 fF	C_{01}	62.9 fF
C_{02}	30.4 fF	C_{03}	32.9 fF
C_{1b}	2.60 fF	C_{2b}	2.61 fF
C_{3b}	0.21 fF	C_{1d}	0.15 fF
C_{2d}	0.02 fF	C_{3d}	0.11 fF

Qubit simulations

In this section, we present the circuit properties numerically calculated by the model presented in previous sections. In the simulations, the full circuit capacitance matrix, CPW resonator properties such as capacitance per unit length and resonance frequency, and junction critical currents are used as input parameters. The simulated capacitances corresponding to faricated device geometry are listed in Table 3.2. The model predicts the energy level structure with various flux frustration and gate charges as well as the sensitivities to flux and charge fluctuations. The model also predicts the coupling strengths of the qubit to the resonator and the drive line. The simulations are performed with the junction critical current density of 3.96 $\mu A/\mu m^2$. The area of the qubit reference junctions are 0.043 μm^2. The simulated energy level spectrum of the shunted circuit for the first five levels versus external magnetic flux ϕ is shown on Fig. 3.2. At flux-symmetry point($\Phi = 0.5\,\Phi_0$), the minimum energy splitting for the qubit space, formed by the lowest two energy levels, is $\omega_{01} = \Delta = 2\pi \times 1.708$ GHz. Away from the symmetry point, the transition frequency between the states 0 and 1 is well approximated by the two level model in Eq. 2.63. At the symmetry point, the higher level transitions are $\omega_{12} = 2\pi \times 5.4$ GHz, $\omega_{23} = 2\pi \times 5.553$ GHz, and $\omega_{34} = 2\pi \times 4.8$ GHz. The anharmonicity between 0-1 and 1-2 transition is $\omega_{12} - \omega_{01} = 2\pi \times 3.69$ GHz. The simulated energy spectrum is compared to the experiments in the next chapter.

The coupling strength between the qubit and the CPW resonator is calculated to be

$2\pi \times 8$ MHz. At symmetry point, the transition strengths are 1.45×10^{12} Hz/V, 3.75×10^{12} Hz/V, and 3.3×10^{-2} Hz/V for 0-1, 1-2, and 0-2 transitions respectively. Due to the symmetry of the potential energy at this flux point, the 0-2 transition is forbidden [58]. Away from the symmetry point, the double well potential structure becomes asymmetric and all three transition are allowed. The transition strengths at 0.501 mΦ_0 are 1.45×10^{12} Hz/V, 3.71×10^{12} Hz/V, and 5.22×10^{11} Hz/V respectively.

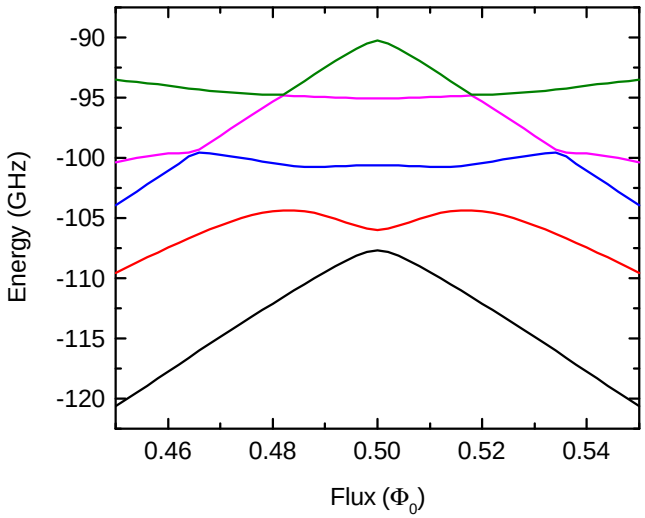

Figure 3.2: Numerically simulated first five levels of the capacitively shunted flux qubit.

Similar to the transmon qubits, the capacitively shunted flux qubit also shows negligible sensitivity to the gate charges. Figure 3.3 shows the energy level dependency on the gate charges n_{g2} and n_{g3} for 0-1, 1-2, and 0-2 transitions respectively. The maximum difference in the transition frequencies is $2\pi \times 133$, $2\pi \times 626$, and $2\pi \times 493$ Hz respectively.

3.3 Fabrication of capacitively shunted flux qubits

In this section, the fabrication procedures of the capacitively shunted flux qubits are discussed. This section is categorized into three parts. In the first part, the fabrication of the

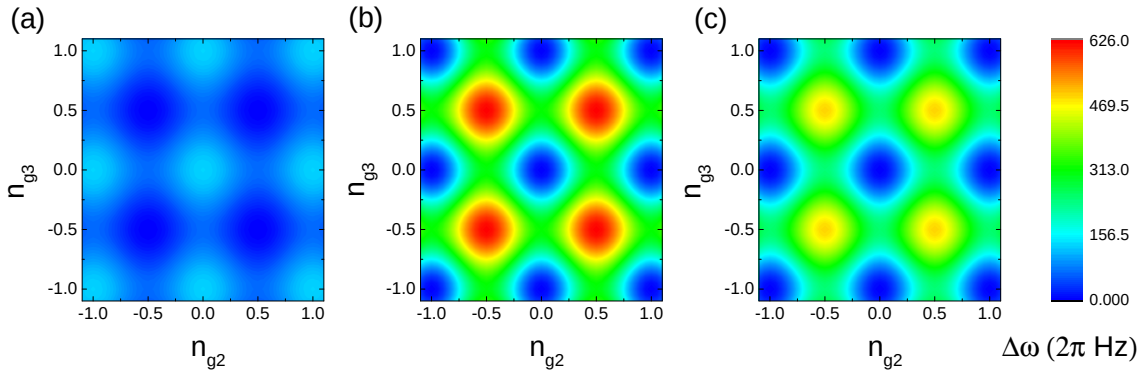

Figure 3.3: Gate charge dependency of the transition frequencies a) 0-1, b) 1-2, and c) 0-2 transition. The maximum frequency differences $\Delta\omega$ are 133, 626, and 493 Hz respectively.

marker layer is discussed. In the second part, the fabrication of the circuit layer, consisting of CPW resonator and qubit shunt capacitors, is discussed. In the last part, the details of the qubit junction fabrication are given.

3.3.1 The marker layer

The fabrication starts with chemical cleaning of high resistivity(10 kΩ.cm) 4" Si wafers. Si is one of the low loss materials for cQED applications [59] and it has been reported to yield high quality devices [60]. Figure 3.4 depicts the fabrication process for the circuit layer. The wafer is cleaned in ultrasonic bath of Acetone and isopropyl alcohol(IPA). The substrate is then rinsed with de-ionized water and vacuum baked for dehydration. For better resist adhesion, the substrate is coated with HMDS by vapor priming in 150 ^{0}C oven.

For alignment of the subsequent fabrication layers, we use the etched markers as reference points. The markers are fabricated by first applying a positive photo resist(Shipley s1811) on the substrate. After UV exposure and development in MF319, the exposed Si is etched with Bosch process to create vertical profile with 2 μm depth. These etched markers provide good contrast for optical lithography and especially for high energy e-beam

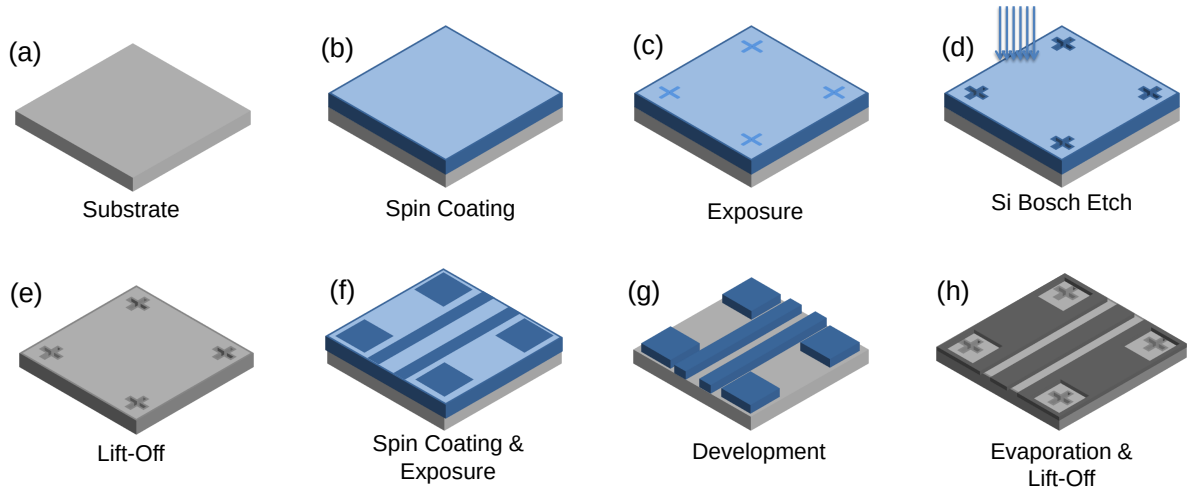

Figure 3.4: Sketch of the fabrication steps for (a)-(e) marker layer and (f)-(g) circuit layer.

imaging during the alignment step in the lithography. The substrate is then cleaned in an ultrasonic bath of remover PG at 80 °C followed by Acetone and IPA cleaning.

3.3.2 The circuit layer

The CPW resonator and the qubit shunt capacitor pads are fabricated in the same process. The substrate is coated with thin layer of HMDS for better resist adhesion. It is coated with 1.3 µm thick negative photoresist ma-N 1410. The photoresist is then exposed with Heidelberg MLA150 direct write lithography tool to pattern the circuit layer. After the exposure, the substrate is developed in ma-D 533/S developer for 90 secs. This results in a negative undercut profile for a better lift-off process. After the development of the ma-N 1410 resist, the substrate is treated with an oxygen descumming process. This is to remove any resist residues left on the surface of the Si. It is reported that, optical and e-beam lithography resists leave residues on the surface [60]. These residual layers can contribute to the loss directly or react with superconducting metal to form lossy regions. Next, the superconducting aluminum layer is evaporated in an e-beam evaporator

tool(Plassys MEB550S) to obtain 100nm of layer thickness with a rate of 0.3 nm/s. During the evaporation, the substrate is tilted to +5°,0°,-5° to create a tapered profile for better contact between the circuit layer and the subsequent layers. After evaporation, the lift-off process is carried out in a bath of Remover PG at 80°C. The bath is stirred to help the lift-off process. The substrate is further cleaned with Acetone and IPA baths

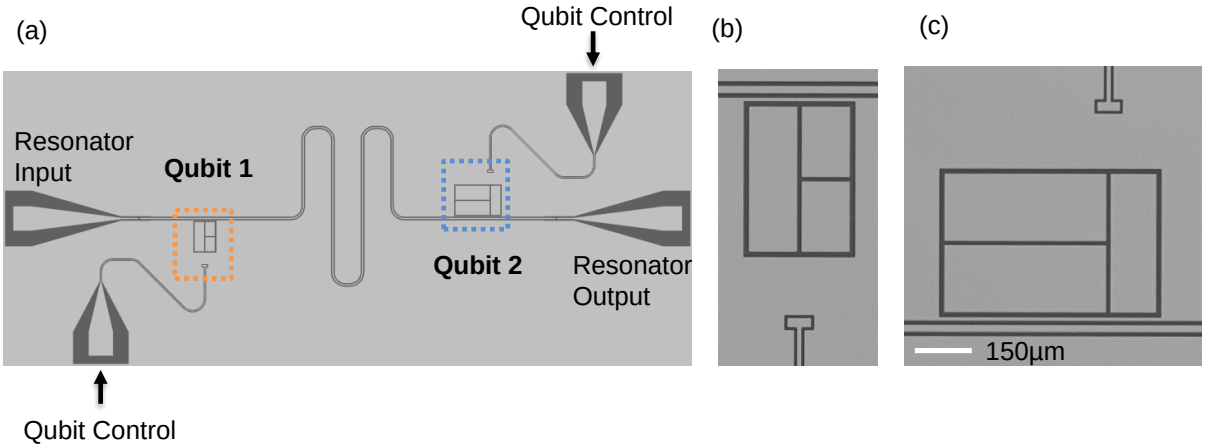

Figure 3.5: Images of the CPW resonator including shunt capacitors. a) The illustration of the 3mm x 7mm CPW resonator chip fabricated for the experiments. b) Microscope image of the qubit 1 shunt capacitors. c) Microscope image of qubit 2 shunt capacitors. The scale is 150 μm for (b) and (c).

Figure 3.5 shows the illustration of the fabricated CPW resonators and microscope images of the fabricated shunt capacitors for qubits. The half wavelength CPW resonator hosts up to two capacitively shunted flux qubit.

3.3.3 The qubit layer

The qubit is formed when the qubit junctions are placed in between the shunt capacitors. Fabrication of the qubit layer is depicted in Fig. 3.6. First, The chip is coated with polymethylglutarimide (PMGI) and polymethylmethacrylate (PMMA)electron beam resists for

a bi-layer lift-off process. PMGI SF7 is dispensed on the chip through a filter. It is spread at 2800 rpm/s for 90 seconds then baked at 200^{o}C for 20 minutes. Next, PMMA 950K A3 is dispensed on the chip through a filter and it is spin coated at 6000 rpm/s for 90 seconds. The chip is baked at 180^{o}C for 20 minutes. The resulting stack layer is around 520 nm.

The resist stack is exposed with high energy electron beam lithography tool(JEOL JBX-6300FS). Sub-micron features are written on the resist stack with 100 KeV acceleration voltage and with a beam current of 1 nA. The required dose for fine resolution structures are 1200 μC/cm^2. After the exposure, PMMA layer is developed in MIBK:IPA (1:3) solution for 70 seconds. Next, PMGI layer is developed in Microprosit developer concentrate for 40 seconds. This process creates an undercut profile of easier lift-off.

Before the evaporation step, the developed chip is again subjected to oxygen descumm process to remove any residual e-beam resist. The sample is transferred to the evaporation chamber. In order to remove the AlOx from the contact area of the capacitor pads, an argon milling process is done at angles 20° and -20°. This also helps to create a tapered profile for better contact between the capacitor pads and junction wires. Next, the evaporation angle is set to +20° and the first Al layer with thickness 40 nm is evaporated with a rate of 0.3 nm/s. After, the Al layer is oxidized (in-situ) in an oxygen environment of 0.012 mBar for 7 minutes. Changing the oxidation pressure and duration change the oxide thickness, therefore, the critical current of the final junction can be modified during this process. With typical oxidation parameters, it yields to junctions with critical current densities of $4 - 20\mu A/\mu m^2$. After oxidation step, second 65 nm of Al layer is evaporated at an angle of -20° with a rate of 0.3 nm/s. Finally, the chip is cleaned in Remover PG bath at 80°C for 40 minutes It is further cleaned by Acetone and IPA baths. This type of fabrication yields good junctions since both superconducting electrodes and the barrier material are fabricated in-situ and in a single process. After the cleaning step, the chip is diced into 3mm×7mm dies. Individual devices are then wire-bonded and placed in microwave packaging for low temperature measurements.

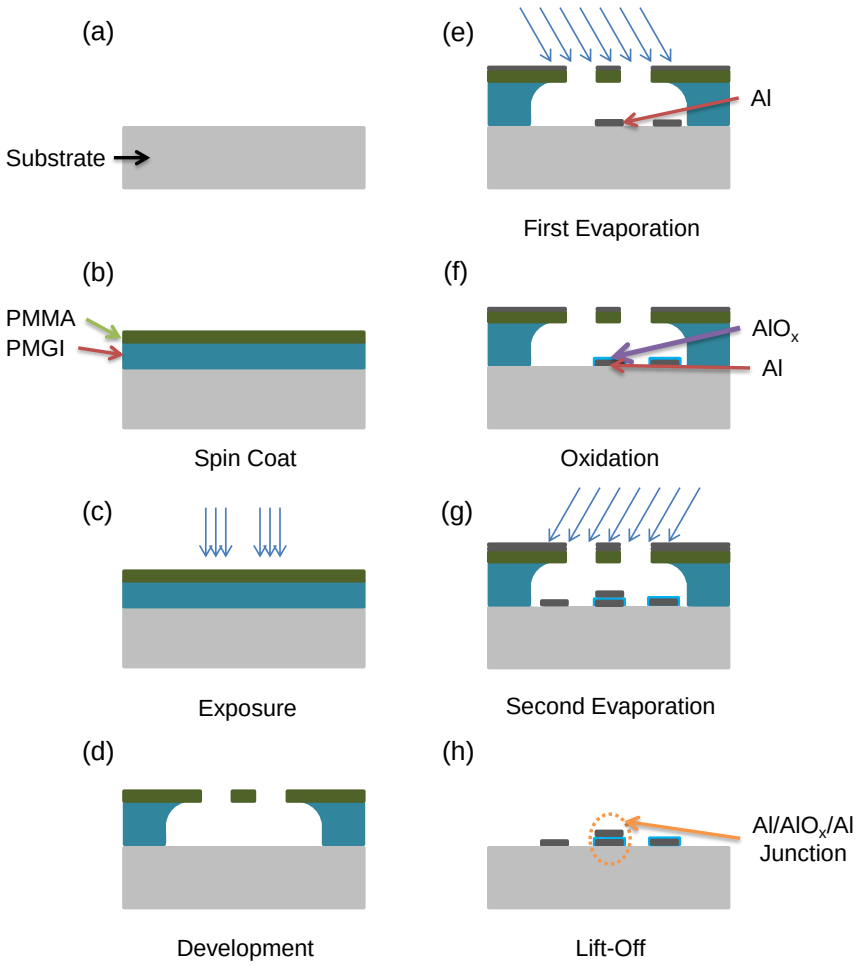

Figure 3.6: Fabrication steps of a Josephson junction. a) Substrate with resonator and capacitor layer is cleaned. b) It is spin coated with bilayer e-beam resists. c) The resist stack exposed with high keV EBL system (JEOL JBX-6300FS). d) Selective developing allows for fine structures on PMMA layer and undercut profile in PMGI layer. e) Argon milling and e-beam assisted directional evaporation of 40 nm Al at an angle of $+20^o$ to the normal of the surface defines the first Al layer. f) The first Al layer is oxidized for 7 minutes in an oxygen atmosphere. g) Second 65 nm thick Al layer is evaporated at an angle of -20^o. h) The device is cleaned and wire-bonded into microwave packaging for measurements.

3.4 Conclusions

In this chapter, the design and model for the capacitively shunted flux qubit are introduced. The resonator characteristics are determined by microwave simulation tools and the circuit capacitances are performed in EM simulation tools. With the fabrication parameters such as critical currents of the junctions and the complete capacitance matrix as input parameters, the qubit characteristics such as transition frequencies, charge and flux dependency, and transition rates are numerically calculated. This approach allows for a fine tuning of the design and fabrication parameters. Next, the fabrication methods are discussed. The design has large shunt capacitors which consists of the majority of the electrostatic energy stored in the qubit. The relatively large size of the pad offers reproducible and reliable fabrication with standard micro- and nano-fabrication steps.

Chapter 4

Characterization of capacitively shunted flux qubit

4.1 Introduction

In this chapter, we present experiments on the capacitively shunted flux qubit to determine the properties such as energy level structure and transitions. The experiments presented in this chapter are preliminary characterization of the device and serve as a basis for the experiments demonstrated in Chapter 5 and 6. In this chapter, first, the transmission spectrum of the coupled system is investigated. Second, the qubit transition frequencies are identified for the first three levels. The spectroscopy data is then compared to the numerical simulations performed in the previous chapter. Third, the coherent driven oscillations between the states of the qutrit space are shown. Last, the method for population extraction and determination of qubit effective temperature are presented.

4.2 Device configuration

The experiments are done with a superconducting flux qubit coupled to a coplanar waveguide (CPW) resonator, shown in Fig. 4.1(a). The qubit is formed of three large pads connected in a loop by three Josephson junctions, shown in Fig. 4.1(c). Two junctions are of equal size and the third is smaller by a factor $\alpha = 0.61$. The use of three large capacitive pads is intended to effectively reduce the participation ratio of electric fields in Josephson junctions and at metal surfaces and interfaces, as demonstrated in transmons [17] and then adapted to other types of superconducting qubits [61, 21]. The qubit is biased with

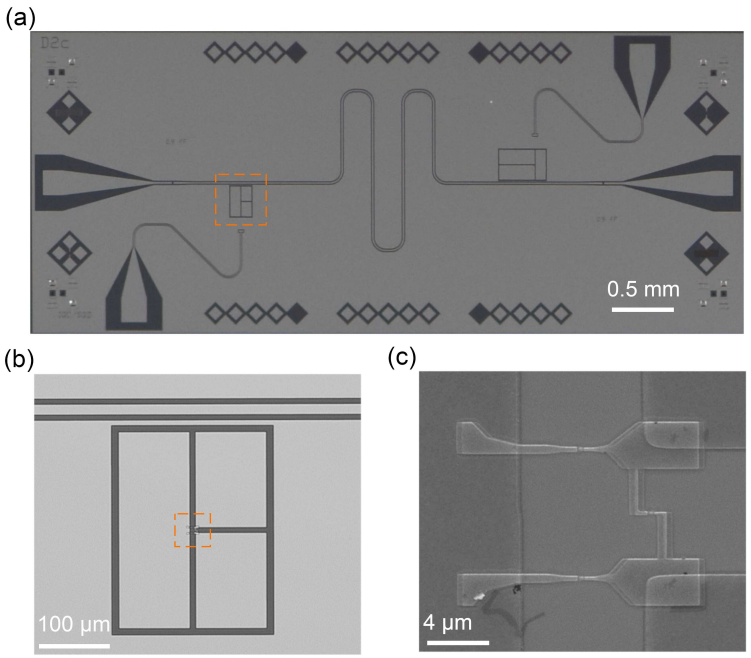

Figure 4.1: Image of the device used in the experiments. a) Photograph of the capacitively shunted flux qubit capacitively coupled to a CPW resonator. The dashed rectangle indicates the qubit with shunt capacitors used in the experiments b) Microscope image of the qubit shunting capacitors. The dashed rectangle indicates the position of the qubit loop and junctions. c) SEM image of the qubit loop and junctions placed in between the capacitor pads.

a magnetic flux Φ generated by an external coil. Transmission through the resonator is

used to measure the state of the qubit, based on dispersive-regime circuit-QED [25]. A coplanar waveguide terminated by a capacitive pad is used to drive transitions between different energy levels. The qubit is placed inside a sample holder at the mixing chamber of a dilution refrigerator. All transmission lines contain attenuators, low-pass filters, and infrared filters.

4.3 Transmission spectrum

We first present the transmission measurements of the coupled resonator and qubit system with applied external magnetic flux. The spectrum in Fig. 4.2 shows that the fundamental resonance frequency of the half wavelength CPW resonator is $\omega_r = 2\pi \times 6.719$ GHz. The quality factor of the resonator is determined by fitting the transmission spectrum with a Lorentzian function [62]. At low power, the internal quality factor of the resonator Q_i is saturating at 1.6×10^5 and the external quality factor Q_e is 1.7×10^5.

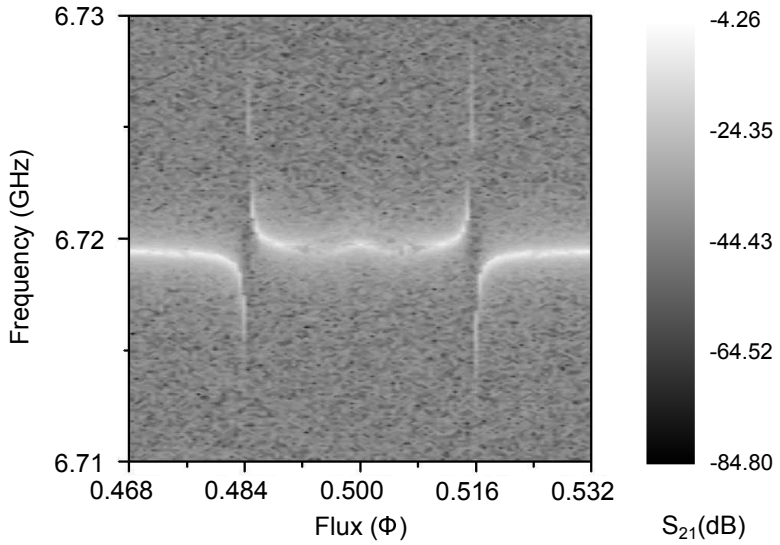

Figure 4.2: Transmission spectrum of the coupled qubit resonator system. The transmitted amplitude reaches maximum value when it is on resonance with the coupled system.

The transition frequencies of the flux qubit are tuned by the applied magnetic field. When the CPW resonator and the qubit energies are resonant, the degeneracy of the coupled system is lifted by the interaction term in the Hamiltonian in Eq. 2.75. The energy splitting depends on the coupling strength g. The avoided crossings in Fig 4.2 demonstrates a coupling strength g= 11.8 MHz, determined by the Jaynes-Cummings model in dispersive regime.

4.4 Qubit spectroscopy

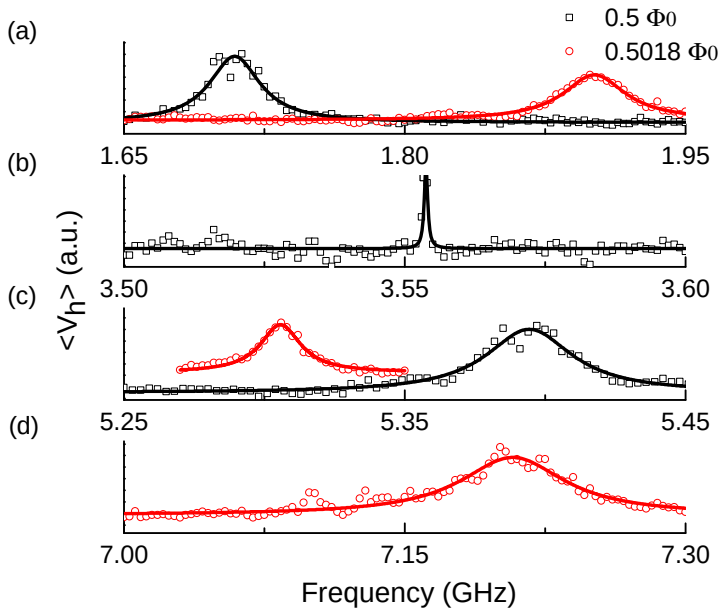

Figure 4.3: Readout homodyne voltage versus the spectroscopy pulse frequency. The spectroscopy peaks correspond to a) the 0-1 transition at the symmetry point and at 0.5018 Φ_0, b) the 0-2 two-photon transition at the symmetry point, c) the 1-2 transition at the symmetry point and at 0.5018 Φ_0, and d) the 0-2 transition at 0.5018 Φ_0. Solid lines represents Lorentzian fits.

To identify the qubit transitions frequencies, we next present the spectroscopy experiments. The qubit is driven by weak spectroscopy pulses with varying drive frequency at

various flux bias points. The readout of the qubit is done by homodyne voltage measurements in the dispersive regime. The readout setup is reported on previous work [48]. The readout pulse duration for spectroscopy experiments were 10 μs long and the corresponding state voltages are averaged over this period. In Fig. 4.3 we show the readout result, given by the average homodyne voltage, versus frequency of an applied spectroscopy pulse, for two values of the applied magnetic flux, $\Phi = 0.5\ \Phi_0$ (the flux symmetry point) and $\Phi = 0.5018\ \Phi_0$. At the symmetry point, we observe a peak at the transition frequency $\omega_{01} = 2\pi \times 1.708$ GHz between states 0 and 1 and a peak at $\omega_{02}^{\mathrm{tp}} = 2\pi \times 3.553$ GHz, a two-photon transition between states 0 and 2. At $\Phi = 0.5018\ \Phi_0$, we observe the 0-1 transition as well as the 0-2 transition, with the latter absent at the symmetry point due to selection rules [58]. The 1-2 transition can be observed after applying a 0-1 pumping tone. The

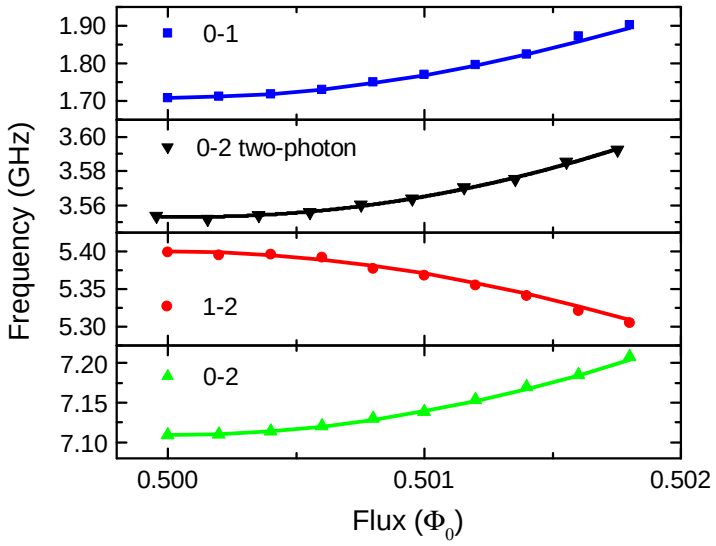

Figure 4.4: Transition frequencies of the shunted qubit versus the external magnetic flux. a) 0-1 transition, b) 0-2 two-photon transition, c) 1-2 transition, and d) 0-2 transitions. Solid lines represents fits based on two-level model.

transition frequencies ω_{01}, $\omega_{02}^{\mathrm{tp}}$ ω_{12}, and ω_{02}, for a range of applied magnetic flux, are shown in Fig. 4.4. The spectroscopy data is in excellent agreement with a model of the qubit based on the complete capacitance matrix extracted from electromagnetic simulations and

the critical currents of the junctions used as the only fit parameters (see Chp. 3). The best fit corresponds to a critical current $I_c = 3.96$ μA for the large junctions with area 0.042 μm^2 and $\alpha = 0.61$, which are in very good agreement with the device fabrication nominal parameters.

At the symmetry point, the qubit energy levels have large anharmonic structure. The anharmonicity, defined as $\mathcal{A} = \omega_{12} - \omega_{01}$, is found to be $2\pi \times 3.682$ GHz. The large anharmonicity allows one to assume the two level approximated Hamiltonian $H_{TLS} = -\hbar\Delta/2\sigma_x - \epsilon/2\sigma_z$ where Δ is the minimum energy difference between the qubit states and $\epsilon = 2I_p(\Phi - \Phi_0/2)$ with the persistent current I_p. From the ω_{01} transition versus external flux Φ, the persistent current is found to be $I_p = 75.4$ nA. Similarly the two level model can be applied to the 1-2 and 0-2 transition separately. The corresponding persistent currents for the 1-2 and 0-2 transitions are found to be 86.6 nA and 103.5 nA, respectively.

4.5 Readout histograms

In this section, the readout voltages for the corresponding states are shown. The control pulses used in state preparation are indicated as rotations on the Bloch sphere and denoted by $R_n^{ij}(\theta)$ where n is rotation axis, i and j are the transition levels, and θ is the rotation angle which is determined by the Rabi oscillations. The readout homodyne voltage is averaged over number of measurements. Figure 4.5 shows the readout histogram at flux-symmetry point for the states g, e, and f with 8192 measurements. The states g, e, and f are prepared by waiting for thermalization, applying a $R_x^{01}(\pi)$ pulse, and applying a $R_x^{01}(\pi)$ followed by a $R_x^{12}(\pi)$ pulse on the thermalized state, respectively. The pulses denoted by $R_x^{01}(\pi)$ and $R_x^{12}(\pi)$ are rotations around the x axis in the Bloch sphere for 0-1 and 1-2 subspace, respectively. Throughout the experiments, the population on state 0 in the thermal state is found to be 0.95 ± 0.02.

At the symmetry point, the state contrast is 88% and it is mainly limited by the errors in the initial state preparations associated with the non-zero populations of the excited

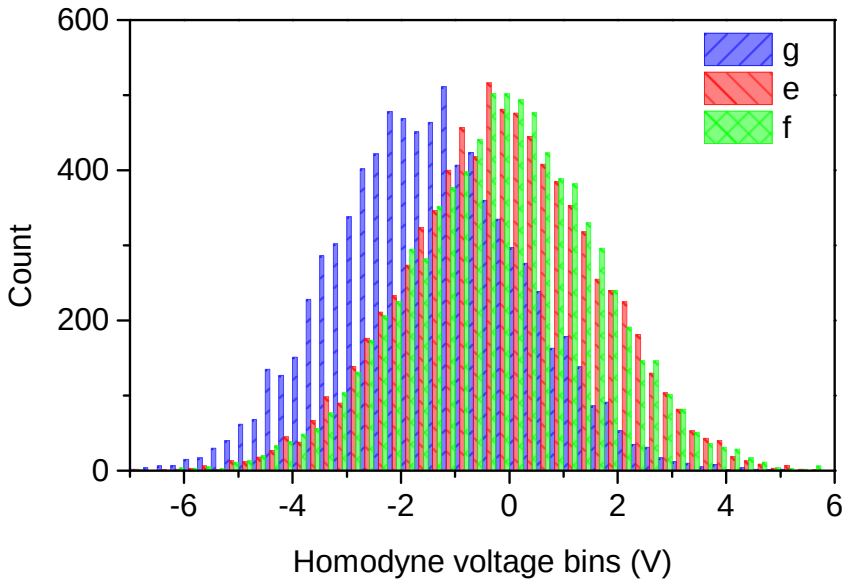

Figure 4.5: Readout histograms of three-level system. Number of counts of the measured voltage bins for prepared states g, e, and f are shown for total of 8192 measurements.

states due to thermalization. The qubit thermalized state includes populations from the state 0 and state 1 with a proportion which depends on the temperature and the transition frequency. The contrast between states e and f is poor, therefore the data of the experiments including state e and f are mapped to states g and e.

4.6 Rabi oscillations

In this section we present the Rabi oscillations in the transitions identified in the spectroscopy experiments. The experiment sequence includes repetitions of state reset, qubit control, and state readout protocols. The state reset is done by waiting at least ten times the qubit relaxation time to for qubit to relax and reach the thermal equilibrium state. The qubit control pulses are shaped cosine waveforms with a cosine rise and fall of the envelope. The Rabi pulses used in the experiments are generated with a Tektronix 70001A

arbitrary waveform generator which has a sampling rate of 50 GS/s. The rise and fall times in the Rabi drive pulses are 1 ns.

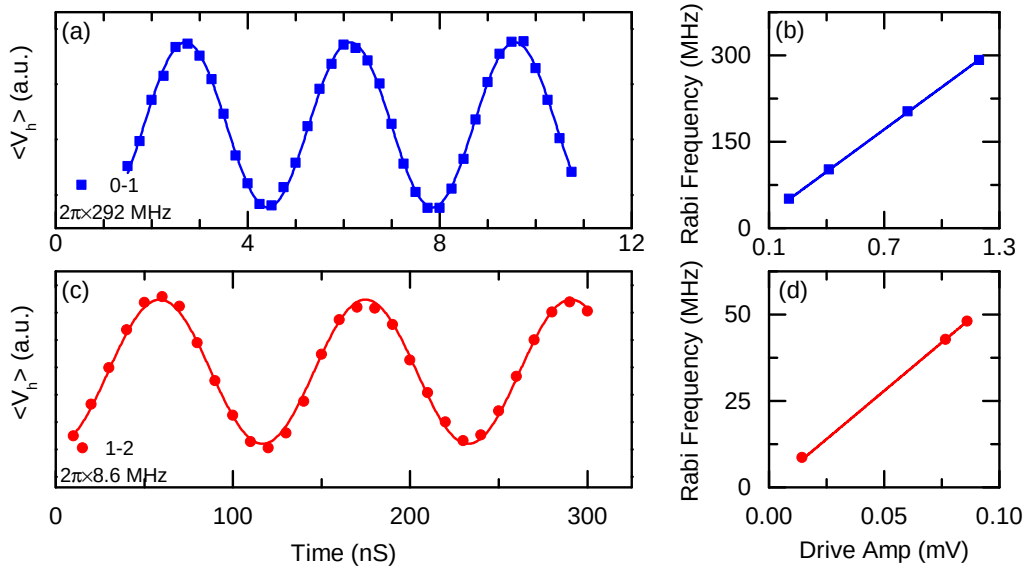

Figure 4.6: Rabi oscillations at the symmetry point. The oscillations are observed between states a) 0 and 1, and c) 1 and 2. Solid lines represent the sinusoidal fits. The linear dependency of the Rabi frequency on the drive amplitude is shown for b) 0-1 and d) 1-2 transitions. Solid lines represent the linear fits.

The Rabi experiments are performed between the first three energy levels. For oscillations between states 0 and 1, after the state reset, a Rabi drive resonant with 0-1 transition frequency is applied. This drive moves the qubit population from 0 towards 1 and vice versa. The state readout is performed and the homodyne voltage is measured by repeating the experiment with increased pulse duration. Figure 4.6(a) shows the oscillations between state 0 and 1 versus the pulse duration indicating that the qubit population swaps. With the maximum drive amplitude available in the experimental setup, we observe an oscillation frequency of $2\pi \times 292$ MHz. Figure 4.6(b) shows the linear dependency of the oscillation frequency on the driving amplitude.

For oscillations between states 1 and 2, after qubit reset, a $R_x^{01}(\pi)$ pulse is applied to

move the qubit to state 1. Next, a Rabi drive resonant with the 1-2 transition is applied. Figure 4.6(c) shows the Rabi oscillations between state 1 and 2 versus pulse duration and the oscillation frequency shows a linear dependency on the drive amplitude, as shown in Fig. 4.6.(d).

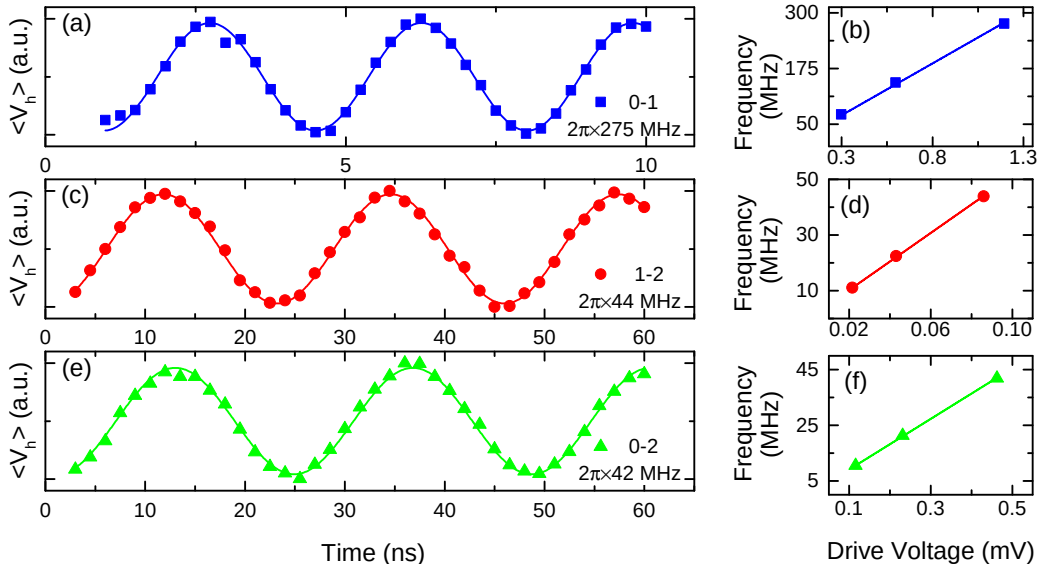

Figure 4.7: Rabi oscillations at $\Phi = 0.501\Phi_0$. (a),(c), and (e) shows sinusoidal oscillations between states 0-1, 1-2, and 0-2, respectively. Solid lines represents sinusoidal fits. (b),(d), and (f) shows the linear dependency of the Rabi frequency to the drive amplitude. Solid lines represent linear fits.

Away from the symmetry point, all three transition are allowed. Figure 4.7 shows the Rabi oscillations between states 0-1, 1-2, and 0-2 at $\Phi = 0.501\Phi_0$. In addition, the readout histograms show good contrast between all three states.

4.7 Population extraction and effective temperature

In the steady state, where the qutrit relaxes and reaches a thermal equilibrium, the populations of the states 0, 1, and 2 depends on the transition frequencies and temperature

of the bath coupled to qubit. It is assumed that the population of state 2 is negligible as the energy gap for this transition is large ($\omega_{02} = 2\pi \times 7.107$ GHz). The steady state populations P_{ss0} and P_{ss1} of state 0 and 1 respectively are determined by performing Rabi oscillations on two different prepared states. The first state preparation is done by waiting long enough for the qutrit to thermalize. The second state preparation is done by applying a π_x^{01} pulse followed by a π_x^{12} pulse to a thermalized state. This method is similar to the approach used in Jin et al. [63], with the difference that the preparations are chosen such that Rabi oscillations for the 0-1 transition are compared, where the readout contrast is optimized for this qubit. The steady state population P_{ss0} can be found as

$$P_{\mathrm{ss0}} = \frac{A_0}{A_1 + A_0}, \tag{4.1}$$

where A_0 and A_1 are Rabi oscillation amplitudes corresponding to the two preparations described above. In the coarse of the experiments P_{ss0} is found to be 0.95 ± 0.02 indicating an effective temperature, calculated based on $P_{\mathrm{ss1}}/P_{\mathrm{ss0}} = \exp(-\hbar\omega_{01}/K_{\mathrm{B}}T)$, of 27-32 mK. The effective temperature is very close to the cryostat temperature of 27 mK, in contrast to other reported results on long coherence time superconducting qubits, where larger differences between effective temperature and cryostat temperature were observed [64, 65].

For experiments including the higher levels, it is important to understand the properties of the readout. For a qutrit, formed by the lowest three energy levels, we model the homodyne voltage as $V_h = V_{h0}P_0 + V_{h1}P_1 + V_{h2}P_2$, where P_0, P_1, and P_2 are the probabilities and V_{h0}, V_{h1}, and V_{h2} are the signal levels corresponding to states 0, 1, and 2, respectively. To determine the signal levels, we measure V_h for three preparations. The first preparation is the qutrit thermalized state, obtained after a sufficiently long waiting time, for which $P_0 = P_{\mathrm{ss0}}$, $P_1 = P_{\mathrm{ss1}}$, and $P_2 = 0$. The second preparation consists of applying a π_x^{01} pulse after thermalization, which results in $P_0 = P_{\mathrm{ss1}}$, $P_1 = P_{\mathrm{ss0}}$, and $P_2 = 0$. The third preparation is done by applying π_x^{01} and π_x^{12} pulses after thermalization, for which $P_0 = P_{\mathrm{ss1}}$,

$P_0 = 0$, and $P_2 = P_{\mathrm{ss}0}$. The state voltage levels can be calculated by

$$\begin{pmatrix} V_{h0} \\ V_{h1} \\ V_{h2} \end{pmatrix} = \begin{pmatrix} P_{\mathrm{ss}0} & P_{\mathrm{ss}1} & P_{\mathrm{ss}2} \\ P_{\mathrm{ss}1} & P_{\mathrm{ss}0} & P_{\mathrm{ss}2} \\ P_{\mathrm{ss}1} & P_{\mathrm{ss}2} & P_{\mathrm{ss}0} \end{pmatrix}^{-1} \begin{pmatrix} V_0 \\ V_1 \\ V_2 \end{pmatrix}, \tag{4.2}$$

where V_0, V_1, and V_2 are the measured homodyne voltages for the prepared states above.

4.8 Conclusions

In this chapter we presented the transmission spectrum of the coupled qubit resonator system where the readout is done by dispersive methods. We presented the energy level spectrum of the qubit which is in excellent agreement with the qubit simulations based on the circuit model with the complete capacitance matrix of the system and nominal fabrication parameters. We also showed that the device is driven coherently in the qutrit subspace. We presented a method to determine the steady state populations of the thermalized state.

Chapter 5

Characterization of multi-level dynamics and decoherence in a high-anharmonicity capacitively shunted flux qubit

In this Chapter, we present the design and characterization of a three-Josephson junction superconducting loop circuit with three large capacitive shunting pads. This circuit is coupled capacitively to a resonator used for dispersive readout and to a capacitive driving pad for resonant control. We first discuss detailed experiments on this circuit used as a qubit, formed by the circuit lowest energy states 0 and 1. At the flux symmetry point the qubit relaxation time reaches as high as $T_1 = 47\,\mu$s and the spin-echo dephasing time $T_{2E} = 9.4\,\mu$s. The coherence time is increased with dynamical decoupling, reaching $26.5\,\mu$s with $N = 100$ Carr-Purcell-Meiboom-Gill pulses applied. We discuss in detail possible mechanisms for decoherence at the symmetry point. The dephasing time away from the flux symmetry point is proportional with coupling to flux fluctuations. We performed detailed spectroscopy and coherence experiments of this circuit used as a qutrit, involving

the lowest three levels 0, 1, and 2. The dependence of the transition frequencies and selection rules on magnetic flux is in excellent agreement with a complete circuit model based on the system capacitance matrix. We performed coherence experiments for the qutrit at the flux insensitive point, allowing to extract the energy relaxation and excitation rates, as well as the Ramsey coherence rates for all the three pairs of states involved. At the flux symmetry point, the circuit has a large anharmonicity, defined as the difference between the 1-2 and 0-1 transition frequencies, approaching $2\pi \times 3.69$ GHz, enabling fast single qubit operations. We performed randomized benchmarking with qubit gates with a duration of 2.64 ns, and an average gate fidelity of 99.9 %. These results demonstrate interesting potential for use of these circuits to implement fast two-qubit gates, enabled by the high anharmonicity, and for multi-level quantum logic.

5.1 Introduction

Recent years were marked by major progress in gate-model quantum computing implementations, leading to the development of small prototypes with sizes reaching tens of qubits [66, 67, 68, 69, 70]. Superconducting quantum bits in particular received attention as one of the most promising platforms from the perspective of scalability [71, 72]. Despite these advances, research on the fundamental building blocks of a superconducting quantum computer, quantum bits and methods for implementation of elementary single and two-qubit gates, remain a highly relevant research topic. Single- and two-qubit gate fidelities have only approached or marginally exceeded the error tolerance threshold for the surface code [73, 74]. Reducing gate errors has the potential to lead to a dramatic reduction in fault tolerant operation overhead [75] and is relevant for non-error-corrected near-term quantum devices [76]. Gate errors are impacted by both qubit coherence times and gate speed, and more generally by architecture details; this complete design space has been only partially explored in superconducting devices.

The spectroscopy experiments and population analysis discussed in the previous chapter

serve as a basis for the experiments presented in this chapter. We present experimental results on a superconducting qubit design that combines long coherence times, of 40 μs for energy relexation and 9.4 μs for spin-echo dephasing, with high level anharmonicity, approaching $2\pi \times 3.69$ GHz. Level anharmonicity is the difference between the first two transition frequencies, ω_{12} and ω_{01}, with 0 and 1 the first two energy eigenstates, used as qubit computational states, and 2 the second excited state. Anharmonicity has a direct impact on the speed of single qubit gates [77, 78] and identified to be a limiting factor for the speed of two-qubit gate implementations [79]. We demonstrate fast single-qubit gates, with duration of 1.62 ns for a $\pi/2$ pulse and 2.64 ns for a π pulse, and a high fidelity, characterized using randomized benchmarking, reaching 99.9 %. We expect the large anharmonicity of this design, combined with the long coherence times, to lead in the future to fast and high-fidelity gates. Moreover, we performed experiments in which we characterized decoherence and controlled this device in the qutrit space (formed by states 0, 1, and 2). Qutrit control and coherence bear relevance for qubit gates that make use of the properties of higher levels and is more broadly relevant for quantum protocols based on multi-level logic [80, 81, 82]. These results are enabled by a flux-type qubit design with three junctions with large planar capacitive shunts. Previous work on capacitively shunted flux qubit circuits focused on single shunt designs and dynamics and properties of the lowest two levels. You *et al.* proposed using capacitive shunting to reduce charge noise induced decoherence [20, 61]. More recently Yan *et al.* [21] performed a systematic study of flux qubits with single capacitive shunts, and demonstrated high coherence and a moderate anharmonicity of the order of 0.5 GHz in optimized samples. Stern *et al.* [83] demonstrated relatively long energy relaxation times in flux qubits coupled to three-dimensional cavities, suitable for hybrid experiments.

5.2 Qubit coherence at the symmetry point

We next discuss the qubit coherence characterization at the symmetry point ($\Phi = 0.5\ \Phi_0$). Fig. 5.1(a) shows an energy relaxation time measurement, with the qubit excited with a π_x^{01} rotation, resonant with the 0-1 transition. The measured T_1 had systematic fluctuations in the course of experiments, with typical values in the $40 \pm 5\,\mu$s range, as observed in other experiments with superconducting qubits [84, 85, 86]. In the course of the experiments, T_1 reached as high as $T_1 = 47.1 \pm 2.0\,\mu$s, which is comparable to the best result reported previously on a capacitively shunted flux qubit design with moderate anharmonicity [21]. The Ramsey and spin-echo coherence times were found to be $T_{2R} = 4.7\,\mu$s and $T_{2E} = 9.4\,\mu$s.

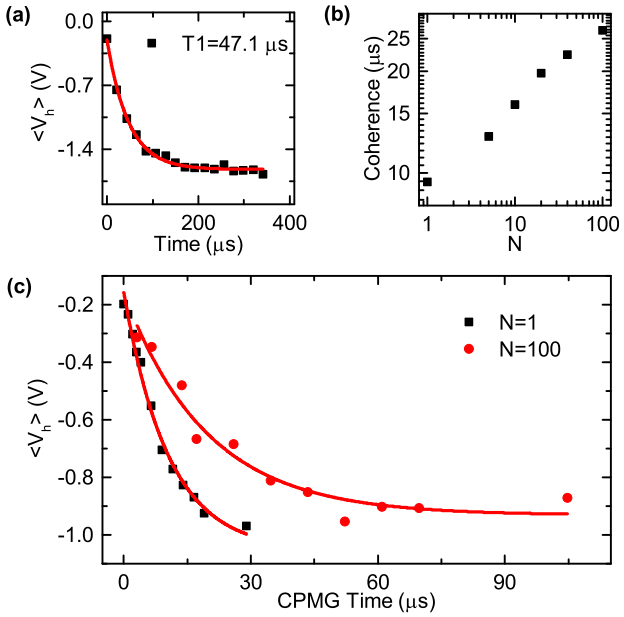

Figure 5.1: Coherence times at the flux symmetry point. a) Readout voltage versus delay time after a π^{01} pulse is applied to the qubit thermalized state. The solid line is an exponential fit, leading to a relaxation time $T_1 = 47.1\mu$s. b) Coherence time versus the number of pulses N in CPMG sequence. c) Homodyne voltage versus CPMG time for N=1 (black squares) and N=100 (red dots). Solid lines represent exponential fits.

For both type of measurements, exponential decay as opposed to Gaussian decay led to a better fit in general. We performed dephasing measurements with dynamical decoupling

based on Carr-Purcell-Meiboom-Gill (CPMG) pulse sequences with π pulse duration of 11.9 μs. The coherence time versus the number of pulses is shown in Fig. 5.1(b). The coherence time reaches $T_{\mathrm{CPMG}} = 26.5\,\mu\mathrm{s}$ for $N = 100$ pulses.

5.3 Multi-level relaxation and dephasing

We performed experiments addressing coherence in the qutrit space. In Fig. 5.2(a), we show the result of a multilevel relaxation experiment. Two pulses, π_x^{01} and π_x^{12}, are applied to excite the system to state 2 and the populations are measured versus time. The continuous lines are fits with a multi-level relaxation model (see Appendix A). In the fit, the 0-1 relaxation (Γ_{10}) and excitation (Γ_{01}) rates are set based on the measurements of the qubit relaxation time and thermal populations. The ratios Γ_{12}/Γ_{21} and Γ_{02}/Γ_{20} are set equal to the corresponding Boltzmann factors, assuming the temperature T_{qb} extracted from qubit thermalization experiments, and Γ_{21} and Γ_{20} are free parameters. We note that the constraints on the ratios of the 1-2 and 0-2 rates does not significantly impact the values of the relaxation rates. Based on a fit of the variation of the populations with time, we extract the following relaxation rates: $\Gamma_{21} = 124.3$ kHz and $\Gamma_{20} = 27.8$ kHz. We performed similar multi-level relaxation experiments away from the symmetry point, at $\Phi = 0.501\,\Phi_0$, and we found comparable energy relaxation times of the order of 10 μs (see Appendix A). We also performed multi-level coherence experiments for the three pairs of levels involved. Figure 5.2(b) shows Ramsey oscillations for coherent superpositions of states at the flux symmetry point. The decay curves are in excellent agreement with a model that includes state preparation, the interlevel relaxation and excitation rates, and low frequency noise modeled as a classical Gaussian stochastic process (see Appendix A).

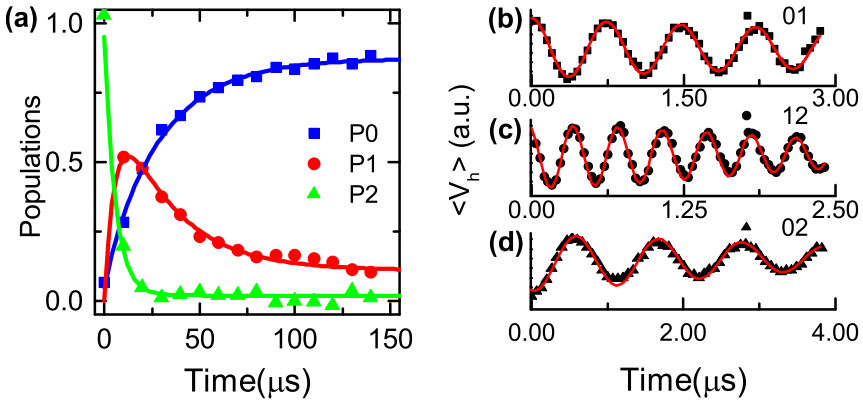

Figure 5.2: Multi-level decoherence. a) Population versus delay time after a π_x^{01} and a π_x^{12} pulse are applied to qutrit thermal state for levels 0 (blue squares), 1 (red dots), and 2 (green triangles). (b-d) Ramsey oscillations with time for coherent superposition of states b) 0 and 1, c) 1 and 2, and d) 0 and 2, with Ramsey coherence times 4.7, 3.4, and 5.4 μs, respectively.

5.4 Qubit coherence away from the symmetry point

We measured the qubit coherence time for a range of magnetic fluxes. The spin-echo rate is shown as a function of the flux sensitivity coefficient $\frac{\partial\omega_{01}}{\partial\Phi}$ in Fig. 5.3. The nearly linear dependence is in line with other experiments and indicative of low frequency flux noise [87, 48]. Detailed measurements of coherence with CPMG pulse sequences were done at a flux $\Phi = 0.501\,\Phi_0$, for various pulse sequence lengths N. The dephasing rate changes from 1.4 μs for $N = 1$ to 6.8 μs for $N = 100$, with approximately a $N^{0.42}$ dependence. At $\Phi = 0.501\,\Phi_0$, we have measured in addition the Ramsey dephasing times for superpositions of states 0-1 and 0-2; we obtained the dephasing rates 2.7 MHz and 0.9 MHz respectively.

5.5 Discussion of coherence

We now discuss the results obtained for qubit coherence, starting with pure dephasing. The nearly linear dependence of the Ramsey and spin-echo dephasing rates on the flux coupling coefficient $\frac{\partial\omega_{01}}{\partial\Phi}$ (see Fig. 5.3) demonstrates that dephasing away from the symmetry point

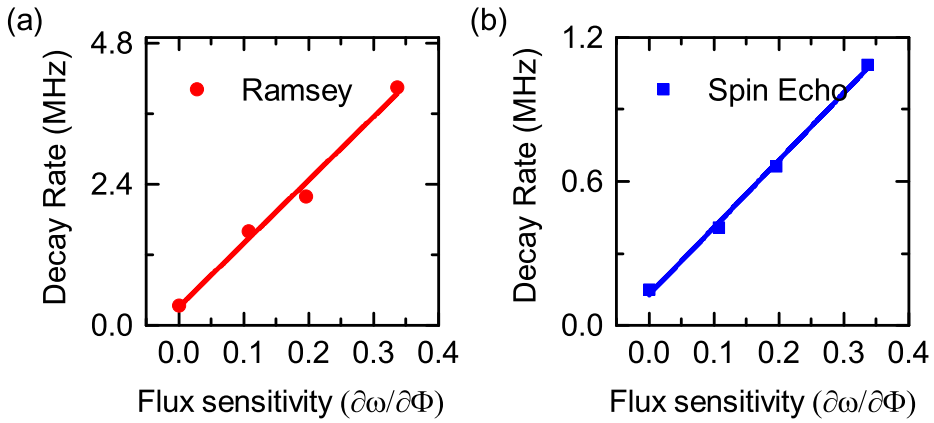

Figure 5.3: a) Ramsey and b) Spin-echo decay rates versus the flux sensitivity coefficient.

is dominated by flux noise, and is indicative of flux noise with a power spectral density (PSD) of the form $A/|\omega|^{\alpha}$, where ω is the frequency, A characterizes the strength of the noise, and $\alpha \approx 1$ [87, 48]. At $\Phi = 0.501\,\Phi_0$, the coherence rate with CPMG pulses changes as $N^{-\beta}$. This is indicative of low-frequency noise with a power density $A/|\omega|^{\alpha}$, where $\alpha = \beta/(1-\beta)$ (see Appendix A). This allows extracting $A = 1.8 \times 10^{-14}\,(\mathrm{rad/s})^{\alpha-1}\Phi_0^2$ and $\alpha = 0.68$; note that these values hold over the frequency range where the CPMG pulses are sensitive to flux noise, corresponding approximately to $3.1 - 46.3$ MHz. The Ramsey dephasing rates for 0-1 and 0-2 coherences at $\Phi = 0.501\,\Phi_0$ are in a ratio proportional to the flux sensitivity coefficients, suggesting that flux noise is the dominant dephasing source for higher levels as well. At the symmetry point, we considered various possible explanations for the observed coherence times. Photon dephasing is expected to be weak, due to the weak coupling to the cavity, with a dispersive shift $\chi = 0.5$ MHz. However, with numerical simulations we found that with $n_{\mathrm{th}} = 0.15$ the observed decay times in simulations are close to experimental values for up to 10 CPMG pulses, but become up to a factor of two longer for larger numbers of CPMG pulses. The value $n_{\mathrm{th}} = 0.15$ corresponds to an effective temperature of 160 mK, which is much larger than expected. This value could be due to ineffectively suppressed excess noise or possibly to coherent leakage of radiation leading to a comparable average photon number. We next considered the role

of charge noise. With the qubit parameters determined from experiment, the modulation of the transition frequencies 0-1, 1-2, and 0-2 over the full charge periodicity interval is $2\pi \times 133$ Hz, $2\pi \times 626$ Hz, and $2\pi \times 493$ Hz respectively, which should induce a negligible contribution to dephasing. Finally, we considered flux noise. The role of flux noise at sweet spots has been considered theoretically in the past for particular types of noise [88]. We resorted to a numerical simulation of dephasing induced by randomly generated noise. If we assume that the PSD of flux noise is $A/|\omega|^{\alpha}$, with A and α as determined based on the CPMG measurements at $\Phi = 0.501\,\Phi_0$, but extrapolated to a a very broad frequency interval, beyond the noise spectroscopy range of range $0.1 - 46$ MHz, then the numerical simulations give negligibly low coherence rates, of the order of 1 kHz. We cannot exclude the possibility that significant departures of the flux noise PSD from the dependence in the CPMG spectroscopy range would explain the observed coherence time at the symmetry point. Finally, we comment briefly on energy relaxation. The long energy relaxation times are comparable to the longest observed for planar qubits, indicating that dielectric loss contributions are effectively suppressed.

5.6 Randomized benchmarking of single-qubit gates

We performed the randomized benchmarking protocol [89, 90] to measure the average fidelity of the gates. The gates used in the experiments are implemented by shaped pulses which have an envelope that has cosine-shaped rise and fall parts and a flat top. The duration of the $\pi/2$ and π pulses are 1.62 and 2.64 ns long, respectively with 0.6 ns of rise and fall times. In the benchmarking experiments, a random sequence of gates with length $2N+1$ is generated and the sequence is applied on the thermalized state with known populations. The generation is done by selecting a random gate from the Clifford group and a random gate from Pauli group and repeating this selection N times. A final gate from either group is appended to project the resulting state to initial state. At the end of each sequence, the average homodyne voltage is measured. For a given length $2N + 1$, 32

random sequences are generated. Figure 5.4 shows the average measured homodyne voltage

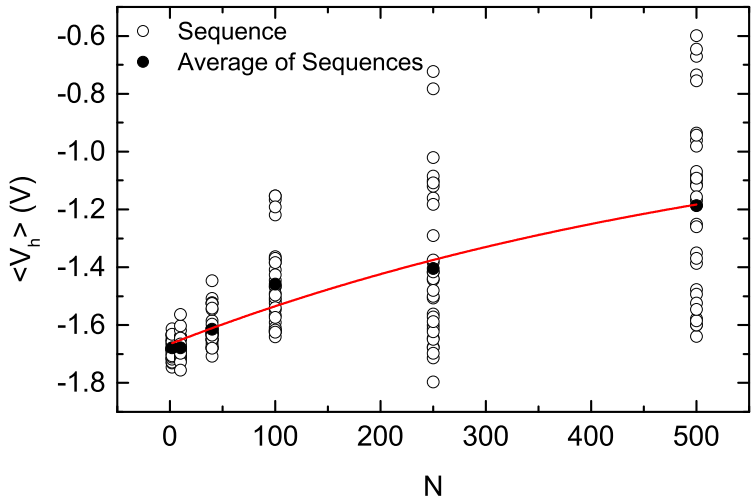

Figure 5.4: Homodyne voltage after randomized benchmarking sequence is applied to qubit thermal state versus the sequence length N. Black circles represent the measured voltage for each randomization of the sequence and black dots represents the sequence averages. The solid curve represents the fit with the decay function.

for each sequence (black circles) and for the averages of 32 sequences (black dots) versus the sequence length N. The average of sequences is fitted with a function $F = A_0 p^N + B_0$ where A_0 and B_0 are fit parameters corresponding to the errors associated with state preparation and measurement and p is related to the average error rate [90]. The average fidelity $F_{\text{ave}} = p + (1-p)/2$ is found to be $99.92 \pm 0.003\%$. We performed numerical simulations of the benchmarking protocol in qubit subspace including decoherence characteristics of the qubit in the lab frame. The simulations agree well with the experiments. We expect that the main limitation to average fidelity is the relatively strong drive strength of $2\pi \times 260$ MHz and shaping of the pulses. Experiments with optimized pulse shaping will be explored in future work.

5.7 Conclusions

In conclusion, we presented experimental results on a capacitively shunted flux qubit that combines high anharmonicity with long coherence times. The energy level structure and flux dependency of the transition frequencies agree well with the model based on the system capacitance matrix. Coherence experiments performed in qubit space show high energy relaxation time and indicates that the dephasing time is mainly limited by the low frequency flux fluctuations. We also demonstrated experiments with the multi-level control of the circuit and measured multi-level coherence in qutrit space. The experimental results are in good agreement with the multi-level decoherence models. We also demonstrated fast and high fidelity single qubit gates with randomized benchmarking protocol. The experimental results indicate a prospective use of the shunted flux qubits to implement fast two-qubit gates, enabled by the high anharmonicity and long coherence, and proves a potential use multi-level quantum logic.

Chapter 6

Implementation of a Walsh-Hadamard gate in a superconducting qutrit

We have implemented a Walsh-Hadamard gate, which performs a quantum Fourier transform, in a superconducting qutrit. The qutrit is encoded in the lowest three energy levels of a capacitively-shunted flux device, operated at the optimal flux-symmetry point. We use an efficient decomposition of the Walsh-Hadamard gate into two unitaries, generated by off-diagonal and diagonal Hamiltonians respectively. The gate implementation utilizes simultaneous driving of all three transitions between the three pairs of energy levels of the qutrit, one of which is implemented with a two-photon process. The gate has a duration of 36 ns and an average fidelity, including preparation and tomography errors, of 91%, characterized with quantum state tomography. We identify incomplete compensation of ac-Stark shifts as one of the primary limitations to the gate fidelity, and we show that significantly higher fidelities can be obtained using optimal pulse parameters.

6.1 Introduction

In recent years significant progress has been made towards the implementation of quantum computers. Current efforts are mainly focused on encoding quantum information using two-state systems, or qubits. Using multi-level systems, or qudits, instead of qubits to perform quantum information processing is a developing field that promises advantages in a number of areas of quantum information. Universal quantum control of qudits and quantum error correction approaches have been explored theoretically [81, 91, 92]. Recent theoretical work suggests that quantum error correction with qudits has potential advantages over qubit-based schemes [93, 80, 94, 95]. The experimental implementation of quantum computing based on qudits is still largely unexplored. Besides quantum computing, qudits have been explored as alternatives to qubits in other areas of quantum information, as an improved platform for quantum metrology [96] and quantum communication [97].

In this chapter, we report the implementation of the generalized Walsh-Hadamard gate in a superconducting three-state qudit, or qutrit. The Walsh-Hadamard gate is one of the elementary gates in qudit control, relevant for error correction [81, 91] and the implementation of the quantum Fourier transform in single- and many-qudit systems [98]. We use a fast single-pulse implementation of the gate based on a single rotation in the qutrit space. We note that superconducting devices provide a natural platform for the exploration of the physics of qutrits, with work to date including basic control and tomography [99], the use of the third level of a qutrit to facilitate two-qubit gates [100], wave mixing [101], holonomic gates [102], electromagnetic induced transparency [103], demonstration of quantum contextuality [104], and adiabatic state transfer protocols [105].

There have been several studies in the literature on decomposing qudit gates into sequences of simple steps, e.g. into a sequence of gates that each operates on two quantum

states [106, 107]. We use an implementation of the Walsh-Hadamard gate

$$U_{\mathrm{WH}} = \frac{1}{\sqrt{3}} \begin{pmatrix} 1 & 1 & 1 \\ 1 & e^{i\frac{2\pi}{3}} & e^{-i\frac{2\pi}{3}} \\ 1 & e^{-i\frac{2\pi}{3}} & e^{i\frac{2\pi}{3}} \end{pmatrix}. \tag{6.1}$$

that can be implemented in just two steps. Specifically, $U_{\mathrm{WH}} = U_{\mathrm{d}}\, U_{\mathrm{o}}$, with $U_{\mathrm{o}} = \exp(-G_{\mathrm{o}}t)$ and $U_{\mathrm{d}} = \exp(-G_{\mathrm{d}}t)$. The generators $G_{\mathrm{o}} = \left(\sum_{0\leq j<k\leq 3} m_{jk}|j\rangle\langle k|\right) + h.c.$ and $G_{\mathrm{d}} = \mathrm{diag}\,(\phi_0, \phi_1, \phi_2)$. This type of decomposition is well suited for superconducting qubits where the microwave based control allows for the application of broadband signals containing multiple frequency tones that can simultaneously drive transitions between different levels, allowing to readily implement G_{o}. The effect of the diagonal unitary U_{d} can be implemented without applying any additional pulses, but rather by shifting the phases of the drive fields in the next resonant control pulses. In our experiment, these phase shifts are applied to the tomography pulses. We found several decompositions of this type with different values of the complex numbers m_{01}, m_{02}, and m_{12} and real numbers ϕ_0, ϕ_1, and ϕ_2 and chose the decomposition which results in the shortest pulse duration for a given drive amplitude.

6.2 Device configuration

The device used in our experiments, shown in Fig. 4.1, is formed by a loop with three Josephson junctions with three large capacitor pads. The device is capacitively coupled to a co-planar waveguide half-wavelength resonator for dispersive readout and to a transmission line terminated by a capacitor pad for control. Similar devices, based on three Josephson junction loops with capacitive shunts, were employed as qubits encoded in the lowest two energy levels [20, 61, 21]. The control pulses are generated using direct synthesis by a fast arbitrary waveform generator (AWG TEK70001A) with a sampling rate of 50 GS/s. The pulses consist of single- and multi-tone signals with an envelope that has cosine-shaped

rise and fall parts and a flat top.

6.3 Quantum state tomography

To reconstruct the density matrix ρ of the qutrit, we use a quantum state tomography procedure, where the readout of the homodyne voltage is preceded by one of the 9 tomography pulses shown in Table 6.1. We choose the tomography pulses to optimize readout

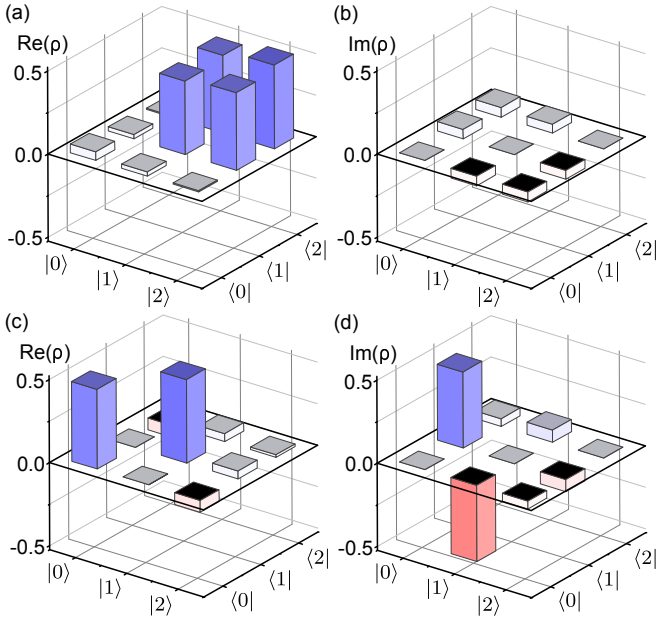

Figure 6.1: Density matrix elements reconstructed with tomography process. a) Real and b) elements of ρ for the state preparation with $R(\pi/2)^{12}_{y}$ $R(\pi)^{01}_{x}$ and c) real and d) imaginary elements of ρ for state preparation with $R(\pi/2)^{01}_{x}$.

based on the large difference between V_{h1} and V_{h0}; this set of pulses is different from the experiment by Bianchetti *et al.* [99], where contrast is maximum between states 1 and 2. The tomography pulses consist of combinations of rotations around the x and y axes of the Bloch sphere for the 0-1 (1-2) transitions, denoted by $R_{\alpha}^{01(12)}(\theta)$ where $\alpha = x, y$ is the rotation axis and θ is the rotation angle. Figure 6.1 shows the density matrices for

Table 6.1: Set of pulses used in state preparation and state tomography experiments.

State Prep.	Rotations	Tomog. Pulses	Rotations
p_0	I	u_0	$R_x^{01}(\pi)$
p_1	$R_x^{01}(\pi)$	u_1	$R_x^{01}(\pi/2)$
p_2	$R_x^{12}(\pi)R_x^{01}(\pi)$	u_2	$R_y^{01}(\pi/2)$
p_3	$R_x^{01}(\pi/2)$	u_3	I
p_4	$R_y^{01}(\pi/2)$	u_4	$R_x^{01}(\pi)R_x^{12}(\pi/2)$
p_5	$R_x^{12}(\pi/2)R_x^{01}(\pi)$	u_5	$R_x^{01}(\pi)R_y^{12}(\pi/2)$
p_6	$R_y^{12}(\pi/2)R_x^{01}(\pi)$	u_6	$R_x^{01}(\pi)R_x^{12}(\pi/2)R_x^{01}(\pi)$
p_7	$R_x^{12}(\pi)R_x^{01}(\pi/2)$	u_7	$R_x^{01}(\pi)R_y^{12}(\pi/2)R_x^{01}(\pi)$
p_8	$R_x^{12}(\pi)R_y^{01}(\pi/2)$	u_8	$R_x^{01}(\pi)R_x^{12}(\pi)R_x^{01}(\pi)$

two states. The first state is prepared by applying a $R_x^{01}(\pi)$ pulse followed by a $R_y^{12}(\pi/2)$ rotation and the second state is prepared by applying a $R_x^{01}(\pi/2)$ on the thermal state. The measured fidelity between the reconstructed density matrix and the expected state is 99.2% for both preparations.

6.4 Rabi oscillations on 0-2 two-photon transition

The implementation of the Walsh-Hadamard gate discussed above requires the simultaneous driving of all three qutrit transitions such that the effective Hamiltonian in the rotating frame has non-zero values for all off-diagonal matrix elements. While the 0-1 and 1-2 transitions are allowed and can be implemented by standard resonant driving, the 0-2 transition is forbidden at the symmetry point, and is therefore implemented as a two-photon process. Figure 6.2(a) shows the Rabi frequency of the two-photon oscillations between states 0 and 2 versus the detuning $\delta_{02}^{tp} = (\omega_{01} + \omega_{12})/2 - \omega_{\mathrm{d},02}^{\mathrm{tp}}$, where $\omega_{\mathrm{d},02}^{\mathrm{tp}}$ is the driving frequency. The Rabi oscillations have a minimum frequency at a detuning $\delta_{02}^{tp} = 2\pi \times 3.06$ MHz, due to ac-Stark shifting of the resonance. On resonance, the frequency of the Rabi oscillations depends quadratically on the drive amplitude (Fig. 6.2(b)), characteristic of a two-photon

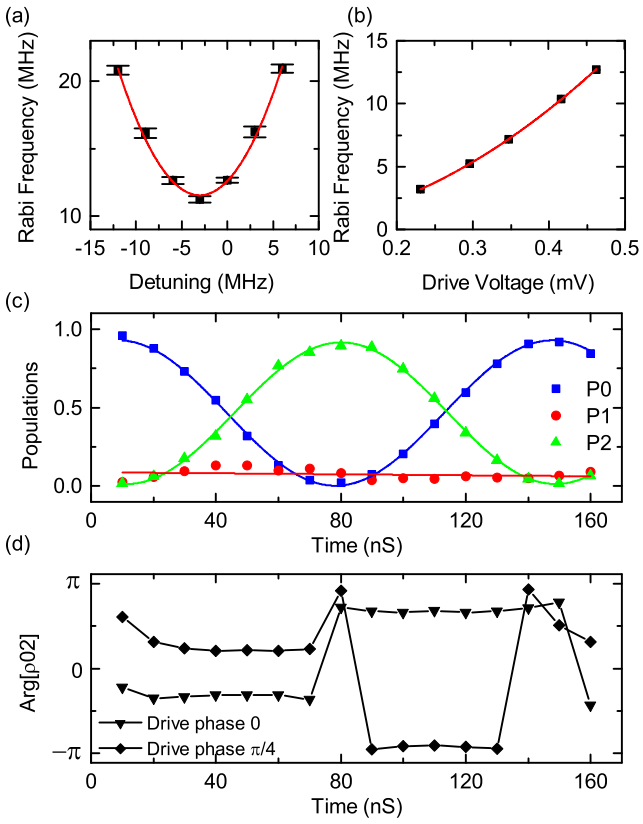

Figure 6.2: Rabi oscillations on 0-2 two-photon transition with populations. a) Frequency of the Rabi oscillations versus the detuning δ between the driving frequency and the two-photon resonance frequency $(\omega_{01} + \omega_{12})/2$. The line is a quadratic fit. b) The two-photon resonant-driving Rabi frequency versus the drive amplitude. The line is a quadratic fit. c,d) Results of the tomography experiments. Panel (c) shows the population of states 0 (blue squares), 1 (red disks), 2 (green triangles), versus the Rabi pulse duration, with oscillation frequency of $2\pi \times 7.1$ MHz. Panel (d) is the phase of the 0-2 component of the density matrix for two values of the phase of the driving field: 0 (triangles) and $\pi/4$ (rhombuses).

process. With driving resonant to the ac-Stark shifted transitions, we performed tomography experiments for various durations of the 0-2 Rabi pulse, shown in Fig. 6.2(c,d). The population oscillates between states 0 and 2, while the population of state 1 remains relatively constant at the level of the thermal state. The argument of the $\langle 0|\rho|2\rangle$ element of the density matrix ρ, shown in Fig. 6.2(d), is constant during each half-oscillation period,

indicating rotation around a constant axis in the $\{|0\rangle, |2\rangle\}$ subspace. The two data sets in Fig. 6.2(d) correspond to two values of the phase of the two-photon driving tone, different by $\pi/4$. The phase of $\langle 0|\rho|2\rangle$ changes by twice the driving tone phase, which is another indication that the transition is a two-photon process. The results of the two-photon driving tomography experiment agree with numerical simulations based on the multi-level Hamiltonian, with the amplitude of the driving voltage at the qutrit being the only adjustable parameter. We note that in the numerical simulations we only obtained good agreement when taking into account at least the lowest five energy levels, underscoring the importance of ac-Stark shifts in the experiment.

6.5 Characterization of the Walsh-Hadamard gate

We next present the characterization of the generalized Walsh-Hadamard gate. We use a decomposition where the off-diagonal generator has coefficients $m_{01} = 0.3491 + 0.6046i$, $m_{12} = -0.6981$, and $m_{02} = 0.3491 + 0.6046i$ and the diagonal generator has elements $\phi_0 = 6.1086$, $\phi_1 = 4.0143$, and $\phi_2 = 4.0143$. As mentioned above, the off-diagonal Hamiltonian that generates $U_{\rm o}$ is obtained by the simultaneous driving of the transitions 0-1, 1-2, and 0-2, with the latter being a two-photon process. The Rabi frequencies are $\Omega_{01} = \Omega_{12} = \Omega_{02} = 2\pi \times 7.1$ MHz. These Rabi frequencies are chosen proportional to m_{01}, m_{02}, and m_{12} and maximized to reach the maximum microwave amplitude available in our setup. We note that the control signal amplitude is not limited by the qutrit properties and larger driving amplitudes could in principle be reached by increasing signal transmission and the coupling to the capacitive driving line. In the experiments, the 0-2 two-photon drive frequency is detuned to be on resonance with the ac-Stark shifted 0-2 two-photon frequency and the 0-1 drive frequency is adjusted by twice the detuning. The diagonal Hamiltonian that generates $U_{\rm d}$ is effectively embedded in the tomography pulses by shifting the phases of the driving fields. The new tomography analyzer pulses are given by $\bar{u}_i = U_{\rm d}^\dagger u_i U_{\rm d}$. The pulse sequence is shown in Fig. 6.3(a). The off-diagonal Hamiltonian is applied on

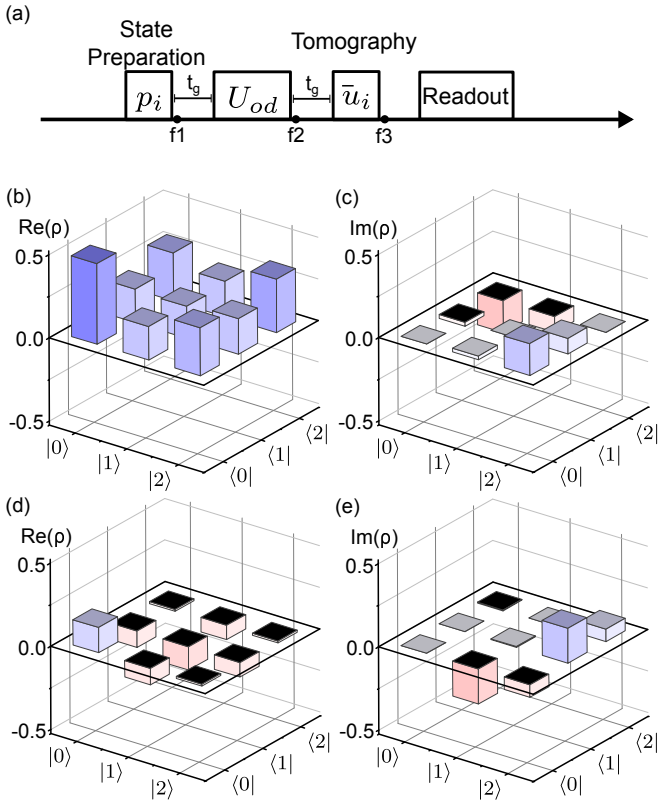

Figure 6.3: a) Pulse sequence used in the experiments. b) Real and c) imaginary parts of the reconstructed density matrix after the gate is applied on the thermalized state shows a 92.5% gate fidelity. The differences between the reconstructed and the expected density matrices are shown for the real and imaginary parts in panels (d) and (e), respectively.

the prepared states p_i followed by the phase-shifted tomography pulses $\bar{u}_i$ to complete the Walsh-Hadamard gate and to reconstruct the density matrix ρ of the state after the gate. The gate fidelity is measured with respect to the ideal evolution of the prepared state under the gate Hamiltonian in Eq. 6.1. Figure 6.3 shows the real (b) and imaginary (c) elements of ρ where the gate is applied on the qutrit thermal state. The fidelity of the gate in this case is 92.5%. The difference between the reconstructed and the expected density matrices are shown in Fig. 6.3(d) and (e) for the real and imaginary parts, respectively. Table 6.2 shows the fidelity values of the gate applied on 9 different prepared states. The state preparation pulses p_i and tomography analyzer pulses $\bar{u}_i$ are on resonance with the

drives in U_o. On average, the gate fidelity at the end of the sequence is observed to be 90.85%.

Table 6.2: Set of pulses used to prepare different states to which the Walsh-Hadamard gate is applied and measured fidelities.

State preparation (p_i)	Fidelity
I	92.5%
$R_x^{01}(\pi)$	91.5%
$R_x^{12}(\pi)\ R_x^{01}(\pi)$	92.9%
$R_x^{01}(\pi/2)$	91.1%
$R_y^{01}(\pi/2)$	89.1%
$R_x^{12}(\pi/2)\ R_x^{01}(\pi)$	94.4%
$R_y^{12}(\pi/2)\ R_x^{01}(\pi)$	88.6%
$R_x^{12}(\pi)\ R_x^{01}(\pi/2)$	88.4%
$R_y^{12}(\pi)\ R_x^{01}(\pi/2)$	89.1%
Average	90.85%

6.6 Simulations

We next show the results of numerical simulations of the complete pulse sequence for all preparations listed in Table 6.2. The simulations are based on the system Hamiltonian with driving including the lowest five energy levels of the system which is given by

$$H(t) = \sum_{i=1}^{n} \hbar\omega_{0i}|i\rangle\langle i| + \sum_{\substack{i,j=0 \\ i\neq j}}^{n} A(t)g_{ij}|i\rangle\langle j|, \tag{6.2}$$

where n is the number of energy levels. The transition matrix elements g_{ij} for the qutrit are determined from the circuit model. The voltage waveform $A(t)$ for the pulse sequence including the state preparation, the off-diagonal part of the Walsh-Hadamard gate, and tomography pulses is generated by the drive frequencies, phases and amplitudes used in the experiments. The simulation parameters are confirmed by the frequency dependent

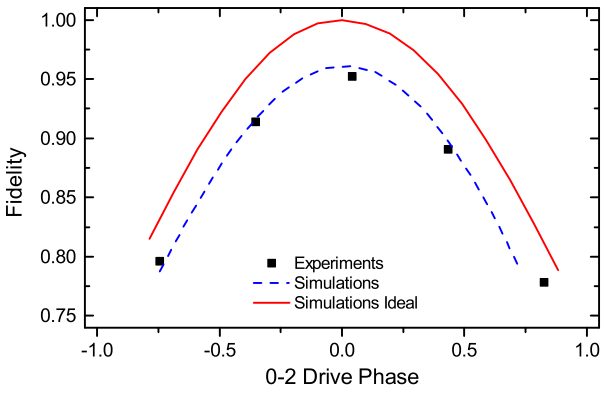

Figure 6.4: Fidelity after the off-diagonal part of the gate versus the 0-2 two photon drive phase. Black squares shows the experimental results when the gate is applied on the qutrit thermal state. The dashed blue line is the result of simulations replicating the experimental conditions. The red solid line represents the fidelity **if** all three transitions of the gate were on resonance with the ac-Stark shifted frequencies.

transmission of the experimental setup and individual Rabi oscillation simulations. The ac-Stark shifted 0-2 two photon frequency is determined by sweeping the drive frequency to obtain resonant Rabi oscillations. The 0-1(1-2) shifted frequency are determined by applying a detuned 0-2 two-photon drive (30 MHz) such that the oscillations are suppressed but the drive field is kept on. Next, the 0-1(1-2) is driven with frequency sweeps to observe resonant Rabi oscillations. The fidelities of the different operations are checked at various stages during the simulation[1] including multi-level decoherence. Average fidelity drops are 1.3%, 2.56%, and 1.23% during the application of state preparation, off-diagonal part of the Walsh-Hadamard gate, and tomography pulses(points f1, f2, and f3 in Fig. 6.3(a)). The average fidelity drops 0.38% due to the decoherence processes including higher levels and 0.98% due to the detuned drive of 0-1 transition throughout the experiments. We additionally performed numerical simulations of the gate applied on the qutrit thermal state with varying 0-2 drive phases and compare it to the experimentally observed values. Figure 6.4 shows the measured fidelities (black squares) versus the 0-2 two photon drive phase relative to the nominal value. In these experiments, the 0-1 and 1-2 drive frequencies

[1]Some of the simulations are performed in Quantum ToolBox in Pyhton(QuTiP) [108]

are adjusted by the detuning on 0-2 two-photon drive frequency. The simulations with these parameters (Figure 6.4 blue dashed line) agree with the experimentally observed fidelities. We note that if the drive frequencies are adjusted to be on resonance with the ac-Stark shifted transition frequencies for the all qutrit transitions, the simulations result in fidelities reaching above 99% (Figure 6.4 red line).

6.7 Conclusions

In conclusion, we have implemented a Walsh-Hadamard gate in a superconducting qutrit. The implementation of the gate relied on a two-step decomposition, which only required the application of a single microwave pulse with three tones coupling the three pairs of qutrit energy levels. The experimentally characterized gate fidelity is 91%, whereas numerical modelling indicated that with proper compensation of ac-Stark shifts the gate fidelity would exceed 99%. This work demonstrates the potential of multi-tone multi-level control in superconducting devices and opens interesting avenues for exploration of superconducting qudits in quantum computing and other areas of quantum science.

Chapter 7

Conclusion

In this thesis, we have presented the design, modeling and characterization of a three-Josephson junction superconducting loop circuit with three large shunt capacitors. The capacitive shunting of the all three junctions of the flux qubit offers flexibility in device design. The use of shunt capacitors was not only to uniformly redistribute the electric fields and effectively reduce the participation ratio lossy materials in the vicinity of the Josephson junctions and interfaces but also to realize reliable and reproducible device fabrication. We demonstrated full control of the device in qubit and qutrit space and performed device characterization. At the flux-symmetry point, the spectroscopy experiments showed large anharmonicity in energy level structure. The circuit model based on the complete capacitance structure of the device is in perfect agreement with the spectroscopic characterization.

Coherence experiments showed that qubit energy relaxation time is comparable to the best results reported previously on a capacitively shunted flux qubit design with moderate anharmonicity [21] and approaching to high coherence transmons which has poor anharmonicity. Our design of capacitive shunting of flux qubits offers high-relaxation time and large-anharmonicity combined together. We considered several dephasing channels and found that $1/f$ flux noise and the photon number fluctuations in the resonator to be the

possible limiting factors. Coherence experiments in qutrit space show similar results to coherence in qubit space, indicating that the shunted design is applicable to multi-level computational applications.

Anharmonicity affects the speed and performance of single-qubit gates. The large anharmonic structure of the device allows to implement fast and high-fidelity single-qubit gates. We demonstrated high-fidelity gates characterized with randomized benchmarking protocol, exceeding the threshold for the fault tolerant computation. We also performed numerical simulations of the randomized benchmarking protocol and identify the main limiting factors for the average gate fidelity to be the relatively strong drive strength and the long time gap between pulses.

We also demonstrated the implementation of a Walsh-Hadamard gate in qutrit space. The gate is decomposed into diagonal and off-diagonal unitary operations which include simultaneous drive of single and two photon transitions and phase shift of adjacent pulses. This unique decomposition allows for a simple implementation of the gate. The density matrix during the state evolution is reconstructed by utilizing quantum state tomography. The gate is applied on several prepared states and the gate fidelity is measured against expected results. We performed numerical simulations of the gate and found that the gate fidelity can be improved significantly with optimal control parameters and by compensating for the ac-Stark shifts.

In summary, our design of capacitive shunting of the flux qubit yields large-anharmonicity and high-coherence devices with multi-level structure, applicable for gate based quantum computation and has prospects for quantum protocols utilizing multi-level structure.

7.1 Future work

In this work, we demonstrated that capacitively shunted flux qubits offer high coherence with large anharmonicity offering fast implementation of high fidelity quantum gates. The

circuit model predicts the qubit characteristics well and can be further used to explore the full device design space. The study of coherence remains a highly relevant topic. Experimental results suggest that the work on capacitively shunted flux qubit would be expanded on to probe the limitations on the coherence. The qubit dephasing due the flux fluctuations could be further improved by reducing the sensitivity to flux. In addition, any noise contribution from photon fluctuations in the microwave resonator could be mitigated by utilizing better isolation of the device and filtering of the signal lines.

In future, this work would also benefit from the study of the fixed and tunable two-qubit coupling mechanisms. Two-qubit gates are essential for universal computation, therefore, utilizing the large-anharmonic structure of the capacitively shunted flux qubits to investigate high fidelity fast two-qubit gates is a very important direction for future work. The capacitively shunted flux qubit design already offers flexible capacitive and inductive coupling mechanisms

The multi-level structure of the device would promise an essential use in the field of quantum computation, communication, error correction and potentially in reducing the scalability complexity with increased number of computational space. Therefore, investigating the shunted devices in multi-level structure, developing couplers, and studying fast and high fidelity multi-level gates is another interesting research avenue.

References

[1] Michael A. Nielsen and Isaac L. Chuang. *Quantum computation and quantum information*. Cambridge University Press, Cambridge ; New York, 10th anniversary ed edition, 2010.

[2] P.W. Shor. Algorithms for quantum computation: discrete logarithms and factoring. In *Proceedings 35th Annual Symposium on Foundations of Computer Science*, pages 124–134, Santa Fe, NM, USA, 1994. IEEE Comput. Soc. Press.

[3] Daniel Loss and David P. DiVincenzo. Quantum computation with quantum dots. *Physical Review A*, 57(1):120–126, January 1998.

[4] Immanuel Bloch. Quantum coherence and entanglement with ultracold atoms in optical lattices. *Nature*, 453(7198):1016–1022, June 2008.

[5] C. Monroe, D. M. Meekhof, B. E. King, W. M. Itano, and D. J. Wineland. Demonstration of a Fundamental Quantum Logic Gate. *Physical Review Letters*, 75(25):4714–4717, December 1995.

[6] C. Monroe and J. Kim. Scaling the Ion Trap Quantum Processor. *Science*, 339(6124):1164–1169, March 2013.

[7] Rainer Blatt and David Wineland. Entangled states of trapped atomic ions. *Nature*, 453(7198):1008–1015, June 2008.

[8] D. Jaksch, J. I. Cirac, P. Zoller, S. L. Rolston, R. Côté, and M. D. Lukin. Fast Quantum Gates for Neutral Atoms. *Physical Review Letters*, 85(10):2208–2211, September 2000.

[9] John J. L. Morton, Alexei M. Tyryshkin, Richard M. Brown, Shyam Shankar, Brendon W. Lovett, Arzhang Ardavan, Thomas Schenkel, Eugene E. Haller, Joel W. Ager, and S. A. Lyon. Solid-state quantum memory using the 31p nuclear spin. *Nature*, 455(7216):1085–1088, October 2008.

[10] R. Hanson, L. P. Kouwenhoven, J. R. Petta, S. Tarucha, and L. M. K. Vandersypen. Spins in few-electron quantum dots. *Reviews of Modern Physics*, 79(4):1217–1265, October 2007.

[11] Iulia Buluta, Sahel Ashhab, and Franco Nori. Natural and artificial atoms for quantum computation. *Reports on Progress in Physics*, 74(10):104401, October 2011.

[12] John Clarke and Frank K. Wilhelm. Superconducting quantum bits. *Nature*, 453(7198):1031–1042, June 2008.

[13] M. H. Devoret and R. J. Schoelkopf. Superconducting Circuits for Quantum Information: An Outlook. *Science*, 339(6124):1169–1174, March 2013.

[14] V. Bouchiat, D. Vion, P. Joyez, D. Esteve, and M. H. Devoret. Quantum Coherence with a Single Cooper Pair. *Physica Scripta*, T76(1):165, 1998.

[15] John M. Martinis, S. Nam, J. Aumentado, and C. Urbina. Rabi Oscillations in a Large Josephson-Junction Qubit. *Physical Review Letters*, 89(11), August 2002.

[16] I. Chiorescu. Coherent Quantum Dynamics of a Superconducting Flux Qubit. *Science*, 299(5614):1869–1871, March 2003.

[17] Jens Koch, Terri M. Yu, Jay Gambetta, A. A. Houck, D. I. Schuster, J. Majer, Alexandre Blais, M. H. Devoret, S. M. Girvin, and R. J. Schoelkopf. Charge-

insensitive qubit design derived from the Cooper pair box. *Physical Review A*, 76(4), October 2007.

[18] Jonathan R. Friedman, Vijay Patel, W. Chen, S. K. Tolpygo, and J. E. Lukens. Quantum superposition of distinct macroscopic states. *Nature*, 406(6791):43–46, July 2000.

[19] C. H. van der Wal. Quantum Superposition of Macroscopic Persistent-Current States. *Science*, 290(5492):773–777, October 2000.

[20] J. Q. You, Xuedong Hu, S. Ashhab, and Franco Nori. Low-decoherence flux qubit. *Physical Review B*, 75(14):140515, April 2007.

[21] Fei Yan, Simon Gustavsson, Archana Kamal, Jeffrey Birenbaum, Adam P. Sears, David Hover, Ted J. Gudmundsen, Danna Rosenberg, Gabriel Samach, S. Weber, Jonilyn L. Yoder, Terry P. Orlando, John Clarke, Andrew J. Kerman, and William D. Oliver. The flux qubit revisited to enhance coherence and reproducibility. *Nature Communications*, 7:12964, November 2016.

[22] Peter K. Day, Henry G. LeDuc, Benjamin A. Mazin, Anastasios Vayonakis, and Jonas Zmuidzinas. A broadband superconducting detector suitable for use in large arrays. *Nature*, 425(6960):817–821, October 2003.

[23] Benjamin A. Mazin, Peter K. Day, Henry G. LeDuc, Anastasios Vayonakis, and Jonas Zmuidzinas. Superconducting kinetic inductance photon detectors. page 283, Waikoloa, Hawai'i, United States, December 2002.

[24] M. A. Castellanos-Beltran and K. W. Lehnert. Widely tunable parametric amplifier based on a superconducting quantum interference device array resonator. *Applied Physics Letters*, 91(8):083509, August 2007.

[25] A. Wallraff, D. I. Schuster, A. Blais, L. Frunzio, J. Majer, M. H. Devoret, S. M. Girvin, and R. J. Schoelkopf. Approaching Unit Visibility for Control of a Super-

conducting Qubit with Dispersive Readout. *Physical Review Letters*, 95(6):060501, August 2005.

[26] Alexandre Blais, Ren-Shou Huang, Andreas Wallraff, S. M. Girvin, and R. J. Schoelkopf. Cavity quantum electrodynamics for superconducting electrical circuits: An architecture for quantum computation. *Physical Review A*, 69(6), June 2004.

[27] J. Majer, J. M. Chow, J. M. Gambetta, Jens Koch, B. R. Johnson, J. A. Schreier, L. Frunzio, D. I. Schuster, A. A. Houck, A. Wallraff, A. Blais, M. H. Devoret, S. M. Girvin, and R. J. Schoelkopf. Coupling superconducting qubits via a cavity bus. *Nature*, 449(7161):443–447, September 2007.

[28] David M. Pozar. *Microwave engineering*. Wiley, Hoboken, NJ, 4th ed edition, 2012.

[29] Rainee Simons and Institute of Electrical and Electronics Engineers. *Coplanar waveguide circuits, components, and systems*. John Wiley & Sons, Incorporated., Hoboken, 2001.

[30] H. Wang, M. Hofheinz, J. Wenner, M. Ansmann, R. C. Bialczak, M. Lenander, Erik Lucero, M. Neeley, A. D. O'Connell, D. Sank, M. Weides, A. N. Cleland, and John M. Martinis. Improving the coherence time of superconducting coplanar resonators. *Applied Physics Letters*, 95(23):233508, December 2009.

[31] M. R. Vissers, J. Gao, D. S. Wisbey, D. A. Hite, C. C. Tsuei, A. D. Corcoles, M. Steffen, and D. P. Pappas. Low loss superconducting titanium nitride coplanar waveguide resonators. *Applied Physics Letters*, 97(23):232509, December 2010.

[32] Jeremy M. Sage, Vladimir Bolkhovsky, William D. Oliver, Benjamin Turek, and Paul B. Welander. Study of loss in superconducting coplanar waveguide resonators. *Journal of Applied Physics*, 109(6):063915, March 2011.

[33] A. A. Clerk, M. H. Devoret, S. M. Girvin, Florian Marquardt, and R. J. Schoelkopf. Introduction to quantum noise, measurement, and amplification. *Reviews of Modern Physics*, 82(2):1155–1208, April 2010.

[34] M. Göppl, A. Fragner, M. Baur, R. Bianchetti, S. Filipp, J. M. Fink, P. J. Leek, G. Puebla, L. Steffen, and A. Wallraff. Coplanar waveguide resonators for circuit quantum electrodynamics. *Journal of Applied Physics*, 104(11):113904, December 2008.

[35] B. D. Josephson. Possible new effects in superconductive tunnelling. *Physics Letters*, 1(7):251 – 253, 1962.

[36] Michael Tinkham. *Introduction to superconductivity*. Dover Publications, Mineola, N.Y., 2004. OCLC: 853663851.

[37] J. Bardeen, L. N. Cooper, and J. R. Schrieffer. Theory of Superconductivity. *Physical Review*, 108(5):1175–1204, December 1957.

[38] Vinay Ambegaokar and Alexis Baratoff. Tunneling Between Superconductors. *Physical Review Letters*, 10(11):486–489, June 1963.

[39] David P. DiVincenzo. The Physical Implementation of Quantum Computation. *Fortschritte der Physik*, 48(9-11):771–783, September 2000.

[40] T. P. Orlando, J. E. Mooij, Lin Tian, Caspar H. van der Wal, L. S. Levitov, Seth Lloyd, and J. J. Mazo. Superconducting persistent-current qubit. *Physical Review B*, 60(22):15398–15413, December 1999.

[41] E.T. Jaynes and F.W. Cummings. Comparison of quantum and semiclassical radiation theories with application to the beam maser. *Proceedings of the IEEE*, 51(1):89–109, 1963.

[42] Howard Carmichael. *An open systems approach to quantum optics: lectures presented at the Université libre de Bruxelles, October 28 to November 4, 1991*. Number m18 in Lecture notes in physics. Springer-Verlag, Berlin ; New York, 1993.

[43] G. Ithier, E. Collin, P. Joyez, P. J. Meeson, D. Vion, D. Esteve, F. Chiarello, A. Shnirman, Y. Makhlin, J. Schriefl, and G. Schön. Decoherence in a superconducting quantum bit circuit. *Physical Review B*, 72(13), October 2005.

[44] M Kenyon, C J Lobb, and F C Wellstood. Temperature dependence of low-frequency noise in Al–Al2o3–Al single-electron transistors. *J. Appl. Phys.*, 88(11):6, 2000.

[45] R. Barends, N. Vercruyssen, A. Endo, P. J. de Visser, T. Zijlstra, T. M. Klapwijk, P. Diener, S. J. C. Yates, and J. J. A. Baselmans. Minimal resonator loss for circuit quantum electrodynamics. *Applied Physics Letters*, 97(2):023508, July 2010.

[46] Gheorghe Stan, Stuart B. Field, and John M. Martinis. Critical Field for Complete Vortex Expulsion from Narrow Superconducting Strips. *Physical Review Letters*, 92(9), March 2004.

[47] P. Kumar, S. Sendelbach, M. A. Beck, J. W. Freeland, Zhe Wang, Hui Wang, Clare C. Yu, R. Q. Wu, D. P. Pappas, and R. McDermott. Origin and Reduction of 1 / f Magnetic Flux Noise in Superconducting Devices. *Physical Review Applied*, 6(4), October 2016.

[48] J.-L. Orgiazzi, C. Deng, D. Layden, R. Marchildon, F. Kitapli, F. Shen, M. Bal, F. R. Ong, and A. Lupascu. Flux qubits in a planar circuit quantum electrodynamics architecture: Quantum control and decoherence. *Physical Review B*, 93(10), March 2016.

[49] Y. Nakamura, Yu. A. Pashkin, and J. S. Tsai. Coherent control of macroscopic quantum states in a single-Cooper-pair box. *Nature*, 398(6730):786–788, April 1999.

[50] Chad Rigetti, Jay M. Gambetta, Stefano Poletto, B. L. T. Plourde, Jerry M. Chow, A. D. Córcoles, John A. Smolin, Seth T. Merkel, J. R. Rozen, George A. Keefe, Mary B. Rothwell, Mark B. Ketchen, and M. Steffen. Superconducting qubit in a waveguide cavity with a coherence time approaching 0.1 ms. *Physical Review B*, 86(10), September 2012.

[51] R. Harris, T. Lanting, A. J. Berkley, J. Johansson, M. W. Johnson, P. Bunyk, E. Ladizinsky, N. Ladizinsky, T. Oh, and S. Han. Compound Josephson-junction coupler for flux qubits with minimal crosstalk. *Physical Review B*, 80(5), August 2009.

[52] Abdufarrukh A. Abdumalikov, Oleg Astafiev, Yasunobu Nakamura, Yuri A. Pashkin, and JawShen Tsai. Vacuum Rabi splitting due to strong coupling of a flux qubit and a coplanar-waveguide resonator. *Physical Review B*, 78(18), November 2008.

[53] J. B. Majer, F. G. Paauw, A. C. J. ter Haar, C. J. P. M. Harmans, and J. E. Mooij. Spectroscopy on Two Coupled Superconducting Flux Qubits. *Physical Review Letters*, 94(9), March 2005.

[54] Alec Maassen van den Brink, A J Berkley, and M Yalowsky. Mediated tunable coupling of flux qubits. *New Journal of Physics*, 7:230–230, November 2005.

[55] A. O. Niskanen, K. Harrabi, F. Yoshihara, Y. Nakamura, S. Lloyd, and J. S. Tsai. Quantum Coherent Tunable Coupling of Superconducting Qubits. *Science*, 316(5825):723–726, May 2007.

[56] P. Forn-Díaz, J. J. García-Ripoll, B. Peropadre, J.-L. Orgiazzi, M. A. Yurtalan, R. Belyansky, C. M. Wilson, and A. Lupascu. Ultrastrong coupling of a single artificial atom to an electromagnetic continuum in the nonperturbative regime. *Nature Physics*, 13(1):39–43, October 2016.

[57] Fumiki Yoshihara, Tomoko Fuse, Sahel Ashhab, Kosuke Kakuyanagi, Shiro Saito, and Kouichi Semba. Superconducting qubit–oscillator circuit beyond the ultrastrong-coupling regime. *Nature Physics*, 13(1):44–47, October 2016.

[58] Yu-xi Liu, J. Q. You, L. F. Wei, C. P. Sun, and Franco Nori. Optical Selection Rules and Phase-Dependent Adiabatic State Control in a Superconducting Quantum Circuit. *Physical Review Letters*, 95(8), August 2005.

[59] Aaron D. O'Connell, M. Ansmann, R. C. Bialczak, M. Hofheinz, N. Katz, Erik Lucero, C. McKenney, M. Neeley, H. Wang, E. M. Weig, A. N. Cleland, and J. M. Martinis. Microwave dielectric loss at single photon energies and millikelvin temperatures. *Applied Physics Letters*, 92(11):112903, March 2008.

[60] C. M. Quintana, A. Megrant, Z. Chen, A. Dunsworth, B. Chiaro, R. Barends, B. Campbell, Yu Chen, I.-C. Hoi, E. Jeffrey, J. Kelly, J. Y. Mutus, P. J. J. O'Malley, C. Neill, P. Roushan, D. Sank, A. Vainsencher, J. Wenner, T. C. White, A. N. Cleland, and John M. Martinis. Characterization and reduction of microfabrication-induced decoherence in superconducting quantum circuits. *Applied Physics Letters*, 105(6):062601, August 2014.

[61] Matthias Steffen, Shwetank Kumar, David P. DiVincenzo, J. R. Rozen, George A. Keefe, Mary Beth Rothwell, and Mark B. Ketchen. High-Coherence Hybrid Superconducting Qubit. *Physical Review Letters*, 105(10):100502, September 2010.

[62] Jiansong Gao. *The physics of superconducting microwave resonators*. PhD thesis, California Institute of Technology, 2008.

[63] X. Y. Jin, A. Kamal, A. P. Sears, T. Gudmundsen, D. Hover, J. Miloshi, R. Slattery, F. Yan, J. Yoder, T. P. Orlando, S. Gustavsson, and W. D. Oliver. Thermal and Residual Excited-State Population in a 3d Transmon Qubit. *Physical Review Letters*, 114(24):240501, June 2015.

[64] Matthew Reagor, Wolfgang Pfaff, Christopher Axline, Reinier W. Heeres, Nissim Ofek, Katrina Sliwa, Eric Holland, Chen Wang, Jacob Blumoff, Kevin Chou, Michael J. Hatridge, Luigi Frunzio, Michel H. Devoret, Liang Jiang, and Robert J. Schoelkopf. Quantum memory with millisecond coherence in circuit QED. *Physical Review B*, 94(1):014506, July 2016.

[65] Simon Gustavsson, Fei Yan, Gianluigi Catelani, Jonas Bylander, Archana Kamal, Jeffrey Birenbaum, David Hover, Danna Rosenberg, Gabriel Samach, Adam P.

Sears, Steven J. Weber, Jonilyn L. Yoder, John Clarke, Andrew J. Kerman, Fumiki Yoshihara, Yasunobu Nakamura, Terry P. Orlando, and William D. Oliver. Suppressing relaxation in superconducting qubits by quasiparticle pumping. *Science*, 354(6319):1573–1577, December 2016.

[66] J. Kelly. Engineering superconducting qubit arrays for Quantum Supremacy. 2018.

[67] Will Knight. *IBM announces a trailblazing quantum machine*. 2018.

[68] J. S. Otterbach, R. Manenti, N. Alidoust, A. Bestwick, M. Block, B. Bloom, S. Caldwell, N. Didier, E. Schuyler Fried, S. Hong, P. Karalekas, C. B. Osborn, A. Papageorge, E. C. Peterson, G. Prawiroatmodjo, N. Rubin, Colm A. Ryan, D. Scarabelli, M. Scheer, E. A. Sete, P. Sivarajah, Robert S. Smith, A. Staley, N. Tezak, W. J. Zeng, A. Hudson, Blake R. Johnson, M. Reagor, M. P. da Silva, and C. Rigetti. Unsupervised Machine Learning on a Hybrid Quantum Computer. *arXiv:1712.05771 [quant-ph]*, December 2017.

[69] J. Zhang, G. Pagano, P. W. Hess, A. Kyprianidis, P. Becker, H. Kaplan, A. V. Gorshkov, Z.-X. Gong, and C. Monroe. Observation of a many-body dynamical phase transition with a 53-qubit quantum simulator. *Nature*, 551(7682):601–604, November 2017.

[70] Hannes Bernien, Sylvain Schwartz, Alexander Keesling, Harry Levine, Ahmed Omran, Hannes Pichler, Soonwon Choi, Alexander S. Zibrov, Manuel Endres, Markus Greiner, Vladan Vuletić, and Mikhail D. Lukin. Probing many-body dynamics on a 51-atom quantum simulator. *Nature*, 551(7682):579–584, November 2017.

[71] J. Kelly, R. Barends, A. G. Fowler, A. Megrant, E. Jeffrey, T. C. White, D. Sank, J. Y. Mutus, B. Campbell, Yu Chen, Z. Chen, B. Chiaro, A. Dunsworth, I.-C. Hoi, C. Neill, P. J. J. O'Malley, C. Quintana, P. Roushan, A. Vainsencher, J. Wenner, A. N. Cleland, and John M. Martinis. State preservation by repetitive error detection in a superconducting quantum circuit. *Nature*, 519(7541):66–69, March 2015.

[72] Jay M. Gambetta, Jerry M. Chow, and Matthias Steffen. Building logical qubits in a superconducting quantum computing system. *npj Quantum Information*, 3(1), December 2017.

[73] R. Barends, J. Kelly, A. Megrant, A. Veitia, D. Sank, E. Jeffrey, T. C. White, J. Mutus, A. G. Fowler, B. Campbell, Y. Chen, Z. Chen, B. Chiaro, A. Dunsworth, C. Neill, P. O'Malley, P. Roushan, A. Vainsencher, J. Wenner, A. N. Korotkov, A. N. Cleland, and John M. Martinis. Superconducting quantum circuits at the surface code threshold for fault tolerance. *Nature*, 508(7497):500–503, April 2014.

[74] Jerry M. Chow, Jay M. Gambetta, A. D. Córcoles, Seth T. Merkel, John A. Smolin, Chad Rigetti, S. Poletto, George A. Keefe, Mary B. Rothwell, J. R. Rozen, Mark B. Ketchen, and M. Steffen. Universal Quantum Gate Set Approaching Fault-Tolerant Thresholds with Superconducting Qubits. *Physical Review Letters*, 109(6):060501, August 2012.

[75] Austin G. Fowler, Matteo Mariantoni, John M. Martinis, and Andrew N. Cleland. Surface codes: Towards practical large-scale quantum computation. *Physical Review A*, 86(3):032324, September 2012.

[76] Sergio Boixo, Sergei V. Isakov, Vadim N. Smelyanskiy, Ryan Babbush, Nan Ding, Zhang Jiang, Michael J. Bremner, John M. Martinis, and Hartmut Neven. Characterizing quantum supremacy in near-term devices. *Nature Physics*, 14(6):595–600, June 2018.

[77] F. Motzoi, J. M. Gambetta, P. Rebentrost, and F. K. Wilhelm. Simple Pulses for Elimination of Leakage in Weakly Nonlinear Qubits. *Physical Review Letters*, 103(11):110501, September 2009.

[78] J. M. Chow, L. DiCarlo, J. M. Gambetta, F. Motzoi, L. Frunzio, S. M. Girvin, and R. J. Schoelkopf. Optimized driving of superconducting artificial atoms for improved single-qubit gates. *Physical Review A*, 82(4):040305, October 2010.

[79] P. C. de Groot, S. Ashhab, A. Lupaşcu, L. DiCarlo, Franco Nori, C. J. P. M. Harmans, and J. E. Mooij. Selective darkening of degenerate transitions for implementing quantum controlled-NOT gates. *New Journal of Physics*, 14(7):073038, 2012.

[80] Earl T. Campbell. Enhanced Fault-Tolerant Quantum Computing in d-Level Systems. *Physical Review Letters*, 113(23):230501, December 2014.

[81] Daniel Gottesman. Fault-Tolerant Quantum Computation with Higher-Dimensional Systems. In Colin P. Williams, editor, *Quantum Computing and Quantum Communications*, Lecture Notes in Computer Science, pages 302–313. Springer Berlin Heidelberg, 1999.

[82] Ashok Muthukrishnan and C. R. Stroud. Multivalued logic gates for quantum computation. *Physical Review A*, 62(5):052309, October 2000.

[83] M. Stern, G. Catelani, Y. Kubo, C. Grezes, A. Bienfait, D. Vion, D. Esteve, and P. Bertet. Flux Qubits with Long Coherence Times for Hybrid Quantum Circuits. *Physical Review Letters*, 113(12):123601, September 2014.

[84] P. V. Klimov, J. Kelly, Z. Chen, M. Neeley, A. Megrant, B. Burkett, R. Barends, K. Arya, B. Chiaro, Yu Chen, A. Dunsworth, A. Fowler, B. Foxen, C. Gidney, M. Giustina, R. Graff, T. Huang, E. Jeffrey, Erik Lucero, J. Y. Mutus, O. Naaman, C. Neill, C. Quintana, P. Roushan, Daniel Sank, A. Vainsencher, J. Wenner, T. C. White, S. Boixo, R. Babbush, V. N. Smelyanskiy, H. Neven, and John M. Martinis. Fluctuations of energy-relaxation times in superconducting qubits. *Phys. Rev. Lett.*, 121:090502, Aug 2018.

[85] R. Barends, J. Kelly, A. Megrant, D. Sank, E. Jeffrey, Y. Chen, Y. Yin, B. Chiaro, J. Mutus, C. Neill, P. O'Malley, P. Roushan, J. Wenner, T. C. White, A. N. Cleland, and John M. Martinis. Coherent josephson qubit suitable for scalable quantum integrated circuits. *Phys. Rev. Lett.*, 111:080502, Aug 2013.

[86] Clemens Müller, Jürgen Lisenfeld, Alexander Shnirman, and Stefano Poletto. Interacting two-level defects as sources of fluctuating high-frequency noise in superconducting circuits. *Phys. Rev. B*, 92:035442, Jul 2015.

[87] F. Yoshihara, K. Harrabi, A. O. Niskanen, Y. Nakamura, and J. S. Tsai. Decoherence of Flux Qubits due to 1 / f Flux Noise. *Physical Review Letters*, 97(16), October 2006.

[88] Yuriy Makhlin and Alexander Shnirman. Dephasing of Solid-State Qubits at Optimal Points. *Physical Review Letters*, 92(17), April 2004.

[89] E. Knill, D. Leibfried, R. Reichle, J. Britton, R. B. Blakestad, J. D. Jost, C. Langer, R. Ozeri, S. Seidelin, and D. J. Wineland. Randomized benchmarking of quantum gates. *Physical Review A*, 77(1), January 2008.

[90] Easwar Magesan, J. M. Gambetta, and Joseph Emerson. Scalable and Robust Randomized Benchmarking of Quantum Processes. *Physical Review Letters*, 106(18), May 2011.

[91] Markus Grassl, Martin Rötteler, and Thomas Beth. Efficient quantum circuits for non-qubit quantum error-correcting codes. *International Journal of Foundations of Computer Science*, 14(05):757–775, October 2003.

[92] Stephen S. Bullock, Dianne P. O'Leary, and Gavin K. Brennen. Asymptotically Optimal Quantum Circuits for d-Level Systems. *Physical Review Letters*, 94(23):230502, June 2005.

[93] Earl T. Campbell, Hussain Anwar, and Dan E. Browne. Magic-State Distillation in All Prime Dimensions Using Quantum Reed-Muller Codes. *Physical Review X*, 2(4):041021, December 2012.

[94] Hussain Anwar, Benjamin J. Brown, Earl T. Campbell, and Dan E. Browne. Fast decoders for qudit topological codes. *New Journal of Physics*, 16(6):063038, 2014.

[95] Anirudh Krishna and Jean-Pierre Tillich. Towards low overhead magic state distillation. *arXiv:1811.08461 [quant-ph]*, November 2018.

[96] M. V. Suslov, G. B. Lesovik, and G. Blatter. Quantum abacus for counting and factorizing numbers. *Physical Review A*, 83(5):052317, May 2011.

[97] Frédéric Bouchard, Robert Fickler, Robert W. Boyd, and Ebrahim Karimi. High-dimensional quantum cloning and applications to quantum hacking. *Science Advances*, 3(2):e1601915, February 2017.

[98] Ashok Muthukrishnan and C.R. Stroud. Quantum fast Fourier transform using multilevel atoms. *Journal of Modern Optics*, 49(13):2115–2127, November 2002.

[99] R. Bianchetti, S. Filipp, M. Baur, J. M. Fink, C. Lang, L. Steffen, M. Boissonneault, A. Blais, and A. Wallraff. Control and Tomography of a Three Level Superconducting Artificial Atom. *Physical Review Letters*, 105(22), November 2010.

[100] Frederick W. Strauch, Philip R. Johnson, Alex J. Dragt, C. J. Lobb, J. R. Anderson, and F. C. Wellstood. Quantum Logic Gates for Coupled Superconducting Phase Qubits. *Physical Review Letters*, 91(16):167005, October 2003.

[101] T. Hönigl-Decrinis, I. V. Antonov, R. Shaikhaidarov, V. N. Antonov, A. Yu. Dmitriev, and O. V. Astafiev. Mixing of coherent waves in a single three-level artificial atom. *Physical Review A*, 98(4):041801, October 2018.

[102] A. A. Abdumalikov Jr, J. M. Fink, K. Juliusson, M. Pechal, S. Berger, A. Wallraff, and S. Filipp. Experimental realization of non-Abelian non-adiabatic geometric gates. *Nature*, 496(7446):482–485, April 2013.

[103] A. A. Abdumalikov, O. Astafiev, A. M. Zagoskin, Yu. A. Pashkin, Y. Nakamura, and J. S. Tsai. Electromagnetically Induced Transparency on a Single Artificial Atom. *Physical Review Letters*, 104(19):193601, May 2010.

[104] Markus Jerger, Yarema Reshitnyk, Markus Oppliger, Anton Potočnik, Mintu Mondal, Andreas Wallraff, Kenneth Goodenough, Stephanie Wehner, Kristinn Juliusson, Nathan K. Langford, and Arkady Fedorov. Contextuality without nonlocality in a superconducting quantum system. *Nature Communications*, 7:12930, October 2016.

[105] Antti Vepsäläinen, Sergey Danilin, and Sorin Paraoanu. Superadiabatic population transfer by loop driving and synthetic gauges in a superconducting circuit. *arXiv:1709.03731 [quant-ph]*, September 2017.

[106] Nikolay V. Vitanov. Synthesis of arbitrary SU(3) transformations of atomic qutrits. *Physical Review A*, 85(3):032331, March 2012.

[107] A. B. Klimov, R. Guzmán, J. C. Retamal, and C. Saavedra. Qutrit quantum computer with trapped ions. *Physical Review A*, 67(6):062313, June 2003.

[108] J. R. Johansson, P. D. Nation, and Franco Nori. QuTiP 2: A Python framework for the dynamics of open quantum systems. *Computer Physics Communications*, 184(4):1234 – 1240, 2013.

[109] G. Zizak, J. D. Bradshaw, and J. D. Winefordner. Rate equation solution for the temporal behavior of a three-level system. *Applied Optics*, 19(21):3631, November 1980.

[110] Timothy F. Havel. Robust procedures for converting among Lindblad, Kraus and matrix representations of quantum dynamical semigroups. *Journal of Mathematical Physics*, 44(2):534–557, January 2003.

[111] Jonas Bylander, Simon Gustavsson, Fei Yan, Fumiki Yoshihara, Khalil Harrabi, George Fitch, David G. Cory, Yasunobu Nakamura, Jaw-Shen Tsai, and William D. Oliver. Noise spectroscopy through dynamical decoupling with a superconducting flux qubit. *Nature Physics*, 7(7):565–570, July 2011.

[112] Serge Haroche and J.-M. Raimond. *Exploring the Quantum: Atoms, Cavities, and Photons*. OUP Oxford, August 2006. Google-Books-ID: ynwSDAAAQBAJ.

[113] R. T. Thew, K. Nemoto, A. G. White, and W. J. Munro. Qudit quantum-state tomography. *Physical Review A*, 66(1), July 2002.

[114] Daniel F. V. James, Paul G. Kwiat, William J. Munro, and Andrew G. White. Measurement of qubits. *Physical Review A*, 64(5), October 2001.

APPENDICES

Appendix A

Multi-level decoherence models

A.1 Multi-level relaxation

In multi-level relaxation experiments, the qutrit is prepared into state 2 by applying a π_x^{01} and a π_x^{12} pulse sequentially to the qutrit thermal equilibrium state of known steady state populations. The total relaxation from state 2 depends on the relaxation and excitation rates from states 0, 1, and 2. For population analysis at a given time during relaxation, we follow Zizak *et al.* [109]. The time-dependent populations for states 1 and 2 are given by

$$P_1(t) = c_0 e^{(-\xi_0 t)} + c_1 e^{(-\xi_1 t)} + \frac{Q_1}{B} \tag{A.1}$$

$$P_2(t) = c_0 \frac{(R_1 - \xi_0)}{R_{21}^*} e^{(-\xi_0 t)} + c_1 \frac{(R_1 - \xi_1)}{R_{21}^*} e^{(-\xi_1 t)} + \frac{Q_2}{B}, \tag{A.2}$$

with $P_0(t) + P_1(t) + P_2(t) = 1$. The measured state populations are fitted with the model with Γ_{21} and Γ_{20} as free fit parameters and the ratios Γ_{12}/Γ_{21} and Γ_{02}/Γ_{20} are constricted to corresponding Boltzmann factors. The rates Γ_{10} and Γ_{01} are determined with qubit

relaxation experiment prior to the multi-level relaxation experiments. Table A.1 shows the extracted relaxation and excitation rates at $0.5\,\Phi_0$ and $0.501\,\Phi_0$.

Table A.1: Multi-level relaxation and excitation rates

Rate	Value at 0.5 Φ_0	Value at 0.501 Φ_0
Γ_{01}	1.4 kHz	1.2 kHz
Γ_{10}	29.5 kHz	63.4 kHz
Γ_{12}	8.8 Hz	0.4 Hz
Γ_{21}	124.3 kHz	78.1 Hz
Γ_{02}	0.1 Hz	0.01 Hz
Γ_{20}	27.8 kHz	61.1 kHz

A.2 Multilevel dephasing

In this section, we discuss the interplay of energy relaxation and pure dephasing in multi-level decoherence. For a two-level system, a Ramsey experiment is used to characterize the decay of the off-diagonal matrix element ρ_{01} of the density matrix. In a frame resonant with the transition frequency, this decay is given by $\rho_{01}(t) = \mathcal{C}(t)e^{-t/2T_1}$, where T_1 is the energy relaxation time and $\mathcal{C}(t)$ is the coherence function. If noise is modelled as a classical stochastic process $\xi(t)$ contributing a term to the Hamiltonian $H_{\mathrm{qb,r}} = -\hbar\xi(t)\sigma_z/2$, which is diagonal in the energy eigenbasis, the coherence function is given by

$$\mathcal{C}(t) = \langle \exp(-i\int_0^t \xi(t')dt') \rangle, \tag{A.3}$$

where $\langle .. \rangle$ is an average over noise realizations.

In this section we discuss the generalization of this situation to a n-level system. We assume the noise couples diagonally, as a term to the system Hamiltonian

$$H_{\mathrm{r}}(t) = -\hbar \sum_{j=0}^{n-1} \xi_j(t)|j\rangle\langle j|, \tag{A.4}$$

where $|j\rangle$, $j = \overline{0, n-1}$, are the energy eigenstates and $\xi_j(t)$ are random noise processes. We analyze the dynamics of the multi-level system under simulatanous coupling to a Markovian bath and coupling to a noise source described by Eq. A.4. In a rotating frame given by the qubit nominal Hamiltonian, the evolution of the off-diagonal terms of the density matrix $\rho_{jk}(t)$ is given by

$$\rho_{jk}(t) = \exp(i \int_0^t [\xi_j(t') - \xi_k(t')]dt')\tilde{\rho}_{jk}(t), \tag{A.5}$$

where $\tilde{\rho}(t)$ is the density matrix in the rotating frame in the absence of noise terms ($H_{\mathrm{r}}(t) = 0$). When averaging is done over different realizations of the noise, we obtain

$$\rho_{jk}(t) = \mathcal{C}_{jk}(t)\tilde{\rho}_{jk}(t), \tag{A.6}$$

where the generalized coherence function is

$$\mathcal{C}_{jk}(t) = \langle \exp(i \int_0^t [\xi_j(t') - \xi_k(t')]dt') \rangle. \tag{A.7}$$

Formally we can write the transformation of the density matrix in the rotating frame from initial time t_i to final time t_f as

$$\rho(t_f) = D[R[\rho(t_i)]], \tag{A.8}$$

where R is an operator that describes Markovian relaxation and D is an operator that acts on the off-diagonal elements of the density matrix elements according to Eq. A.6. This equation is most conveniently expressed by using the density matrix in column form (see e.g. Ref [110]). To characterize multi-level dephasing in experiments, we proceed as follows. First, multi-level relaxation is characterized in an experiment where we prepare an excited state and we measure the decay of populations versus time. Next, we prepare a superposition of states $|j\rangle$ and $|k\rangle$, and monitor the decay of ρ_{jk} in a Ramsey type experiment. After factoring out energy relaxation terms based on Eq. A.8, the coherence function $\mathcal{C}_{ij}(t)$ is obtained.

A.3 Decoherence with $A/|\omega|^{\alpha}$ noise

In this section, we discuss qubit coherence measurements using CPMG sequences [111, 48]. With Gaussian noise, the coherence function for a CPMG sequence with N pulses is given by

$$C_N(\tau) = \exp\left[\int_{-\infty}^{\infty} d\omega S(\omega) F(\omega, N, \tau)\right], \tag{A.9}$$

where $S(\omega)$ is the double sided noise PSD of fluctuations in qubit angular transition frequency. The filter function $F(\omega, N, \tau)$ is given by

$$F(\omega, N, \tau) = \frac{1}{2}\left|\int_0^{\tau} dt \zeta(N,t) e^{i\omega t}\right|^2, \tag{A.10}$$

where $\zeta(N,t) \in \{-1, 1\}$ is the CPMG sign multiplier for the noise after each refocusing π rotation. Using dimensionless parameter $X = \omega\tau$, Eq. A.10 is expressed as

$$F(X, N, \tau) = \begin{cases} \tau^2 \frac{8}{X^2} \sin^4(\frac{X}{4N}) \frac{\cos^2(X/2)}{\cos^2(X/2N)}, & \text{if } N \text{ is odd,} \\ \tau^2 \frac{8}{X^2} \sin^4(\frac{X}{4N}) \frac{\cos^2(X/2)}{\sin^2(X/2N)}, & \text{if } N \text{ is even.} \end{cases} \tag{A.11}$$

We note that the filter function is peaked at $X \approx N\pi$ with a peak width of the order 1. In the integral in Eq. A.9, we assume we can neglect the variations of the noise PSD $S(\omega)$ over the peak of the filter function. Defining the integrals $I = \int dX F(X, N, \tau)$ and $X^* = (1/I) \int dX F(X, N, \tau) X$, the coherence function can be approximated as

$$C_N(\tau) \approx \exp\left[-2\tau I S\left(\frac{X^*}{\tau}\right)\right]. \tag{A.12}$$

We note that $I \approx 1.24$ and $X^* \approx \pi \times N$ are good approximations for $1 < N < 200$. Eq. A.12 allows for finding the noise PSD directly from the measurement of the coherence function. We next discuss the case when $S(\omega) = A/\omega^{\alpha}$. In this case Eq. A.12 becomes

$$C_N(\tau) = \exp\left[-(\Gamma_N \tau)^{(\alpha+1)}\right], \tag{A.13}$$

with

$$\Gamma_N = (2.48A)^{1/(\alpha+1)}(\pi N)^{(-\alpha/\alpha+1)}. \tag{A.14}$$

At $0.501\,\Phi_0$, we performed CPMG experiments with $N = 1, 5, 10, 20, 40$, and 100 and determined Γ_N for each N using the coherence function in Eq. A.13. The Γ_N dependency on N is fitted with Eq. A.14 and the noise PSD parameters are determined as $A = 1.8 \times 10^{-14}/|\omega|^{\alpha}(\mathrm{rad/s})^{\alpha-1}\Phi_0^2$ with $\alpha = 0.68$.

A.4 Decoherence due to photon noise

We consider dephasing of the qubit at the symmetry point due to fluctuations of the photon number in the cavity. We use numerical simulations to predict dephasing due to this source. Specifically, the photon population of the cavity is modeled using a random telegraph noise with states $n = 0$ (empty cavity) and $n = 1$ (cavity occupied by one photon). The transition rates between two states are $\gamma_{0\to1} = \omega_r/Q \times n_{\mathrm{th}}$ and $\gamma_{1\to0} = \omega_r/Q \times (1 + n_{\mathrm{th}})$, with ω_r the cavity resonance frequency, Q the cavity quality factor, and n_{th} the thermal photon number [112]. The effect of photon number fluctuations on the qubit is determined by the dispersive shift. Based on numerical simulations of the spectrum of the coupled qubit/cavity system, we find that the dispersive shift for the $0-1$ transition is 0.55 MHz. To obtain this number we use the first several levels of the qubit and one level of the cavity. We note that in experiments we observed in certain cases, when the repetition time of experiments was too short, beating patterns in Ramsey oscillations with a beating frequency of 0.5 MHz, which we attribute to photon number fluctuations. This value of the beating frequency is in reasonable agreement with the numerically determined dispersive shift.

Appendix B

Pulses in randomized benchmarking sequence

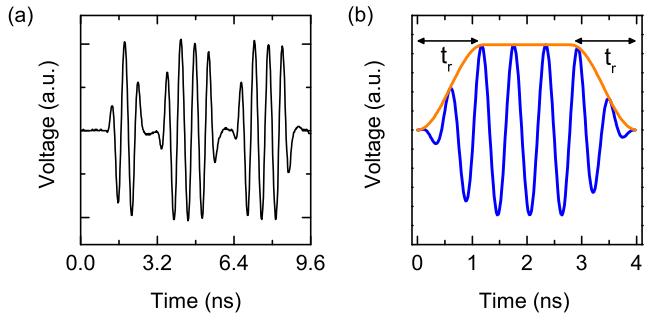

Figure B.1: a) A section of the randomized benchmarking pulse sequence measured with an oscilloscope. b) An example single shaped pulse showing the rise time t_r and the fall time t_f.

The pulses in randomized benchmarking experiments, corresponding to the unitary operators from the Clifford group and the Pauli group, are $\pi/2$ and π rotations around the x(y) axis and denoted by $R_{x(y)}(\theta)$ where θ is the rotation angle. A section of the waveform of the sequence pulse used in the experiments is measured with an oscilloscope and shown in Fig. B.1. The pulses have a driving strength of $2\pi \times 260$ MHz and rise and fall times of

0.6 ns. The duration of the $\pi/2$ and π pulses are 1.62 and 2.64 ns respectively. The time gap between each pulse in the sequence is 0.5 ns. Oscilloscope measurements indicate a good control of pulse shaping with the Tektronix AWG70001A.

Appendix C

Tomography and density matrix reconstruction

C.1 Qutrit tomography

To perform a tomography process on any prepared qutrit state, a set of tomography analyzer pulses are applied just prior to the qubit state readout. In dispersive regime, the homodyne voltage detection method is used for the qutrit state readout and the measured voltage is expressed as

$$V_h = V_{h0}P_0 + V_{h1}P_1 + V_{h2}P_2, \tag{C.1}$$

The tomography sequence first starts with state preparation. Next, the analyzer tomography pulses are applied and the qutrit state read out is performed. The average measured voltage is expressed as $V_k = \text{Tr}\ [\rho.u_k V_h u_k^\dagger]$ [99], where ρ is the density matrix of the state and $u_k V_h u_k^\dagger$ corresponds to voltage measurement after the tomography pulse u_k. Any qutrit density matrix or hermitian operator can be constructed by traceless SU(3)

generators and a (3×3) identity operator [113] as,

$$\rho = \frac{1}{3}\sum_{m=0}^{8} r_m \lambda_m. \tag{C.2}$$

The average homodyne voltage in this case can be written as

$$V_k = \sum_{m=0}^{8} \frac{1}{3}\mathrm{Tr}[\lambda_m u_k V_h u_k^{\dagger}] r_m \tag{C.3}$$

$$= \sum_{m=0}^{8} A_k^m r_m \tag{C.4}$$

The coefficients A_k^m can be calculated and the qutrit density matrix can be reconstructed by

$$\rho = \sum_{k,m=0}^{8} (A_k^m)^{-1} V_k \lambda_m. \tag{C.5}$$

The A matrix depends on the tomography pulses and the pulses are selected to form a complete set while maintaining A to be invertible.

C.2 SU(3) generators and rotation operators

The SU(3) group is given as

$$\lambda_1 = \begin{pmatrix} 0 & 1 & 0 \\ 1 & 0 & 0 \\ 0 & 0 & 0 \end{pmatrix}, \quad \lambda_2 = \begin{pmatrix} 0 & -i & 0 \\ i & 0 & 0 \\ 0 & 0 & 0 \end{pmatrix}, \quad \lambda_3 = \begin{pmatrix} 1 & 0 & 0 \\ 0 & -1 & 0 \\ 0 & 0 & 0 \end{pmatrix},$$

$$\lambda_4 = \begin{pmatrix} 0 & 0 & 1 \\ 0 & 0 & 0 \\ 1 & 0 & 0 \end{pmatrix}, \quad \lambda_5 = \begin{pmatrix} 0 & 0 & -i \\ 0 & 0 & 0 \\ i & 0 & 0 \end{pmatrix}, \quad \lambda_6 = \begin{pmatrix} 0 & 0 & 0 \\ 0 & 0 & 1 \\ 0 & 1 & 0 \end{pmatrix}, \tag{C.6}$$

$$\lambda_7 = \begin{pmatrix} 0 & 0 & 0 \\ 0 & 0 & -i \\ 0 & i & 0 \end{pmatrix}, \quad \lambda_8 = \tfrac{1}{\sqrt{3}} \begin{pmatrix} 1 & 0 & 0 \\ 0 & 1 & 0 \\ 0 & 0 & -2 \end{pmatrix}.$$

The ideal unitary rotation operators in qutrit subspace are given by

$$R_x^{01}(\pi) = \begin{pmatrix} 0 & -i & 0 \\ i & 0 & 0 \\ 0 & 0 & 1 \end{pmatrix}, \quad R_x^{01}(\pi/2) = \tfrac{1}{\sqrt{2}} \begin{pmatrix} 1 & -i & 0 \\ -i & 1 & 0 \\ 0 & 0 & \sqrt{2} \end{pmatrix}, \quad R_y^{01}(\pi/2) = \tfrac{1}{\sqrt{2}} \begin{pmatrix} 1 & -1 & 0 \\ 1 & 1 & 0 \\ 0 & 0 & \sqrt{2} \end{pmatrix},$$

$$R_x^{12}(\pi) = \begin{pmatrix} 1 & 0 & 0 \\ 0 & 0 & -i \\ 0 & -i & 0 \end{pmatrix}, \quad R_x^{12}(\pi/2) = \tfrac{1}{\sqrt{2}} \begin{pmatrix} \sqrt{2} & 0 & 0 \\ 0 & 1 & -i \\ 0 & -i & 1 \end{pmatrix}, \quad R_y^{12}(\pi/2) = \tfrac{1}{\sqrt{2}} \begin{pmatrix} \sqrt{2} & 0 & 0 \\ 0 & 1 & -1 \\ 0 & 1 & 1 \end{pmatrix}. \tag{C.7}$$

C.3 Maximum likelihood estimation

We employ the maximum likelihood estimation (MLE) method for reconstructing the density matrix following James *et al.* [114]. The approach is to generate an expression for a physical density matrix satisfying the normalization, Hermiticity and the positivity properties. A likelihood function is introduced that measures the closeness of the generated density matrix to the experimentally measured one and perform optimization around this closeness. For a qutrit, we adopt similar approach.

$$T(t) = \begin{pmatrix} t1 & 0 & 0 \\ t4 + it5 & t2 & 0 \\ t8 + it9 & t6 + it7 & t3 \end{pmatrix} \tag{C.8}$$

The expression for the density matrix satisfying the aforementioned properties is given as

$$\rho_p(t) = \frac{T^\dagger(t)T(t)}{\mathrm{Tr}[T^\dagger(t)T(t)]}. \tag{C.9}$$

Next we define a function L as

$$L = \sum_k |V_k - \mathrm{Tr}[\rho_p u_k V_h u_k^\dagger]|^2, \tag{C.10}$$

and find the minimum of this function to determine $t1 \ldots t9$. The density matrix is recovered by Eq. C.9

Appendix D

Decomposition of Walsh-Hadamard gate

We seek a decomposition of the Walsh-Hadamard gate of the form

$$U_{\mathrm{WH}} = U_{\mathrm{d}} U_{\mathrm{o}}, \tag{D.1}$$

where $U_{\mathrm{d}} = \exp(-iG_{\mathrm{d}})$ and $U_{\mathrm{o}} = \exp(-iG_{\mathrm{o}})$. The generators G_d and G_o are given by

$$\begin{aligned} G_{\mathrm{d}} &= \begin{pmatrix} \phi_0 & 0 & 0 \\ 0 & \phi_1 & 0 \\ 0 & 0 & \phi_2 \end{pmatrix}, \\ G_{\mathrm{o}} &= \begin{pmatrix} 0 & m_{01} & m_{02} \\ m_{01}^* & 0 & m_{12} \\ m_{02}^* & m_{12}^* & 0 \end{pmatrix}. \end{aligned} \tag{D.2}$$

We perform a numerical search where we sweep the phases ϕ_0, ϕ_1, ϕ_2 between 0 and 2π and look for values that result in a valid decomposition as described in Eqs. (D.1,D.2). We find five decompositions listed in Table D.1. Any of these five decompositions can

Table D.1: Numerically determined matrix elements of Walsh-Hadamard gate generators when the gate is decomposed into two unitary operators as explained in the text.

Decomp.	m_{01}	m_{12}	m_{02}	ϕ_0	ϕ_1	ϕ_2
1	$-0.9672 - 0.2365i$	1.9345	$-0.9672 - 0.2365i$	0.8434	0.3637	0.3637
2	$-0.6982 - 1.2092i$	1.3962	$-0.6981 - 1.2092i$	1.9199	6.1087	6.1086
3	$-0.9672 - 1.6753i$	$0.6885 + 0.7194i$	$0.2788 - 0.9559i$	2.4581	0.3637	5.0322
4	$0.2788 - 0.9559i$	$0.6885 - 0.7194i$	$-0.9672 - 1.6753i$	2.4581	5.0322	0.3637
5	$0.3491 + 0.6046i$	-0.6981	$0.3491 + 0.6046i$	6.1086	4.0143	4.0143

be used to construct the WH gate in the experiment. We note, however, that the Rabi frequencies of the driven gate dynamics will be proportional to $|m_{ij}|$. In other words, if we fix the WH gate pulse duration, the Rabi frequencies will be proportional to $|m_{ij}|$. The driving field amplitude will in turn depend on $|m_{ij}|$, linearly for the 0-1 and 1-2 transitions and quadratically for the 0-2 transition, because we drive the 0-2 transition using a two-photon process. Because the two-photon transition requires stronger driving fields than those required for the other two transitions, and we would like to obtain the fastest gate for a given drive power, we choose the decomposition that has the smallest value of $|m_{02}|$, which is fifth decomposition in Table D.1.

D.1 Tomography pulses with shifted phases

The diagonal part of the gate U_{WH} can be embedded in to the tomography pulses and it can be treated as new set of tomography analyzer pulses $\bar{u}_i$ as

$$\bar{u}_i = U_{\mathrm{d}}^{\dagger} u_i U_{\mathrm{d}}, \tag{D.3}$$

with U_d

$$\begin{pmatrix} e^{-i\varphi_0} & 0 & 0 \\ 0 & e^{-i\varphi_1} & 0 \\ 0 & 0 & e^{-i\varphi_2} \end{pmatrix}. \tag{D.4}$$

The tomography pulses are based on the rotation on the Bloch sphere and a generic rotation is defined as $R_{\vec{n}}^{01(12)}(\theta)$, where $\vec{n}$ is the rotation axis and 01(12) correspond to the transitions between levels 0-1(1-2), the tomography pulses with $U_{\rm d}$ embedded are found as

$$\bar{R}_{\vec{n}}^{01(12)}(\theta) = U_{\rm d}^{\dagger} R_{\vec{n}}^{01(12)}(\theta) U_{\rm d}. \tag{D.5}$$

Considering only 0-1 rotations, Eq. D.5 becomes

$$\begin{aligned} \bar{R}_{\vec{n}}^{01}(\theta) &= \begin{pmatrix} e^{i\varphi_0} & 0 \\ 0 & e^{i\varphi_1} \end{pmatrix} R_{\vec{n}}^{01}(\theta) \begin{pmatrix} e^{-i\varphi_0} & 0 \\ 0 & e^{-i\varphi_1} \end{pmatrix} \\ &= e^{i\frac{\varphi_0-\varphi_1}{2}\sigma_z} \; R(\theta)_{01}^{\vec{n}} \; e^{-i\frac{\varphi_0-\varphi_1}{2}\sigma_z} \end{aligned} \tag{D.6}$$

The general expression for the rotation operator is $R_{\vec{n}}^{01}(\theta) = \cos(\frac{\theta}{2})\mathrm{I} - i\sin(\frac{\theta}{2})(\vec{n}\vec{\sigma})$. If Eq. D.6 is investigated for the σ_x and σ_y parts of the rotation operator, it is found that

$$e^{i\frac{\varphi_0-\varphi_1}{2}\sigma_z} \; \sigma_x \; e^{-i\frac{\varphi_0-\varphi_1}{2}\sigma_z} = \cos(\varphi_0-\varphi_1)\sigma_x - \sin(\varphi_0-\varphi_1)\sigma_y \tag{D.7}$$

$$e^{i\frac{\varphi_0-\varphi_1}{2}\sigma_z} \; \sigma_y \; e^{-i\frac{\varphi_0-\varphi_1}{2}\sigma_z} = \cos(\varphi_0-\varphi_1)\sigma_y + \sin(\varphi_0-\varphi_1)\sigma_x. \tag{D.8}$$

With the above equations, the effect of the diagonal part of the Walsh-Hadamard gate on the pulses u_i can be interpreted as adjustments on the rotation axis as $\bar{R}_{\vec{n}}^{01}(\theta) = R_{\vec{n}'}^{01}(\theta)$. The relation between the rotation axes n and n' is given as

$$\vec{n}' = \vec{n} \begin{pmatrix} \cos(\varphi_0-\varphi_1) & -\sin(\varphi_0-\varphi_1) \\ \sin(\varphi_0-\varphi_1) & \cos(\varphi_0-\varphi_1) \end{pmatrix} \tag{D.9}$$

A resonant drive on 0-1 transition in the general form of $A\cos(\omega_{01}t+\varphi)\sigma_x$ is expressed in the rotating frame as

$$H_{rf} = \frac{A\cos(\varphi)}{2}\sigma_x - \frac{A\sin(\varphi)}{2}\sigma_y, \tag{D.10}$$

where A is the amplitude and φ is the phase of the drive. For this drive in rotating frame, the rotation axis is $\vec{n} = (\cos(\varphi), \sin(\varphi))$ and the rotation angle is proportional to the drive

amplitude and the pulse duration as $\theta = A\Delta t$. Assuming the phase of the tomography pulses to be φ and the rotation axis to be $\vec{n}$, the addition of the diagonal component U_d to the tomography pulses results in new rotation axis $\vec{n}' = (\cos(\varphi+\varphi_0-\varphi_1), \sin(\varphi+\varphi_0-\varphi_1))$. This can also be interpreted as a phase shift in the tomography pulses by $\varphi_0 - \varphi_1$. Similar approach holds for 0-2 transitions.

Appendix E

AC-Stark shift modeling

We use a two-photon process to drive the 0-2 transition, the ac-Stark shift must be taken into account in our implementation of the gate. If 0-2 transition is driven resonantly using a two-photon process with a given drive power and driving field frequency ω_d the resulting Rabi oscillation frequency is given by

$$\Omega_{Rabi,tp} = \frac{|\Omega_{01}\Omega_{12}|}{2(\omega_d - \omega_{01})}, \tag{E.1}$$

where $|\Omega_{01}|$ is the Rabi frequency of 0-1 oscillations if the same drive power is applied resonantly with the 0-1 transition, $|\Omega_{12}|$ is the Rabi frequency of 1-2 oscillations if the same drive power is applied resonantly with the 0-1 transition, and ω_{01} is the resonance frequency of the 0-1 transition.

The drive of the 0-2 two-photon transition can be seen as an off-resonant drive field for the 0-1 and 1-2 transitions. As a result, all of these energy levels will experience ac-Stark shifts. For 0-1 transition, and considering that $\omega_d > \omega_{01}$, the ac-Stark shift will bring levels 0 and 1 closer to each other by

$$\delta\omega_{01} = -\frac{|\Omega_{01}|^2}{2(\omega_d - \omega_{01})}. \tag{E.2}$$

A similar expression can be obtained for the ac-Stark shift of the 1-2 transition:

$$\delta\omega_{12} = \frac{|\Omega_{12}|^2}{2(\omega_d - \omega_{01})}. \tag{E.3}$$

Since Ω_{01} and Ω_{12} are comparable to each other, both ac-Stark shifts are comparable to the two-photon Rabi frequency. And since in our implementation of the gate all transitions are driven simultaneously with comparable Rabi frequencies for all pairs of transitions (as will be discussed in more detail below), the fields used to resonantly drive the 0-1 and 1-2 transitions will have Rabi frequencies that are comparable to the Rabi frequency of the two-photon transition and hence comparable to the 0-1 and 1-2 ac-Stark shifts. If the detuning from exact resonance is comparable to the resonant Rabi frequency, the Rabi oscillation amplitude will be reduced significantly from its resonant value, which is one (i.e. full population transfer between the energy level pair that is being driven). For this reason, the ac-Stark shifts must be taken into account and the drive field frequencies must all be shifted to correct for the ac-Stark shifts.

The device contains higher energy levels that contribute additional ac-Stark shifts comparable to those given above and can therefore lead to significant changes from the situation described above. For example, because $|\Omega_{12}| > |\Omega_{01}|$, the three-level approximation would suggest that the 0-2 transition frequency should be ac-Stark shifted to a larger value, but in the experiment we find that it is shifted in the opposite direction. By gradually increasing the number of energy levels in the theoretical model, we find that we must keep at least five energy levels to obtain good agreement between the theoretical model and experimental data.

Appendix F

Experimental setup

The experiments are performed in a dilution refrigerator at 27 mK. The sample is enclosed in a copper package hosting superconducting coils for local magnetic flux bias. For shielding, the package is placed inside high magnetic permeability metal shields. The sample is connected to readout and control equipment in room temperature with coaxial cables and the pulses are attenuated and filtered at different temperature stages of the fridge.

The qubit control pulses are generated in two ways. First, they are directly generated by Tektronix AWG70001A arbitrary waveform generator. The AWG has a sampling rate of 50 GS/s and a bandwidth of 15 GHZ with 10 bit amplitude resolution. Majority of the experiments are performed with this setup. Second, the pulses are generated by standard microwave synthesizers and shaped with IQ mixers. Similarly, the readout pulses are generated by synthesizers and mixers. The resonator output signal is amplified by HEMT low temperature amplifier and demodulated quadratures are sampled with a digitizer [48].

Appendix G

Pulse calibrations

The calibration procedure for the $R^{01}_{x(y)}(\pi/2)$ pulses is done by applying $[R^{01}_{x(y)}(\theta)]^{2N+1}$ pulses. For large number of repetitions the accumulated error is projected on the measurement basis and the error is minimized by adjustments on θ. Similarly, $R^{01}_{x}(\pi)$ rotations are calibrated by applying $R^{01}_{x}(\pi/2)[R^{01}_{x}(\theta)]^{(2N+1)}$. The pulses on the subspace formed by state 1 and 2 are calibrated similarly. $R^{12}_{x(y)}(\pi/2)$ pulses are calibrated by the pulse sequence $R^{01}_{x}(\pi)[R^{12}_{x(y)}(\theta)]^{(2N+1)}$ and $R^{12}_{x}(\pi)$ pulse is calibrated by $R^{01}_{x}(\pi/2)[R^{12}_{x}(\theta)]^{(2N+1)}$. Pulses are calibrated up to N=300.

The error on the orthogonality of the rotation axes x and y is determined by the sequence $R^{01}_{y'}(\pi/2)\left\{[R^{01}_{x}(\pi/2)]^2[R^{01}_{y'}(\pi/2)]^2\right\}^N R^{01}_{x}(\pi/2)$ where the rotation axis y' is calibrated against x axis. The error on the angle is find to be 0.002 rad with N=10.